Structured Laser Illumination Planar Imaging SLIPI Applications for Spray Diagnostics

Kristensson, Elias

2012

STRUCTURED LASER ILLUMINATION
PLANAR IMAGING

SLIPI

APPLICATIONS FOR SPRAY DIAGNOSTICS

DOCTORAL THESIS

Elias Kristensson

Division of Combustion Physics
Department of Physics

LUND 2012

LUND UNIVERSITY

Elias Kristensson
Division of Combustion Physics
Department of Physics
Lund University
P.O. Box 118
SE-221 00, Lund, Sweden

And now for something completely different...

Abstract

Laser sheet imaging, also known as planar laser imaging, is one of the most versatile optical imaging techniques known and is frequently applied in several different domains. It furthermore constitutes the basis for a variety of other 2D methods, in turn allowing visualization of e.g. velocity, particle size, species concentration and temperature. However, when applied on turbid, light scattering media, the accuracy of laser sheet imaging (and techniques based thereon) is significantly reduced. The inaccuracy can be attributed to three phenomena known as laser extinction, signal attenuation and multiple light scattering. The work presented in this thesis is motivated by these challenges, with the overall aim of making laser sheet imaging applicable for studies of optically dense media. High-pressure, liquid atomizing spray systems, used for combustion purposes, are typical examples of such media. Here sprays are used to disintegrate liquid fuel into fine droplets, which evaporate and burn, an approach which is essential to generate the mechanical power needed for all combustion-based vehicles, such as cars and trucks. Accurate characterization of these multiphase, dense, turbulent spray systems is key in order to reduce pollutions and to improve combustion efficiency.

To enable the utilization of laser sheet imaging in optically dense environments a novel 2D imaging technique named Structured Laser Illumination Planar Imaging (SLIPI) has been developed. The method is based on planar laser imaging but uses a sophisticated illumination scheme - spatial intensity modulation - to differentiate between the intensity contribution arising from directly- and multiply scattered light. By recording three images, between which this encoding is altered in a way only noticeable for the directly scattered light, the approach enables the suppression of the undesired diffuse light intensity contribution.

This thesis presents convincing experimental evidence that SLIPI leads to improved and enhanced visualization up to an optical depth of $\sim$6, thus improving the range of applicability by a factor of $\sim$150 (in terms of light transmission). Also presented herein are solutions to acquire instantaneous SLIPI images of rapidly moving samples, a key feature in order to study dynamic transient spray behavior. It is imperative for accurate instantaneous imaging of turbulent flows that the sample remains static during the time of acquisition, which is experimentally challenging since the SLIPI technique requires three realizations.

Based on the SLIPI method, several quantitative imaging techniques have also been developed within the framework of this thesis, all designed to measure the extinction coefficient. This optical property contains information related to both particle size and number density and is thus of great importance for spray characterization. Moreover, since the extinction coefficient is the origin for both laser extinction and signal attenuation, accurate readings of this parameter by means of SLIPI makes the methods almost completely unaffected by the three previously mentioned sources of error associated with laser sheet imaging.

The SLIPI technique is relatively inexpensive - the cost does not exceed an ordinary laser sheet arrangement noticeably - and can be combined with several other linear imaging techniques. These characteristics can be of great benefit for the spray community, in particular by providing accurate and reliable input data for spray modelers.

Populärvetenskaplig Sammanfattning

Människors sätt att visualisera objekt bygger på en del underliggande principer som man kanske inte alltid reflekterar över. Det faktum att vi har just två ögon gör det till exempel möjligt för oss att avgöra på vilket avstånd ett objekt befinner sig. Detta kallas för parallaxeffekten. Kameror, som bara har ett "öga", saknar denna förmåga, vilket försvårar avbildande mätningar i många forskningssammanhang. För att kringgå detta kan man eliminera behovet av djupseende, genom att belysa sitt prov på ett smart sätt med hjälp av den s.k. laserarksmetoden.

Ett laserark är en lövtunn ljusspalt och när den interagerar med det provmaterial man önskar undersöka, uppstår en ljussignal endast på ett förutbestämt avstånd. Fördelen är att kameran då inte behöver ha något djupseende. Detta är en av de mest beprövade mätmetoderna inom många olika forskningsfält och fungerar utmärkt så länge provet man ska studera inte är grumligt. Ett sådant ljusspridande prov skapar nämligen signaler som kan komma från andra avstånd än det förutbestämda. Detta fenomen kallas multipelspridning och innebär helt enkelt att en del av de fotoner (ljuspartiklar) som detekteras har interagerat upprepade gånger med provmaterialet. Problemet är att vår kamera, som saknar djupseende, tolkar det som att alla fotoner kommer från det plan som belyses av laserarket. Resultatet av det hela blir en bild med en del skarpa och en del suddiga konturer. Ibland, beroende på hur grumligt provet är, skapas även nonsenssignaler. Dessa felkällor gör att laserarksmetoden inte är särskilt applicerbar inom alla områden och för dessa områden saknas dessvärre liknande metoder som samtidigt uppvisar laserarksmetodens beskrivna fördelar.

Denna avhandling beskriver utvecklingen av en ny mätteknik som bygger på laserarksmetoden, men som gör det möjligt att undertrycka det oönskade multipelspridda ljuset. Minskandet av detta ljus, som orsakar både nonsenssignalerna och de suddiga konturerna, ger en ökad mätnoggrannhet. Metoden bygger på att ge laserarket en viss förutbestämd egenskap, som endast de direktspridda fotonerna kan bibehålla under sin färd genom mätobjektet. På så vis kan man med stor säkerhet avgöra vilka delar av bilden som innehåller relevant information.

Metoden, som kallas Structured Laser Illumination Planar Imaging (SLIPI), har huvudsakligen använts för att studera sprayer. Sprayer används inom många olika fält, men det kanske största användningsområdet är inom bil- och flygindustrin. Här används sprayer för att omvandla flytande bränsle till en brännbar gas. Denna process är ytterst komplicerad och ännu inte helt förstådd eftersom sprayer är svåra att undersöka. Anledningen till detta är att sprayer är optiskt grumliga, i och med att de utgörs av en icke-homogen samling droppar, som ger upphov till multipelspridning. Dessutom rör sig dessa olikstora droppar väldigt snabbt, vilket kräver att man belyser och detekterar det spridda ljuset under så kort tid som en miljondels sekund.

Vanligtvis är detta inget problem eftersom standardlasersystem kan generera extremt korta laserpulser (i storleksordningen nanosekunder). Dock kräver SLIPI att man utför tre mätningar för att kunna undertrycka multipelspridningen, vilket försvårar situationen. I avhandlingsarbetet beskrivs bl.a. olika tillvägagångssätt för att lösa detta problem.

Ett annat vanligt problem som uppstår när man försöker mäta på ett grumligt medium är att ljusintensiteten snabbt avtar med avståndet p.g.a. spridning och/eller absorption. Detta gör att mediets alla delar inte belyses lika starkt. Föreställ dig exempelvis en spray som belyses med ett laserark, som består av 100 fotoner och som under sin färd genom sprayen interagerar med 100 identiska droppar. För enkelhetens skull säger vi att varje droppe sprider 1% av den ljusintensitet som infaller mot den. Under dessa förhållanden kommer den första droppen således träffas av 100 fotoner, medan den sista droppen endast belyses med 37 fotoner. Med andra ord, trots att dropparna är identiska kommer signalen från dem skilja sig med en faktor 3, vilket kan medföra feltolkningar. Avhandlingen beskriver olika mätmetoder för att kompensera för denna förlust. Metoderna baseras i korta drag på att mäta mediets förmåga att dämpa ljus istället för dess förmåga att sprida ljus. Detta gör att varje enskild droppe i ovanstående exempel skulle få värdet 0.01, d.v.s. en procent. Härmed undviks feltolkningen som kan uppstå p.g.a. intensitetsförlusten.

Dessa metoder, inkluderande SLIPI, har tillämpats på ett flertal olika sprayer och resultaten har jämförts med laserarksmetoden. Resultaten är mycket lovande, både vad gäller mätnoggrannhet och reproducerbarhet. En stor fördel med SLIPI är även att tekniken kan kombineras med många andra sedan tidigare utvecklade mätmetoder.

SLIPI kan användas inom många olika områden men spraystudier är och kommer säkert förbli, den största tillämpningen för SLIPI. Med teknikens förmåga att undertrycka multipelspritt ljus, kan den användas för att undersöka tidigare outforskade delar av en spray och därmed bidra till ökad förståelse för hur sprayer fungerar. Utveckling av SLIPI är därför högst relevant för bil- och flygindustrin, där man ständigt strävar efter att förbättra och förfina sprayprocessen.

List of Papers

   I. **Kristensson, E.**, Richter, M., Pettersson, S.-G., Aldén, M. and Andersson-Engels, S., *Spatially resolved, single-ended two-dimensional visualization of gas flow phenomena using structured illumination*, Appl. Opt., **47**, 3927-3931, 2008.

  II. **Kristensson, E.**, Berrocal, E., Richter, M., Pettersson, S.-G. and Aldén, M., *High-speed structured planar laser illumination for contrast improvement of two-phase flow images*, Opt. Lett., **33**, 2752-2754, 2008.

 III. Berrocal, E., **Kristensson, E.**, Richter, M., Linne, M. and Aldén, M., *Application of structured illumination for multiple scattering suppression in planar laser imaging of dense sprays*, Opt. Express, **16**, 17870-17881, 2008.

 IV. **Kristensson, E.**, Berrocal, E., Richter, M. and Aldén, M., *Nanosecond structured laser illumination planar imaging for single-shot imaging of dense sprays*, Atomization Sprays, **20**, 337-343, 2010.

  V. **Kristensson, E.**, Berrocal, E., Wellander, R., Richter, M., Aldén, M. and Linne, M., *Structured illumination for 3-D Mie imaging and 2-D attenuation measurements in optically dense sprays*, 33rd International Symposium on Combustion, 2010.

 VI. **Kristensson, E.**, Berrocal, E. and Aldén, M., *Extinction coefficient imaging of turbid media using dual structured laser illumination planar imaging*, Opt. Lett., **36**, 1656-1658, 2011.

VII. **Kristensson, E.**, Araneo, L., Berrocal, E., Manin, J., Richter, M., Aldén, M. and Linne, M., *Analysis of multiple scattering suppression using structured laser illumination planar imaging in scattering and fluorescing media*, Opt. Express, **19**, 13647-13663, 2011.

VIII. Wellander, R., Berrocal, E., **Kristensson, E.**, Richter, M. and Aldén, M., *Three-dimensional measurement of the local extinction coefficient in a dense spray*, Meas. Sci. Technol., **22**, 125303 (15pp), 2011.

 IX. **Kristensson, E.**, Berrocal, E. and Aldén, M., *Quantitative 3D imaging of scattering media using Structured Illumination and Computed Tomography*, Submitted to Opt. Express.

  X. Berrocal, E., Johnsson, J., **Kristensson, E.** and Aldén, M., *Single scattering detection in turbid media using single-phase structured illumination filtering*, Submitted to Laser Phys. Lett.

XI. Berrocal, E., **Kristensson, E.**, Hottenbach, P., Aldén, M. and Grünefeld, G., *Quantitative imaging of a non-combusting Diesel spray using SLIPI*, Submitted to Appl. Phys. B.

Related Work

A. Persson, L., **Kristensson, E.**, Simonsson, L. and Svanberg, S., *Monte Carlo simulations of optical human sinusitis diagnostics*, J. Biomed. Opt., **20**:5, 2007.

B. Persson, H., Sjöholm, J., **Kristensson, E.**, Johansson, B., Richter, M. and Aldén, M., *Study of Fuel Stratification on Spark Assisted Compression Ignition (SACI) Combustion with Ethanol Using High Speed Fuel PLIF*, SAE Technical Paper 2008-01-2401, 2008.

C. Sjöholm, J., **Kristensson, E.**, Richter, M., Aldén, M., Göritz, G. and Knebel, K., *Ultra-high-speed pumping of an optical parametric oscillator (OPO) for high-speed laser-induced fluorescence measurements*, Meas. Sci. Technol., **20**, 025306 (7pp), 2009.

D. Berrocal, E., **Kristensson, E.**, Richter, M., Linne, M. and Aldén, M., *Multiple scattering suppression in planar laser imaging of dense sprays by means of structured illumination*, Atomization Sprays, **20**, 133-139, 2010.

Contents

Abbreviations

Ballistic Imaging	BI
Charged Coupled Device	CCD
Computed Tomography	CT
Continuous Wave	CW
Depth-of-field	DOF
Dye Cuvette	DC
Field-of-view	FOV
Filtered-backprojection	FBP
Full Width at Half Maximum	FWHM
GAs in Scattering Media Absorption Spectroscopy	GASMAS
Gasoline Direct Injection	GDI
Interferometric Laser Imaging for Droplet Sizing	ILIDS
Internal Combustion	IC
Laser Induced Phosphorescence	LIP
Laser Sheet Dropsizing	LSD
LIght Detection And Ranging	LIDAR
Micro-Channel Plate	MCP
Molecular Tagging Velocimetry	MTV
Nitrogen Oxides	NO_x
Numerical Aperture	NA
Optical Transfer Function	OTF
Particle Image Velocimetry	PIV
Particle Tracking Velocimetry	PTV
Phase Doppler Anemometry	PDA
Photo-Multiplier Tube	PMT
Planar Droplet Sizing	PDS
Planar Laser Imaging	PLI
Planar Laser Induced Fluorescence	PLIF
Region Of Interest	ROI

Root Mean Square	RMS
Sauter Mean Diameter	SMD
Scanning Confocal Microscopy	SCM
Signal-to-Noise Ratio	S/N
Single Plane Illumination Microscopy	SPIM
Spark Ignition	SI
Start Of Injection	SOI
Structured Illumination	SI
Structured Illumination Microscopy	SIM
Structured Laser Illumination Planar Imaging	SLIPI
Structured Laser Illumination Transmission Imaging	SLITI
Top Dead Center	TDC
Ultra-Violet	UV

Chapter 1

Introduction

THE utilization of spray systems is a necessity in modern society. Most people associate sprays with their day-to-day life usage of these systems, for instance in the shower or in front of the mirror when styling their hair. However, the most frequently encountered sprays are the naturally created ones, such as rain.

Within industry, sprays are used for cleaning, applying chemicals, medical treatments, cooling, producing soot, coating, misting, drying *etc.* [1]. With the previously commonly used extinguishing agent Halon now being banned from production, water sprays have become a vital tool for fire suppression [2]. Spray painting is another important industrial application, as is the utilization of sprays for delivering fuel for combustion purposes. Each area of application requires its unique tuning of the spray characteristics, where droplet size, velocity, spatial distribution, angle of dispersion and number density are key factors. Failure in attaining the optimum operating conditions can have severe consequences, both economically and environmentally. For instance, the pollution generated by paint missing its target when sprayed onto a vehicle can exceed the pollution generated by the engine powering the vehicle itself during its entire lifetime [1]. The tuning process involved when seeking the optimum spray characteristics is sometimes based purely on trial and error, an expensive approach which calls for reliable and accurate measurement techniques. This has spurred the development of optical (light-based) diagnostics that, opposed to mechanical or electrical devices, provide the user the opportunity of performing remote non-intrusive measurements. Nowadays there is a substantial variety of optical instruments available, some designed specifically for a single task, others being capable of measuring several quantities simultaneously.

Perhaps the most versatile optical probing technique is laser sheet imaging, which constitutes the basis for numerous other light-based techniques. The unique feature of laser sheet imaging which makes it attractive for spray studies is its capability of producing optically sectioned images, meaning that the signal originates only from a thin "optically selected" region. This attribute distinguishes laser sheet imaging from other available imaging techniques which usually rely on path-integrated data. Due to the three-dimensional nature of sprays, the sectioning approach renders fewer uncertainties when analyzing the results.

Spray systems generate, in general, a polydisperse and inhomogeneous ensemble of droplets. Most optical probing techniques perform satisfactory when the number density of droplets is low. However, when the number density increases beyond a certain limit the cloud of droplets becomes *optically dense*, meaning that the penetrability of photons is significantly reduced. Acquiring accurate, noise-free data from any type of optically dense light scattering media using optical techniques is far from trivial. In such environments a large fraction of the incident photons interact more than once with the illuminated sample. This is called *multiple light scattering* and is one the most important sources of error when probing turbid scattering media. For imaging techniques multiple light scattering causes blur and erroneous signal levels. This, in turn, leads to misinterpretations and inaccurate results. Due to its detection arrangement, conventional laser sheet imaging is unfortunately especially prone to collect these undesired multiply scattered photons, making the technique restricted to less turbid media.

The aim of the work presented in this thesis has been to develop means to solve the issue of multiple light scattering experimentally and to enable the utilization of laser sheet imaging in complex turbid environments, such as dense sprays. This has been successfully accomplished by employing a special type of illumination scheme that allows singly scattered photons to be distinguished from the multiply scattered ones. This approach, which has been given the name Structured Laser Illumination Planar Imaging (abbreviated SLIPI), and its applications for spray diagnostics is the topic of this thesis.

1.1   Outline of the Thesis

The outline of this thesis is as follows:

Chapter 2 provides an introduction to the spray formation process for high-pressure injection systems. The physics involved in this so-called atomization process are briefly discussed and some important applications are described.

Chapter 3 describes light-matter interaction and introduces the concept of optical turbidity. The most common sources of error experimentalists encounter when probing turbid media - *laser extinction*, *signal attenuation* and *multiple light scattering* - are also described.

Chapter 4 provides a review of the most frequently used imaging techniques in the field of spray diagnostics. The most advanced optical probing techniques - X-ray absorption and Ballistic imaging - are also described.

Chapter 5 makes a short detour to the field of microscopy to give a detailed description of the structured illumination technique, which constitutes the link between planar laser imaging and the SLIPI method.

Chapter 6 presents the main results and achievements of the work carried out within the framework of this thesis. All results are not included as a full account of all experiments are instead found in the appended papers.

Chapter 7 provides practical information and recommendations for those readers who intend to carry out SLIPI measurements themselves. A typical experimental arrangement of SLIPI is presented and the purpose of the optical components involved in the setup is explained. Experimental and computational solutions to the most commonly encountered problems are also given.

Chapter 8 aims at illustrating the versatility of SLIPI and includes material yet to be published.

Chapter 9 concludes and summarizes the presented work.

Part I

Background

Chapter 2

Spray Characteristics

T HIS chapter provides a brief introduction to the spray formation process, with primary focus on sprays generated using high-pressure liquid injection strategies. The modern view of the physical processes governing liquid atomization is presented and the important measurement parameters which are relevant for the characterization of spray systems are discussed.

2.1 Background

A spray is defined as a system containing individual liquid droplets that evolve in a surrounding gaseous medium [3]. The applications of these systems are numerous, including areas such as field treatment with pesticides within agriculture, inhalation of drugs within medical therapy, delivery of fuel for combustion purposes, spray painting [1]. The spray characteristics striven after in each application depends on the specific need. For instance, the drug-carrying droplets inhaled in the treatment of asthma must be made sufficiently small to penetrate through the throat and bronchial passageways to finally deposit on the surface of the lungs, but large enough to avoid immediate exhalation of the medicine. Regardless of the application, it can be stated that the efficiency of the process relies on the control of the spray formation.

The largest application of liquid sprays, and also the area in which most research has been conducted, concerns the delivery of fuel in internal combustion (IC) engines, e.g. diesel engines. In such cases, the liquid is issued with high pressure through a narrow orifice into the combustion chamber where it, due to turbulence and instabilities, disintegrates into fine droplets which vaporize and eventually burn. This process is referred to as the *atomization* of the liquid. Despite decades of scientific efforts and thorough investigations, the physics governing this transition between liquid and vapor is not fully understood. One of the main reasons for this lack of understanding is due to the large number of droplet and irregular liquid ligaments generated near the nozzle outlet, making the region almost impenetrable to light. This is problematic since the majority of diagnostic tools available for spray studies today are based on laser radiation (or, alternatively, non-chromatic radiation). Laser-based diagnostics are preferable over techniques based on physical probes because of their non-intrusive nature. Furthermore, by using pulsed lasers, measurements can be performed on a

time scale short enough to freeze the flow of the atomizing liquid in time, which is of fundamental essence for the understanding of dynamic transient spray behavior. Some of the most commonly applied spray diagnostics are described in Chapter 4.

2.2 Spray Structure

As a consequence of the limited knowledge of the atomization process various views on the spray structure can be found in the literature. However, a common aspect is to divide the overall structure in two parts; the region close to the orifice and the downstream region. The former is frequently referred to as the *dense spray region*, while the latter is recurrently denoted the *dilute spray region*[1] [4]. The names stem from the fact that a dense cloud of droplets are commonly formed near the nozzle outlet, while further downstream this cloud has dispersed and become dilute. From an engineering point of view, this classification is useful and serves its purpose. However, from an optical diagnostic point of view, this terminology may render some confusion since the dense region of some sprays can be *optically dilute* and *vice versa*. The concept of optical turbidity is discussed in further detail in the following chapter. In an attempt to avoid such confusion, the terms *spray formation region* and *spray regions* will be used throughout this thesis instead. The aim of these terms is to distinguish between optical characteristics and spray phenomena.

2.2.1 Atomization Process

Figure 2.1 illustrates the conceptual model of the spray formation used throughout this thesis. The spray production can be generalized by three steps; (1) the ejection of liquid into a gaseous medium, (2) the so-called *primary breakup* mechanism, which is followed by (3) the *secondary breakup* mechanism [3]. For high-pressure injection systems, the formation of droplets was historically explained by the presence of an intact liquid core that extended far downstream of the nozzle. In the boundary layer of the liquid core, liquid ligaments and large droplets were stripped off and sequentially broken up into finer droplets. Although the presence of an intact liquid core (at high injection pressures) is still somewhat debated, the modern view of the process is that the liquid jet undergoes atomization almost directly as it emerges from the nozzle outlet, and remains intact, at most, only a few nozzle diameters [4].

The spray formation region constitutes the initial formation of isolated liquid elements as well as their subsequent fragmentation into smaller droplets. The initial creation of liquid ligaments are thought to be initiated by deformations in the interface between the liquid core and the surrounding gas, caused by turbulence or variations in the liquid flow velocity. With time these deformations grow, eventually leading to the ejection of an isolated liquid body - the primary breakup. Collisions between these ligaments as well as coalescence (merging) may occur but sequentially they disintegrate until stable isolated spherical droplets are formed - the secondary breakup process. The remainder (downstream region) of the spray constitutes the spray region. One important characteristic of this region is that the intensity of a light beam traversing the spray here reduce exponentially, via scattering, according to the Beer-Lambert law. This is discussed further in Chapter 3.

---

[1]The terms *near-field region* and *far-field region* are also frequently used.
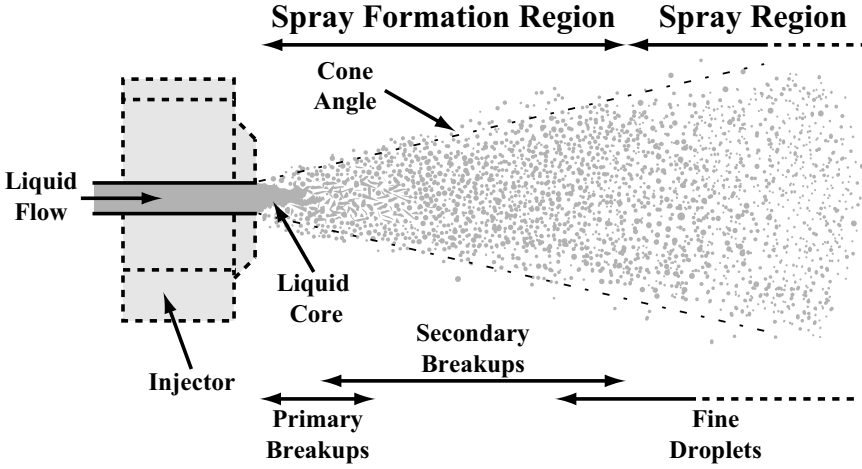
Figure 2.1: *Illustration of the spray formation process and the different spray regions.*

2.2.2 Cavitation

One possible explanation for the onset of the disturbances causing the initial rupture of the liquid core is the creation of vapor cavities in the internal flow. This phenomena is known as *cavitation* and is strongly coupled to the injection pressure and the internal design of the nozzle. The internal geometry of high-pressure cylindrical jets consists, in general, of a tube with an inner diameter D in which the fuel is delivered. The liquid is then forced through a cylindrical tube with a diameter d, where $d < D$, and of length L. If the transition between the tubes is sharp, the liquid will be subjected to a rapid change in pressure. Should the pressure drop below the vapor pressure of the liquid gas will be formed. Figure 2.2 illustrates how the creation of these cavities depend on the geometrical design of the nozzle and the injection pressure. In these measurements, which were performed by Hiroyasu *et al.*, cavitation was not observed for a short ($L/d = 0$) or rounded-inlet nozzle (Fig. 2.2 a) and b)), regardless of the operating condition. Cavitation first appeared when sharp-inlet nozzles with adequately large L were employed (dashed lines in Fig. 2.2 c)). The authors further demonstrated that the extension of these cavities increased with pressure, as shown in Fig. 2.2 d), leading to improved atomization. However, when the cavitating region expanded further, a significant reduction in the atomization efficiency was noted (Fig. 2.2 e)). This behavior was called *super-cavitation* and occurs when the cavity extends over the entire inlet tube, leading to reduced wall friction and, consequently, reduced turbulence of the emerging liquid [5].

The influence of the internal geometry on atomization has spurred the development and visualization of transparent nozzles and similar findings as those presented in Fig. 2.2 can be found in the literature (see [3] and references therein). However, exactly how cavitation affects the sequential breakup process is still not fully understood, partly due to the experimental challenges associated with measurements in the spray formation region.
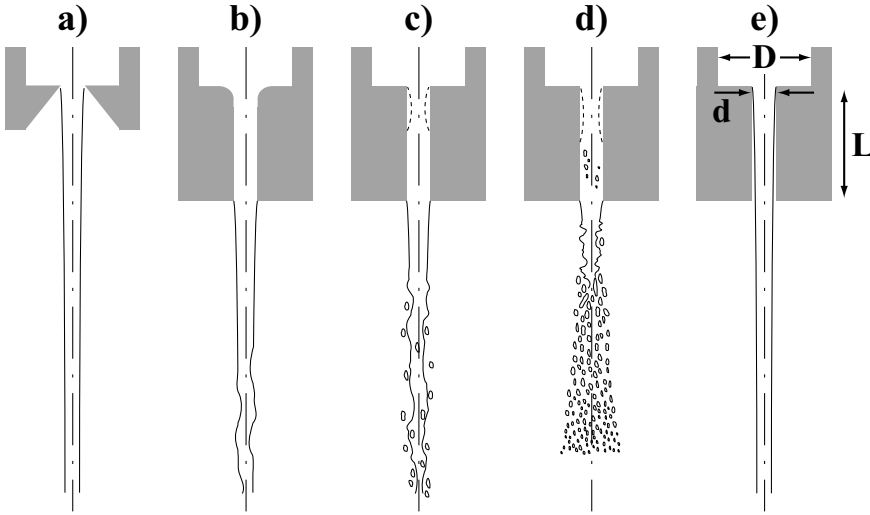
Figure 2.2: *The influence of the internal nozzle design and pressure (increasing from left to right). Adapted from [5].*

2.3 Measurement Parameters

To quantify the end performance and overall effectiveness of an atomizing spray system, the most important parameters to experimentally measure are [3]:

- Droplet-size distribution

- Droplet-velocity distribution

- Droplet density (number per unit volume)

- Spatial distribution of droplets

- Droplet temperature

These, in turn, depend on a variety of factors such as injection pressure, ambient density, liquid viscosity, air motion and turbulence, internal geometry of the nozzle, orifice diameter, temporal profile of the pressure, *etc* [4]. Various techniques to measure some of the desired parameters are provided in Chapter 4. However, it should be pointed out that only a few of these quantities can be readily accessed, even in the spray region, due to issues caused by light scattering and/or absorption. To avoid these experimental difficulties yet still be able to compare different measurement cases and operating conditions quantitatively, a common routine is to observe variations in more easily attainable spray parameters. The most common are *cone angle* (ϕ_c) and *liquid penetration length* (L_p).

The cone angle, also referred to as the spray angle, defines the (average) spreading of the liquid. Experimental evidence indicates that ϕ_c is highly coupled to the injection pressure and internal design of the nozzle [6]. The cone angle can be measured

using various approaches, such as laser sheet imaging (see Chapter 4.1) or shadow-graph imaging. It should, however, be pointed out that the results obtained using different optical techniques are not always directly comparable [7].

The liquid penetration length is a measure of the distance (from the injector) the liquid-phase propagates before complete vaporization has occurred. This length is especially important for in-cylinder engine applications because the entrainment of air into the jet is mainly taking place during this passage. The liquid penetration length thus influences the fuel/air mixing and, consequently, the subsequent combustion. However, over-penetration leading to wall impingement is highly undesired as it can render elevated levels of unburned hydrocarbons in the exhaust gas (and, in extreme cases, wash off the lubricating oil film on the cylinder liner). It has been demonstrated experimentally that L_p is highly sensitive to the orifice diameter [8]. By decreasing the outlet dimension, the penetration of liquid reduces linearly. The determination of L_p is accomplished by illuminating the spray and visualizing the scattered light [9]. As liquid undergoes vaporization, the scattering cross-section (see Chapter 3) reduces significantly, leading to a significant drop in photon counts between the liquid-phase and the gas-phase. L_p is then evaluated by applying an intensity threshold on the recorded image. The main uncertainty associated with the determination of L_p concerns the choice of the threshold value, especially when the border between the two phases is indistinct. Also, different camera systems have different characteristics (sensitivity, resolution, gain-curves *etc.*), which should be taken into account in the evaluation of L_p.

2.4   Spray Applications

2.4.1   Diesel Engine

In a diesel engine air is introduced into the cylinder in the intake stroke. When the piston is near top dead center (TDC) fuel is injected with high pressure ($\sim$2000 bar), followed by a rapid atomization process in which the liquid fuel disintegrates and evaporates. As the fuel is mixed with the compression-heated air spontaneous ignition occurs. A high compression ratio (14:1 - 20:1) is required for this process, as the air temperature must be sufficient for auto-ignition. The combustion does, however, not start immediately at start of injection (SOI) - the process is slightly delayed. This delay depends on the spray dispersion and evaporation processes, temperature history as well as on the intrinsic auto-ignition properties of the fuel. During the delay, evaporated fuel mixes with the air and when ignition eventually takes place, premixed and mixing-controlled combustion occur simultaneously. One advantage of the diesel concept is that the power generation is only governed by the amount of fuel injected into the cylinder, thereby circumventing the need for throttling the air flow, which is a requirement for ordinary gasoline engines. This results in reduced pumping losses and thus good mechanical efficiency. Furthermore, the high compression ratio results in a high thermal efficiency of the diesel cycle, although the engine must be constructed more robustly as it is subjected to both higher pressure and higher pressure raise rates compared to the spark-ignited (SI) Otto engine [10, 11].

Compared to SI engines, the diesel cycle produces a reduced amount of CO_2 but suffers from elevated particulate and NO_X emissions, which is why this engine concept

is avoided in e.g. the United States[2]. Laser diagnostics have played an important role in the understanding of the diesel combustion process. One example is the work performed by John Dec [12], who (during eight years!) gathered information by applying various laser-based techniques on a diesel spray. The investigations led to a new conceptual model for the diesel combustion process.

The main obstacle when attempting to employ laser diagnostics for the study of diesel sprays is the high concentration of droplets produced in the process. This makes it difficult for photons to penetrate into the central region of the spray without being scattered. The scarce number of photons succeeding in this task face the same obstacle as they try to escape from the core of the spray, reducing the number even further. For this reason almost no information can be found in the literature describing the physical processes occurring in the interior of a diesel spray.

2.4.2 Gasoline Direct Injection Engine

The most common gasoline engine is the Otto engine, where fuel and air are mixed before being introduced into the cylinder. The mixture is compressed and ignited by a spark plug as the piston approaches TDC. Because this combustion concept is not spray driven, it is not discussed in further detail. A second type of Otto engine which, instead of using port-injection, employs direct-injection (DI) of the fuel, is the so-called Gasoline Direction Injection (GDI) engine. The overall purpose of the GDI concept is to enable the engine to run with an abundance of air (lean fuel/air mixture). As in a diesel engine, the load is (ideally) controlled by varying the amount of fuel injected into the cylinder and not by throttling the intake air. This reduces pumping work losses, yielding a higher efficiency at low loads. An abundance of air furthermore lowers the production of NO_X [10]. However, the use of a lean mixture eliminates the possibility of igniting the fuel charge with an electrical spark. To solve this issue the geometry of the combustion chamber must be designed in such a way that a stratified (stoichiometric or slightly rich) charge is produced near the spark plug during ignition. Combustion then starts in these richer regions and spreads to leaner zones, eventually consuming the entire fuel charge. The correct operation of a GDI engine requires proper knowledge regarding the fuel injection, spray atomization, vaporization, in-cylinder flow conditions and spray impingement.

The injection timing is crucial for the GDI combustion process to proceed optimally. Early SOI increases the fuel/air mixing, leading to over-lean regions that do not burn. Late injection has the opposite effect, creating fuel-rich zones that give rise to soot and unburned hydrocarbons in the exhaust. In addition, late SOI often leads to fuel deposits on the piston due to spray impingement that consequently result in an aggravated emission of hydrocarbons. Even at its optimum, GDI engines suffer from emissions of particles and unburned hydrocarbons. Furthermore, even though the production of NO_X is relatively low, the emission levels are still higher than for ordinary SI engines because three-way catalysts do not operate efficiently for lean mixtures [10, 11].

---

[2]NO_X emissions produces smog, which has become a serious issue in the USA.

2.4.3 Fire Suppression

Until 1987 Halon was the primary choice for fire suppression, due to its ability to inhibit the chemical reactions occurring in combustion [2, 13]. However, due to its negative impact on the environment (ozone depletion and long atmospheric lifetime), this gaseous agent is now banned from production, with only a few exceptions such as for military-, aviation- and nuclear industry purposes. Since then, extensive efforts have been made to find optional means of active fire protection, where the use of water spray systems are considered to be one of the most promising alternatives.

Fire extinguishing by means of water mist systems is, however, a fairly complicated process. Its effectiveness is affected by a variety of factors such as water flow rate, nozzle type, droplet diameter, location of sprinkler head, ventilation condition, combustion reaction characteristics and properties of the burning material [14]. There is currently insufficient knowledge to assess the optimum combination of these factors. For instance, a spray producing a large number of very small droplets lead to a larger surface area than a flow with fewer but larger drops. A large surface area could be beneficial for fire suppression as it abstracts more of the generated heat, increasing the chance for extinction. However, small drops are quickly slowed down after leaving the nozzle, increasing the risk of them being carried away by the strong convection currents produced by the fire [15]. For this reason, some scientists counter-argue that larger droplets with a greater momentum are preferred, as these can penetrate the fire plume and cool the burning surface.

To understand the physical processes governing the suppression of fires using water mist systems, it is imperative to properly characterize the properties of the employed spray system, which calls for accurate and reliable probing techniques.

Chapter 3

Light Interaction With Sprays

THIS chapter is devoted to a brief description on how light interacts with matter, mainly focusing on scattering. The concept of optical turbidity is introduced, an essential part in order to understand the problems that arise when probing dense atomizing sprays. The important effects known as *laser extinction*, *signal attenuation* and *multiple light scattering* are also described.

3.1 Light Extinction

Intensity, also referred to as specific intensity, radiance or brightness, is defined as follows [16]: Let dE_λ represent the amount of radiant energy in a wavelength interval $(\lambda, \lambda + d\lambda)$ transported through the area dA within the solid angle $d\omega$ over a time interval dt. The intensity is defined as

$$I_\lambda = \frac{dE_\lambda}{\cos\theta \cdot d\lambda \cdot dA \cdot dt \cdot d\omega} \tag{3.1}$$

where θ denotes the angle between the beam of radiation and the normal to the area dA. The unit of the intensity is thus W/(m^2 ster Å). Usually the wavelength dependence is not considered but rather the integrated intensity over all wavelengths is used, in which case the subscript λ is omitted. The Beer-Lambert law describes how the intensity of a beam of light changes as it propagates through a turbid medium. Consider the case presented in Fig. 3.1, where a beam of radiation propagates through an element volume with attenuating particles. As the light travels the distance dx, a part of the intensity, dI, will be lost. The amount depends on the attenuating particles according to

$$dI = -\mu_e \cdot I \cdot dx \tag{3.2}$$

where μ_e is the *extinction coefficient* (m^{-1}), which, by convention, is set as positive. Integrating Eq. 3.2 over the distance x leads to

$$I(x) = I(0) \cdot \exp\left(-\int_0^x \mu_e(x) \cdot dx\right) \tag{3.3}$$

which is the Beer-Lambert relation[1], stating that the intensity decreases exponentially with distance and μ_e as it travels through an object consisting of light-attenuating elements. For a homogeneous sample, i.e. constant extinction of light, with a thickness L the expression simplifies to a single exponential decay and the transmitted light intensity can be calculated according to

$$I(L) = I(0) \cdot \exp\left(-\bar{\mu}_e \cdot L\right) \tag{3.4}$$
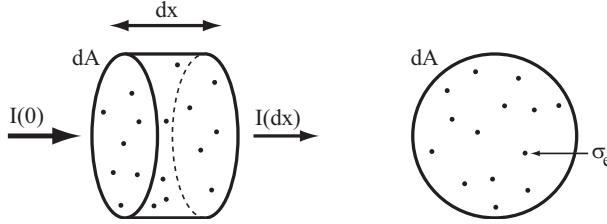

Figure 3.1: *An element volume consisting of light-attenuating particles. Attenuation occurs through scattering and/or absorption.*

The attenuating particles in the slab shown in Fig. 3.1 each present an effective extincting area σ_e (m^2). This area is referred to as the *extinction cross-section* and relates the extinction coefficient to the number density N (number of particles per m^3) according to

$$\mu_e = \sigma_e \cdot N \tag{3.5}$$

Note however, that the effective area σ_e differs from the geometrical cross-section area G of the particle (for the case of spherical particles of diameter D, $G = \pi \cdot D^2/4$). Instead, these are related through the *extinction efficiency* Q_e [17], given by

$$Q_e = \frac{\sigma_e}{G} \tag{3.6}$$

The value of Q_e varies depending on the wavelength of light and G. However, when considering the typical droplet sizes generated by atomizing spray systems ($D \gtrsim 20$ µm) illuminated by visible light, Q_e can be approximated to 2 [18].

There are two main conditions for the validity of Eq. 3.3; (1) the linear scale of the extinction cross-section, i.e. $\sqrt{\sigma_e}$, has to be small in comparison to the average interparticle distance and (2) the attenuators have to be randomly distributed [16]. In the spray formation region, these conditions are not fulfilled and the use of the Beer-Lambert law to deduce optical characteristics may render erroneous results. Therefore, Eq. 3.3 should mainly be used to analyze measurements performed in the spray region where isolated spherical droplets have been formed.

3.2   Light Scattering

So far, extinction of light has only been treated as a general phenomenon without considering the physics governing it. Extinction of light can occur through either

---

[1]Also known as the Lambert-Beer law or simply Beer's law.

scattering and/or absorption. As for the total extinction, each individual process is characterized by a given coefficient (μ), cross-section (σ) and efficiency (Q). These are coupled to the total extinction parameters through

$$\mu_e = \mu_s + \mu_a \tag{3.7}$$

$$\sigma_e = \sigma_s + \sigma_a \tag{3.8}$$

$$Q_e = Q_s + Q_a \tag{3.9}$$

Each coefficient is related to the number density N via the respective cross-section, according to

$$\mu_s = \sigma_s \cdot N \tag{3.10}$$

$$\mu_a = \sigma_a \cdot N \tag{3.11}$$

Pure absorption will not be discussed further, we will instead focus our attention on light scattering, since this phenomenon is unavoidable when optically probing a spray using visible radiation. Scattering of electromagnetic waves can occur in several different ways and the concept cannot be explained by a single theory. For the work presented in this thesis, only two fields of light scattering are considered, namely *elastic scattering* and *fluorescence*.

3.2.1 Elastic Scattering

Elastic scattering of electromagnetic radiation is the term given to the scattering process in which the wavelength of the incident and scattered light is equal. In a simplified view, the concept is divided into three domains based on the dimensionless particle size diameter x, given by

$$x = \frac{\pi \cdot D}{\lambda} \tag{3.12}$$

The different regimes are provided in Table 3.1. For most types of spray systems, the second case - Mie scattering - is the one of main interest.

Table 3.1: *Three domains of elastic scattering.*

$x \ll 1$	**Rayleigh**: Wavelength large compared to the particle
$x \approx 1$	**Mie**: Wavelength and particle about the same size
$x \gg 1$	**Geometric**: Particle large compared to the wavelength

The physics underlying the process of elastic scattering can be understood by realizing that all matter is composed of discrete electric charges, i.e. protons and electrons. When shone upon, the electromagnetic wave will force these charges to oscillate (at the frequency of the incident wave). This accelerating motion will cause the charges to coherently emit electromagnetic waves in all directions. The newly formed source of radiation (wavelets) is what is referred to as *scattered* light [19].

Figure 3.2: *Scattering of light by a single particle, subdivided into smaller regions. The total scattered intensity at P is the sum of all wavelets generated by each subdivision. Adapted from [19].*
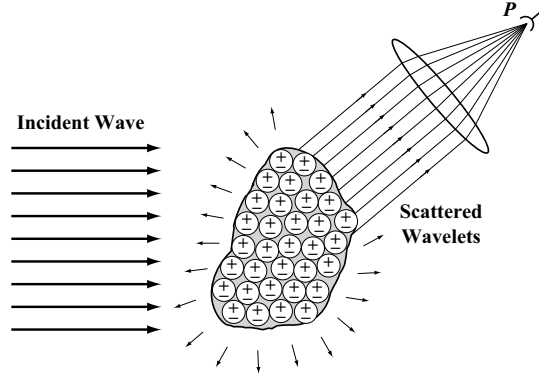
The total intensity detected at a certain position P, see Fig. 3.2, is obtained by superimposing the scattered wavelets. However, since the emitted radiation is coherent the phase of each individual ray must be considered. The phase relation depends on the size and shape of the particle as well as the angle of detection. If the size is small in comparison to the incident wavelength, i.e. the Rayleigh regime, the emitted wavelets are in phase and thus the scattered intensity varies marginally for different scattering angles. The scattering magnitude is, however, highly dependent on the diameter of the particle and is proportional to λ^{-4} [17]. In the opposite case, where the wavelength and the particle size are of comparable dimensions, i.e. the Mie regime, phase mismatch develops and the wavelets interfere constructively or destructively. Hence, in contrast to Rayleigh scattering, Mie scattering is highly angularly dependent and exhibits preferential scattering directions (typically either back- or forward scattering). The different scenarios are illustrated in Fig. 3.3.
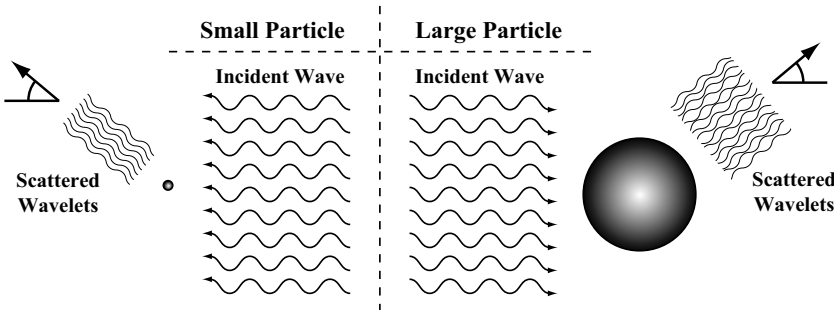
Figure 3.3: *Differences in scattering as light is incident on either a relatively small or large particle.*

Preferential forward scattering will pose a problem when attempting to determine the optical characteristics of a sample by using transmission-based techniques. In such a measurement, both the incident and the transmitted light intensity are recorded and used as input in Eq. 3.3 or 3.4. If the physical dimension L of the sample is known (e.g. a substance contained within a cuvette), the average extinction of light over the distance L can be derived. This approach assumes that only the unperturbed light is detected and that photons interacting with the sample are either absorbed or

scattered into a new direction (and therefore not detected). However, if the incident trajectory is preserved when the photons are scattered, this contribution of light cannot be differentiated from the unperturbed one, leading to an underestimation of the extinction coefficient. Figure 3.4 illustrates how the scattering phase function varies for different (spherical) particle diameters, illuminated by $\lambda = 532$ nm (corresponding to the frequency doubled radiation emitted by a Nd:YAG laser source). Noticeable is the increase in the number of scattering lobes as well as the more pronounced forward scattering peak appearing as the particle diameter increases.
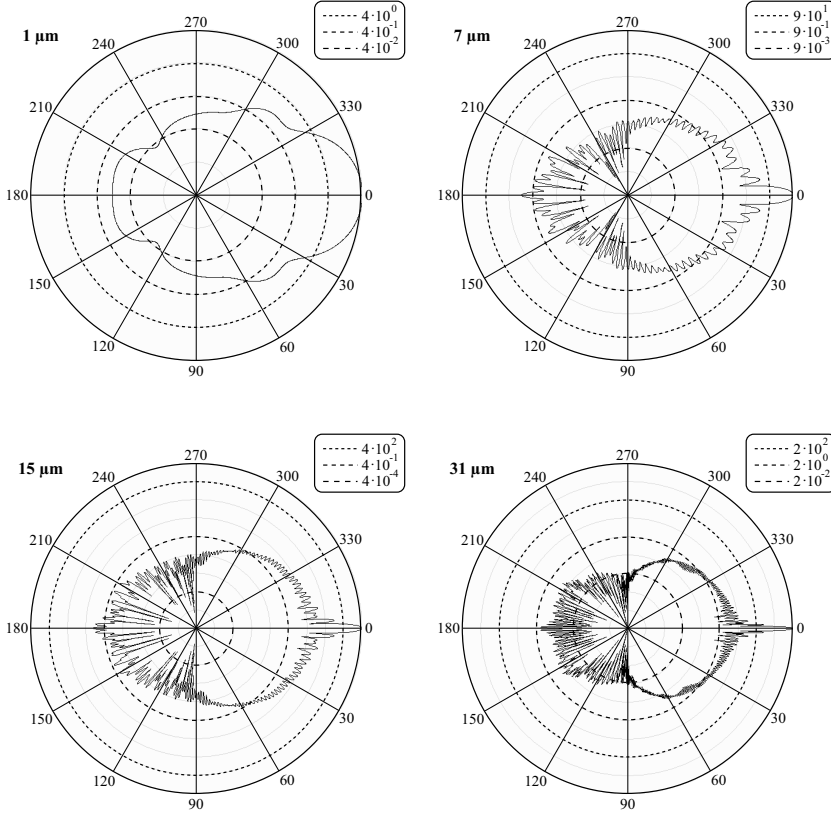
Figure 3.4: *Polar scattering phase functions (logarithmic scale) for a water droplet ($n = 1.33 + 0.0i$) calculated for different diameters ($\lambda = 532$ nm). The circles in each plot indicate the scale.*

3.2.2 Fluorescence

Fluorescence is an inelastic scattering photophysical process in which an atom or molecule gets excited to a higher electronic energy state via the absorption of a photon, after which it relaxes to its ground state through spontaneous emission of radiation. The emitted radiation is primarily redshifted compared to the incident light, which usually consists of a monochromatic laser source, because the process

involves partial de-excitation through non-radiative steps [11]. This is advantageous for experimental work, as it allows the elastically scattered light to be spectrally filtered out prior to detection. The approach is sometimes called "background free" because of this feature. Because each atom or molecule has a unique energy level structure, fluorescence is species specific.

3.3 Turbidity

All opaque, light scattering samples has a certain level of turbidity, which can be described through various parameters such as *scattering orders* and *optical depth* (*OD*).

3.3.1 Scattering Orders

Photons undergoing n scattering events during their passage through the sample are said to be of scattering order n. The unperturbed photons (scattering order 0) are often referred to as *ballistic* and are ideal for shadowgraph imaging as they create a perfect shadow of the sample. Photons which undergo one interaction event - scattering order 1 - are, on the other hand, particularly important for the determination of droplet size, concentration, sphericity *etc*. As the number of interactions increase further, such information can no longer be deduced from the photons. Photons of scattering order 2-9 are sometimes called "snake" photons, stemming from their characteristic snakelike zigzag path through the sample. The photons belonging to scattering orders 10 and above are referred to as "diffuse" [17]. Note however, that the term "diffuse light" is sometimes used in the literature as a general term for photons belonging to scattering orders greater than 2.

In general, quantitative assessments regarding the optical characteristics of the probed sample can be made by means of the Beer-Lambert law if either, for a transillumination measurement, the ballistic light is detected or, for side-scattering, the singly scattered light is recorded.

3.3.2 Optical Depth

The distance of propagation between two light-droplet interaction events is called the *free path length*, l_{fp}. The mean free path length is calculated according to

$$\bar{l}_{fp} = \frac{1}{\mu_e} \tag{3.13}$$

By comparing $\bar{l}_{fp}$ with the actual (geometrical) dimension L it is possible to deduce the number of average free path lengths a photon travels when traversing the sample (Eq. 3.14). The obtained value is an approximation of the number of scattering events occurring in the probed medium and is called the optical depth or the *optical thickness*.

$$OD = L/\bar{l}_{fp} = L \cdot \mu_e \tag{3.14}$$

It can be seen by comparing Eq. 3.14 with Eq. 3.4 that the concept of optical depth is included in the Beer-Lambert law.

$$I(L) = I(0) \cdot \exp\left(-\mu_e \cdot L\right) = I(0) \cdot \exp\left(-OD\right) \tag{3.15}$$

3.3.3 Scattering Regimes

Based on the concept of optical depth, the scattering of light within a turbid medium can be classified into three regimes [20].

Single Scattering Regime

In this regime the average number of scattering events is less than one and the non-scattered ballistic photons are dominant. Under these conditions, a spray is said to be *optically dilute*. For off-axis detection, the single scattering approximation, which assumes that photons have experienced only one scattering event prior to detection, applies.

Intermediate Scattering Regime

In this intermediate single-to-multiple scattering regime, the average number of scattering events is between 1 and 10. One dominant scattering order is clearly defined and the single scattering approximation is no longer valid. A spray operating in the intermediate scattering regime is referred to as being *optically dense*.

Multiple Scattering Regime

Here the number of scattering events is greater than or equal to 10. Unlike the other regimes, the relative amount of each scattering order tends to be equal, i.e. no scattering order is dominant. The diffusion approximation can be applied in this regime. A spray producing a cloud of droplets with this level of turbidity is said to be *optically thick*.

Table 3.2: *Different scattering regimes, based on the concept of optical depth.*

Single Scattering Regime	Intermediate Scattering Regime	Multiple Scattering Regime
$OD \leq 1$	$1 < OD < 10$	$OD \geq 10$
Optically Dilute	Optically Dense	Optically Thick

Remarks

It should be mentioned that other classifications can be found in the literature. A spray is often referred to as either *optically thin* or *optically dense*, implying that the OD is either above or below unity, respectively [21, 22]. Moreover, it is not uncommon to express the Beer-Lambert law on a $\log_{10}$ system, in which case the term *optical density* is used instead of optical thickness. For reasons of clarity, optical density is avoided in this thesis.

3.4   Laser Extinction

As explained above, when light traverses a turbid medium, radiation energy is lost either via scattering or absorption according to the Beer-Lambert law. Many advanced light-based diagnostic tools take advantage of this to deduce certain optical characteristics of the sample, either by measuring the transmitted or back-scattered light intensity. However, in terms of imaging, this exponential loss of light poses a problem that severely affects the accuracy and signal-to-noise ratio (S/N). In these cases, where the extinction of light is viewed as a source of error, the effect is referred to as *laser extinction*.

To explain laser extinction and its influence on the measurement accuracy, consider a sample with a spatial distribution of attenuating particles according to Fig. 3.5 a). The two peaks can be considered to represent the liquid sheet of a hollow-cone spray or, alternatively, the reaction zone of a Bunsen burner. Regardless of the actual composition, the illuminated particles are assumed to generate a signal that is linearly related to the local light intensity (e.g. elastic or inelastic scattering). As light is guided through the sample (here from the left-hand side) the local intensity at a given distance x is given by Eq. 3.3, as is quantitatively illustrated in Fig. 3.5 b). The attenuators in the first peak causes the intensity to drop to ~67% of the incident $I(0)$. The intensity continues to decrease as it propagates through the second peak. However, due to the non-linearity of the process, the absolute reduction of intensity is now less. By imaging the generated signal onto a pixel array situated at 90 degrees relative the direction of light propagation, the graph shown in Fig. 3.5 c) is obtained. Two effects can be observed; (1) the first peak appears stronger compared to the second and (2) the recorded intensity distribution is somewhat skewed (biased) towards the entrance side. The impact of these effects grow with turbidity.
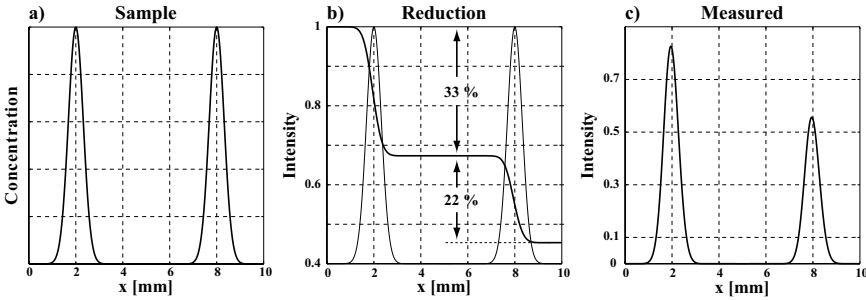
Figure 3.5: *Illustration of the effect of laser extinction.* **a):** *The spatial distribution of attenuating particles.* **b):** *The local light intensity.* **c):** *The signal generated as light interacts with the sample. Due to the exponential loss of light the acquisition does not accurately depict the true sample distribution.*

3.5   Signal Attenuation

In the previous example in Fig. 3.5 no consideration was taken to the three-dimensional nature of the sample. In reality, the signal generated at a certain point by the incident light source is also attenuated as it propagates towards the detector

via scattering and/or absorption. The effect is called *signal attenuation* or *signal trapping*. The reader should note that this particular source of error is not associated with transmission detection.

The intensity reduction caused by signal attenuation can, as for laser extinction, be expressed mathematically using the Beer-Lambert law. Combining the two effects leads to the following expression for the detected light at the position x:

$$I(x) = S \cdot I(0) \cdot \underbrace{\exp\left(-\int_0^x \mu_e dx\right)}_{\text{Laser Extinction}} \cdot \underbrace{\exp\left(-\int_{z_0}^{z_c} \mu_e dz\right)}_{\text{Signal Attenuation}} \qquad (3.16)$$

wherein S denotes the three-dimensional *source function*[2] and μ_e is the three-dimensional extinction coefficient. The light source is positioned at $z = z_0$ and the detector at $z = z_c$.

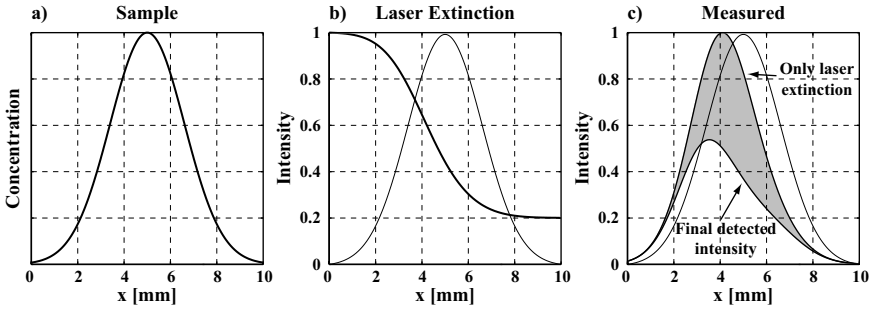

Figure 3.6: *The combined effect of laser extinction and signal attenuation. **a):** The spatial distribution of attenuating particles at $z = z_0$. **b):** The local intensity, reduced exponentially with distance due to laser extinction. **c):** Signal reduction caused by signal attenuation (grayish area). The curves are normalized with respect to the laser extinction curve.*

An example of the combined effect of laser extinction and signal attenuation is provided in Fig. 3.6. The example is constructed in the same fashion as the one in Fig. 3.5, with the exception of the sample which now extends (symmetrically) in space (not shown in the figure). The grayish area represents the loss associated with signal attenuation.

3.6 Multiple Light Scattering

Most atomizing sprays are highly scattering media, a consequence of the high number density of droplets with large scattering cross-sections (for visible light). Scattering will therefore, under most conditions, account for a large fraction of the total light extinction. However, it is important to note that although an elastic scattering event may lead to a change in photon trajectory, the photon itself is not lost and can

---

[2]The source function is a mathematical description of the magnitude of the generated signal. Under erroneous-free measurement conditions, the generated signal is a qualitative representation of S.

undergo several interaction events prior to exiting the sample. All photons belonging to scattering order 2 or above are thus *multiply scattered* (sometimes referred to as *secondary emission*).

The detection of these multiply scattered photons can severely deteriorate both the accuracy and precision of a measurement since their intensity contribution cannot be expressed mathematically using Eq. 3.3[3]. The influence of the multiply scattered light depends on the source-detector arrangement. For transmission measurements, the detection of multiply scattered light leads to an underestimation of the extinction coefficient, as seen in Eq. 3.17.

$$I(L) = I(0) \cdot e^{-\bar{\mu}_e \cdot L} + I_{MS} \qquad (3.17)$$

Here, I_{MS} is the undesired multiple light scattering intensity contribution. For side-scattering detection, a photon can undergo several alternative paths prior to its detection:

A A photon can be directly scattered, providing a faithful description of the illuminated sample.

B A photon, that originally should have been detected with a certain angle, can be given a new direction, leading to a false interpretation of the position of the scattering particle.

C A photon, that originally should not have been detected, can be given a new angle and thereby detected, also leading to a false interpretation of the position of the scattering particle.

D A photon can be multiply scattered and illuminate a droplet situated within the beam path, leading to a correct image of the droplet. However, the Beer-Lambert law assumes that the photon energy is lost in the first scattering event.

Figure 3.7 summarizes the different paths for the side-scattering detection arrangement. The false interpretation of the location of the particle (case B and C) is due to the fact that the detector assumes that all photons originate from the laser beam section.

---

[3]This does not directly imply that the information carried by multiply scattered photons is of no value. One great example of a technique that relies on multiple light scattering in order to gain volume information is Gas In Scattering Media Absorption Spectroscopy (GASMAS) [23].
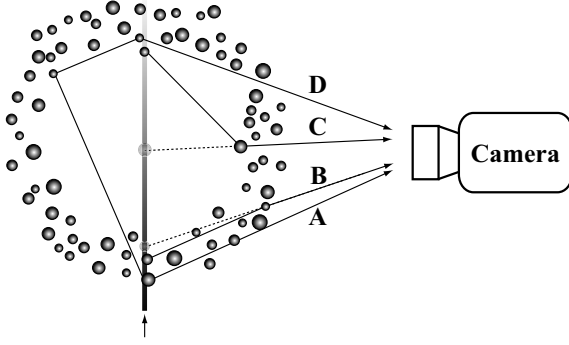
Figure 3.7: *Schematic of the various paths a photon can take prior to detection. **A**: Directly scattered light. **B-C**: False interpretations of the origin of the scattering event. **D**: Correct image of the droplet but the intensity contribution deviates from the Beer-Lambert law.*

To further complicate matters, the magnitude of the multiply scattered light intensity contribution depends on the employed detection system, where collection acceptance angle, source-detector angle as well as the distance between the detector and the laser sheet are factors that will influence the relative amount of multiply scattered light being detected [24].

Chapter 4

Laser Imaging Diagnostics

As discussed in Chapter 2, the most important parameters to measure for the complete characterization of a spray system are droplet size, velocity, number density, temperature and spatial distribution. This chapter provides an overview of the most commonly applied light-based *imaging* techniques that are capable of acquiring these parameters. Although point measurement techniques can produce 2D information by scanning the probed volume, these are not considered as imaging techniques in this context.

The chapter starts by outlining "conventional" imaging methods, briefly describing their basic principles and limitations. The final section is devoted to "advanced" techniques - X-ray absorption and Ballistic imaging.

4.1   Planar Laser Imaging

Planar laser imaging (PLI), also known as laser sheet imaging, is an attractive technique since it produces optically sectioned images, that is, the signal can be interpreted as though originating from a thin two-dimensional section only. Figure 4.1 illustrates the basic principle of the approach. A negative cylindrical lens first expands the incident beam in one direction. The beam is then collimated using a positive spherical lens which also compresses the light in the other direction, thus creating a sheet of light. In certain applications, a diverging laser sheet is preferred which can be achieved by replacing the spherical lens with a cylindrical. Regardless of which, the light is then guided through the sample at a certain position and the signal which is generated as the photons interact with the sample is detected, generally with a CCD camera positioned at 90 degrees. Depending on the optics involved, the lateral spatial resolution of the recorded image can be made as good as $\sim 10~\mu$m and the axial spatial resolution $\sim 100~\mu$m.

Laser sheet imaging is the basis for a variety of qualitative and quantitative imaging techniques but the most straightforward implementation of PLI for spray studies is planar Mie imaging, which can be employed for nearly all types of atomizing spray systems with, in principle, any type of light source. The principle of this approach is to detect the light which is elastically scattered on the droplets. The method is commonly applied to gather information which is related to the structure of the spray,
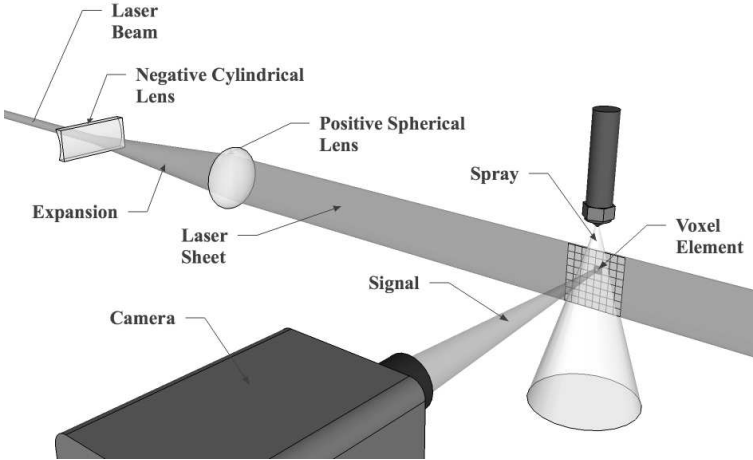
Figure 4.1: *Optical arrangement for a laser sheet measurement.*

e.g. cone angle and liquid penetration length. For spherical droplets with a diameter D, the intensity of the scattered light can be assumed to be proportional to D^2 [25]. Thus, when probing an atomizing spray system, the light contribution from the smaller or evaporated droplets becomes negligible. Planar Mie scattering can thus be used to visualize the liquid phase of a two-phase flow [26].

Another common planar laser imaging approach for spray research is Planar Laser Induced Fluorescence (PLIF), which, unlike planar Mie scattering, can be made species-specific. This feature has made the technique especially attractive for combustion research, where it can be used to map naturally present species, in turn allowing e.g. the flame front to be visualized [27]. In spray research the injected fuel is often doped with a so-called tracer, despite the fact that most commercial fuels contain compounds that naturally fluoresce when excited by ultra-violet radiation. The reason for adding tracers is because of uncertainties regarding which parts of the composition that naturally fluoresce, which renders difficulties when attempting to quantify the signal. The tracer and its concentration must be chosen carefully and it should, in principle, have the same characteristics as the fuel. Moreover, most tracers exhibit pressure and temperature dependencies that should be taken into account, especially when quantitative data is desired [28].

4.2 Velocimetry

4.2.1 Particle Image Velocimetry

Particle Image Velocimetry (PIV) is a laser sheet-based imaging technique, capable of extracting a two-dimensional velocity field, comprising either two or three velocity components. The basic principle of the technique is to perform two laser sheet measurements (see Fig. 4.2), separated Δt in time, and to determine the displacement $\Delta \bar{x}$ of the flow elements during this (short) time interval. The velocity can

then be obtained by calculating

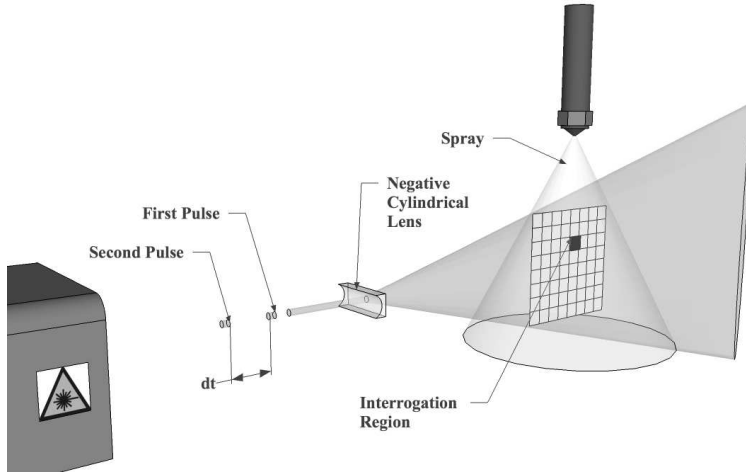$$\bar{v} = \frac{\Delta \bar{x}}{\Delta t} \tag{4.1}$$

Figure 4.2: *Illustration of the optical arrangement utilized for PIV and PTV.*

One approach to measure the displacement vector is to track particles (tracers) naturally present in the flow. This is known as Particle Tracking Velocimetry (PTV). The method can, however, not be readily applied in measurement situations with a high number density of particles [26]. PIV, on the other hand, does not track naturally present tracers. To visualize the velocity field the fluid is instead seeded with particles. The particle size (typically in the range 1-100 μm) is an important factor; too large particles may not give an accurate representation of the flow while too small particles may not scatter the light sufficiently. To extract velocity vectors in 2D, the tracer distribution is visualized by guiding a laser sheet through the investigation region. To freeze the motion in time, a pulsed laser is required, where a frequency doubled dual cavity Nd:YAG laser is normally employed. The scattered light is then detected at 90 degrees with a CCD camera. After a suitable time, Δt, which is determined by the characteristics of the flow, a second laser pulse is fired. The displacements occurring during Δt, which is a reflection of the flow field, can then be extracted from these two frames. The input of this information in Eq. 4.1 finally provides the desired velocities.

The data analysis associated with PIV is illustrated in Fig. 4.3. First, each frame is divided into several so-called *interrogation regions*. The size of these regions, which will set the spatial resolution of the resulting velocity field, depends on the density of tracers and is usually adjusted so that it contains 10-25 particles [11]. By cross-correlating each interrogation region in frame 1 with its neighboring ones in frame 2 on a pixel-to-pixel basis, the displacement of the group of particles can be measured.

Standard PIV systems provide only the x and y velocity components. To determine the velocity field in all three dimensions, an approach called stereoscopic PIV can be utilized. In this optical arrangement, two cameras, with different viewing angles, are used simultaneously to visualize the tracer distribution. Because of the
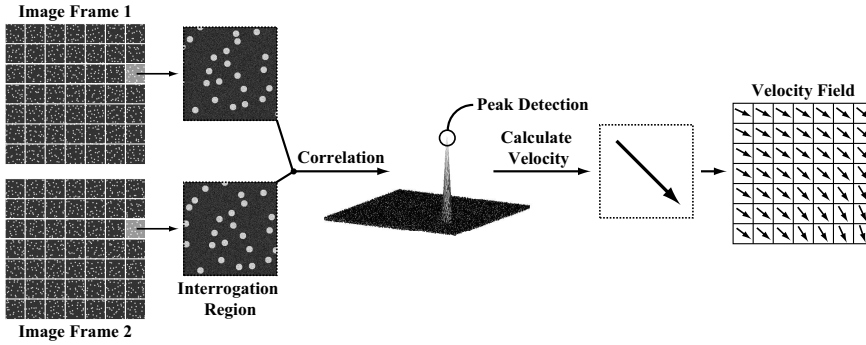
Figure 4.3: *Data evaluation routine for PIV. Inspired by [11].*

parallax effect, the approach allows displacements taking place in the z-direction to be quantified as well. However, to capture these motions, the laser sheet must be made thicker compared to a standard PIV measurement. A detailed description of the history of particle tracking can be found in [29]. It could be mentioned that recent developments of the PIV technique now also enables 3D velocimetry by means of so-called volumetric PIV [30].

Applications to Optically Dense Sprays

In spray research, direct measurements of the liquid motion using PIV is restricted to optically dilute regions. When applied in denser regions, the large number of droplets fill the interrogation region, making the reliability of the technique questionable. Multiple light scattering, signal attenuation and laser extinction are additional effects which hamper the performance of PIV when applied to optically dense media. However, PIV can be used to gain indirect information regarding the spray formation region. For example, the technique can capture the velocity field of the surrounding gas, which carries information regarding air entrainment. The approach furthermore allows recirculation zones to be characterized [31].

4.2.2 Molecular Tagging Velocimetry

Molecular Tagging Velocimetry (MTV) can be thought of as the *molecular* counterpart of PIV, acting as a complementing technique to measurement situations where the use of seeders, for various reason, are undesired. The basic principle of the method consist in "writing" a recognizable structure into the sample. With time, flow motions will distort the initial structure. Measuring and quantifying this distortion after a given time, Δt, in a fashion similar to PIV, yields the desired velocity field.

Experimentally, the "writing"-process consists of exciting a tracer to a long-lived state, typically by means of a pulsed laser (called the "write" or "tag" beam). Depending on the application and the time scales associated with the flow of interest, different molecular complexes can be utilized. Examples of tracers used for MTV measurements of gas-phase flows are ozone, OH, acetone or biacetyl, to name a few [32]. Basically, a molecular complex is suitable for MTV if its lifetime is long in relation to the flow convection time scale. For instance, the excitation of biacetyl leads

to both fluorescence and phosphorescence, the former being too short-lived ($\sim$10 ns) for MTV applications. The latter process, on the other hand, has a lifetime of up to 1.5 ms (in oxygen purged environments) and is therefore sufficiently long to be utilized for velocimetry in most spray applications. To measure the velocity field, a second "read" beam is fired after Δt, having its wavelength tuned appropriately to stimulate emission from the long-lived excited molecules.

Molecular Tagging Velocimetry can be performed in a variety of ways and is applicable for both liquid and gas phase applications [32, 33]. Perhaps the most straight-forward approach of MTV is by using single or multiple line excitation [34]. Such an approach will, however, only provide one component of the velocity, that which is normal to the tagged line. To enable measurements of two components, the write beam must have spatial gradients in two, preferably orthogonal, directions. This can be achieved by using two crossing laser beams, yet the more attractive experimental arrangement consists of illuminating the sample with a grid of intersecting laser lines as this approach provides 2D data.
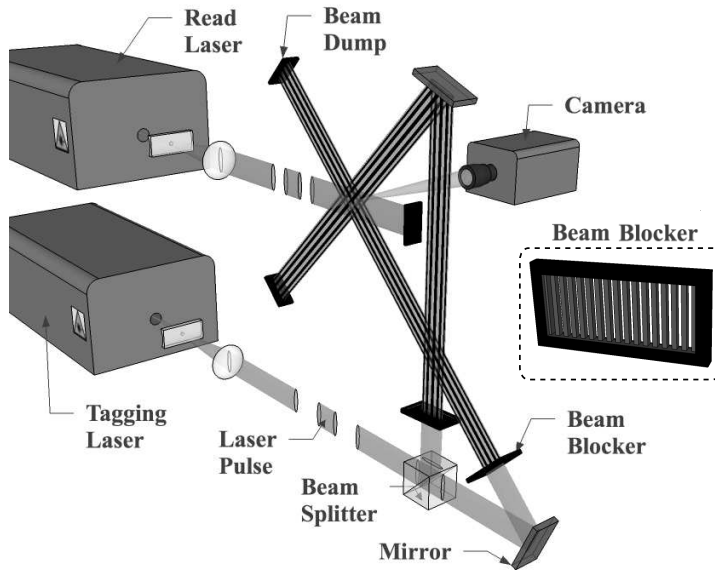

Figure 4.4: *Optical arrangement for multi-point MTV.*

A schematic of the optical arrangement for the multi-point scheme is given in Fig. 4.4. The write beam is first divided using a 50:50 beam-splitter. To generate the desired grid pattern the resulting beams are then guided through a beam blocker, consisting of e.g. an aluminum plate with a series of thin slots [35]. The structured beams are then directed towards the region of interest. Depending on the optics involved, up to $\sim$700 intersecting points (velocity points) can be achieved, mostly limited by the pixel density of the detector. Immediately after the write laser is fired, the camera records an initial image of the tagged flow using the read laser. If Δt is relatively long in relation to the readout time, a single camera setup is sufficient,

otherwise two detectors are required. Figure 4.5 illustrates how a 2D grid structure becomes distorted during the time interval between acquisitions.
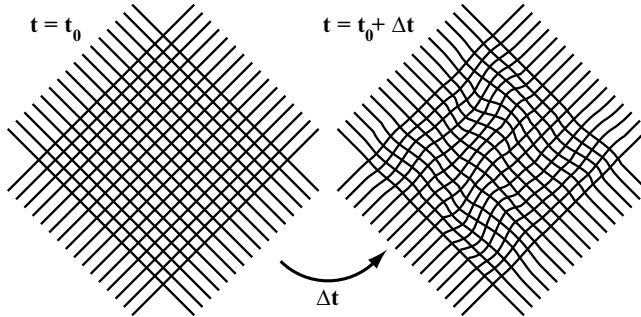

Figure 4.5: *Examples of a reference image, acquired at t_0, and the second read image, measured at $t_0 + \Delta t$.*

The selection of the time delay between the two acquisitions is dictated by several factors. A large Δt leads to larger displacements which, in turn, yields a higher dynamic range of the velocity measurement. However, with time, the population in the excited state naturally depletes and an increase in the delay often leads to a degradation of the signal-to-noise ratio (S/N) in the second (delayed) image. The correct choice of Δt, as well as the density of grid lines, thus depends on the tracer molecule in combination with the convection time scales associated with the probed flow.

Applications to Optically Dense Sprays

MTV has shown great potential for visualizing the velocity field in optically dense environments. Compared to PIV and PTV, the technique is less sensitive to multiple light scattering, due to the use of relatively wide tag beams which are still recognizable despite being blurred. Krüger and Grünefeld used the technique to study the air entrainment in a hollow-cone spray generated by a GDI injector [36]. Here NO was used as a molecular tracer, created by photodissociating tert-butyl nitrite which was seeded into a co-flow. The same author later presented velocity and acceleration measurements on the liquid flow by means of MTV [37].

4.3 Droplet Sizing

4.3.1 Laser Sheet Dropsizing

When light interacts with a spherical droplet, the elastically scattered intensity is essentially related to the surface area (D^2) whereas the fluorescence signal is volume-dependent (D^3). Therefore, the ratio between a PLIF and a planar Mie scattering image would thus render a two-dimensional mapping of a quantity that is related to D. This approach for droplet sizing is known as Laser Sheet Dropsizing (LSD) [25, 38]. The name Planar Droplet Sizing (PDS) can also be found in the literature [39, 40].

To explain in more detail, consider a volume element containing an ensemble of N fluorescing droplets with a certain size distribution. The LIF signal detected from this element is given by

$$S_{LIF} = C_{LIF} \cdot \sum_{i=1}^{N} D_i^3 \tag{4.2}$$

where C_{LIF} is a measurement constant that depends on factors such as collection optics, index of refraction, scattering angle, *etc.* The corresponding elastically scattered signal can be expressed according to

$$S_{Mie} = C_{Mie} \cdot \sum_{i=1}^{N} D_i^2 \tag{4.3}$$

If these signals are measured simultaneously, i.e. on the same ensemble of droplets, the ratio of these signals (Eq. 4.4) is proportional to the *Sauter Mean Diameter* (SMD), often denoted D_{32}.

$$\frac{S_{LIF}}{S_{Mie}} = K \cdot \frac{\sum_{i=1}^{N} D_i^3}{\sum_{i=1}^{N} D_i^2} = K \cdot \text{SMD} \tag{4.4}$$

The value of K in Eq. 4.4 is usually determined from a calibration measurement using a second sizing approach, e.g. Phase Doppler Anemometry (PDA).

An example of a typical experimental arrangement for the LSD technique is illustrated in Fig. 4.6. A laser sheet with the appropriate wavelength to excite molecules in the liquid irradiates the spray at a given position. Each voxel generates a signal consisting of both elastically and inelastically scattered light. The spectrally separated intensities are divided by means of a dichroic mirror and detected using CCD cameras. This arrangement allows instantaneous realizations of the SMD distribution. Optionally, the two signals can be recorded using a single camera, either by employing a stereoscope (providing instantaneous images but with reduced spatial resolution) or by collecting the two signals separately in time, thus restricting the technique to averaged imaging.

It is important to note that the SMD does not represent the average droplet diameter but is biased towards larger diameters due to the volume-dependence of the LIF signal. This is illustrated in Fig. 4.7 where three different droplet distributions, but with an equal average diameter, are shown. A suitable distribution must be assumed to assess truly quantitative data, where once again a second sizing technique can be used for this purpose. However, there is no guarantee that the distribution obtained at a single point within the spray (from e.g. PDA) remains valid throughout the entire sample.

Another uncertainty with LSD is related to the volume- and area-dependence of the inelastically and elastically scattered light, respectively. With a too high dye concentration, the volume of the droplet is not equally illuminated due to absorption, and consequently the D^3 dependence in Eq. 4.2 is no longer valid [25]. The D^2 relation in Eq. 4.3 is questionable (especially for small droplets) due to the appearance of signal oscillations (see Chapter 3.2.1). The magnitude of these oscillations are especially pronounced when the scattered light is collected at 90 degrees, which is,
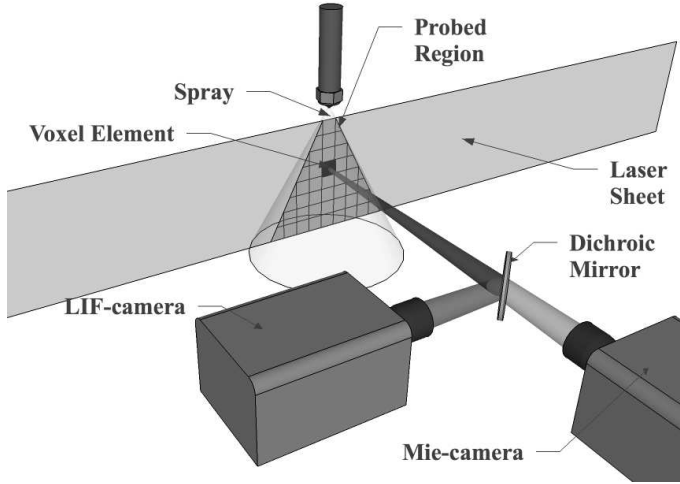
Figure 4.6: *Arrangement for instantaneous visualization of the SMD distribution.*

unfortunately, the most convenient way experimentally. However, Charalampous and Hardalupas recently demonstrated that shifting the viewing angle to 60 degrees significantly reduces the presence of these signal oscillations, leading to an increased accuracy of the LSD technique for a broad range of refractive indices [41].
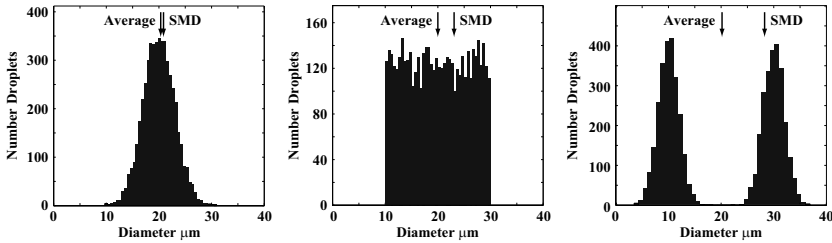

Figure 4.7: *Three droplet size distributions, illustrating the difference between the geometrical average droplet diameter and the SMD.*

Applications to Optically Dense Sprays

The LSD technique enables quantitative, optically sectioned, 2D readings of the droplet size distribution. Furthermore, instantaneous images can be recorded by using either two cameras or by implementing a stereoscope, making the technique attractive for the study of transient and turbulent flows. Unlike other sizing approaches, the method is said to be applicable to optically dense sprays, however, at present this statement lacks convincing experimental validation. The main argument supporting this claim is that the two collected signals are ratioed, thereby canceling out the contribution from multiply scattered light. However, it should be pointed out that the multiply scattered light superimposed on the fluorescence and on the Mie scattering signal are not equal and therefore not suppressed using this approach [17]. Although,

the ratio approach has the benefit of canceling out intensity variations in the laser sheet profile.

Even though the technique is both experimentally simple and mathematically elegant, the method requires further development before it can be applied for droplet sizing within dense sprays, with special concern regarding uncertainties related to multiple light scattering.

4.3.2 Interferometric Laser Imaging

The Interferometric Laser Imaging for Droplet Sizing (ILIDS) technique is a 2D sizing method applicable for low number density sprays. The method utilizes laser sheet illumination to access 2D information but in contrast to planar laser imaging, ILIDS is based on depicting out-of-focus light. To elaborate, consider a ray of light incident on a spherical transparent droplet. The radiation will be partially reflected on the surface and partially refracted, see Fig. 4.8. When the refracted light meets the surface, a part of its intensity is refracted and scatters to the outside, whereas the remaining part is reflected back into the droplet. The process is then repeated and each refracted ray leaving the droplet is classified by its *order of refraction p* ($p = 0, 1, 2, ...$) [41].

External Reflection
p = 0

Incident Ray

Refraction
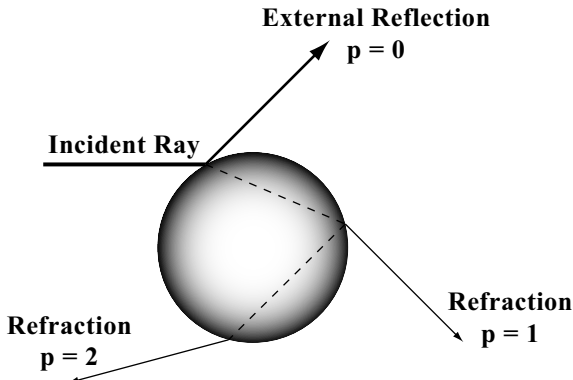**p = 2**

Refraction
p = 1

Figure 4.8: *A ray of light being reflected and refracted as it encounters a transparent droplet.*

The reflected and the first-order refracted light are dominant in the wide-angle forward scattering region (around $\theta = 30°$ to $80°$) and their intensity ratio is near unity at $\theta \approx 70°$ [42, 43]. A photograph taken within this observation angle ($30°$ to $80°$) of an illuminated droplet will consist of two distinct spots. These spots of light are named *glare points* and arise from the light contribution of either the reflected ($p = 0$) or the refracted light ($p = 1$), respectively [44]. The separation between the glare points depends on the relative refractive index m of the illuminated particle, the observational angle θ and the size of the droplet [45]. Knowing the first two quantities provides the opportunity for droplet sizing, as demonstrated by Chang [46]. However, this approach demands high spatial resolution and small droplets are therefore not readily measured.

If the incident radiation is coherent, the light originating from the two glare points will interfere and generate a sinusoidal fringe pattern as they overlap in the far-field. Similar to the information carried by the glare points, the spatial frequency of these

stripes are directly related to the droplet diameter through the wavelength of light, relative refractive index and the observational angle. The size of the droplet can be deduced in two ways; (1) by determining the spatial frequency of the interference pattern (by means of e.g. Fourier analysis) or (2) by simply counting the number of fringes [45]. Equation 4.5 describes the relationship between the diameter D and the number of fringes N [43].

$$D = \frac{2\lambda N}{\alpha} \cdot \left(\cos(\theta/2) + \frac{m\sin(\theta/2)}{\sqrt{m^2 - 2m\cos(\theta/2) + 1}} \right)^{-1} \qquad (4.5)$$

where λ denotes the wavelength of the incident light and α and θ are the collecting and off-axis angles, respectively. Note that the number of fringes are affected neither by the magnification of the collection optics nor the intensity of the incident light. Moreover, the number of fringes from a given droplet can be adjusted by varying the aperture (α). This is a very important feature since the number of countable fringes is limited by the finite resolution of the detection system. However, to accurately determine droplet diameters the index of refraction m must be known. This poses a problem when studying reacting sprays, since m can vary as the fuel undergoes evaporation.

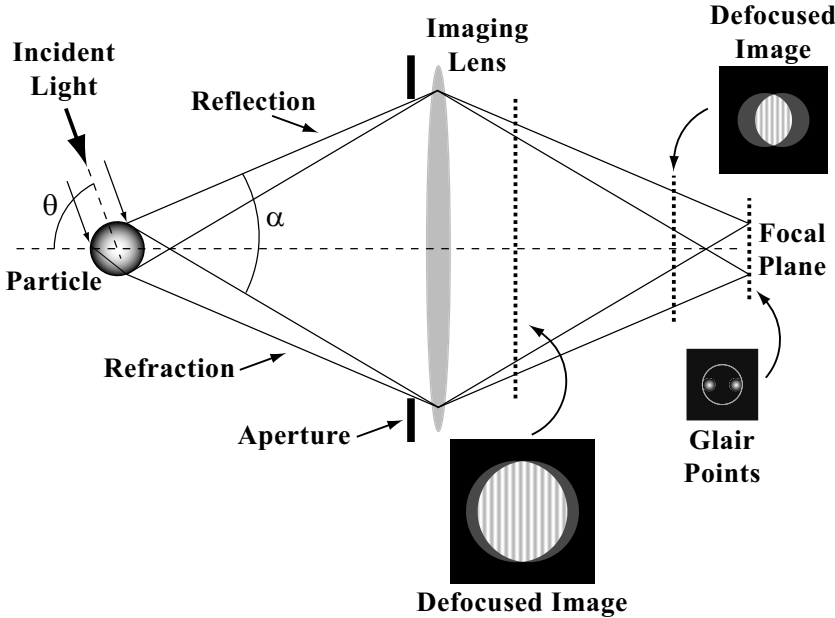**Figure 4.9:** *Basic optical configuration for the ILIDS technique. Adapted from [45].*

As illustrated in Fig. 4.9, the size of the defocused image of each pair of glare points is only dependent on the degree of defocusing. Hence, differently sized droplets appear equally large as long as they are situated of equal distances from the imaging lens. Due to the finite thickness of the laser sheet, this will not always be the case and

the size of an individual droplet (in the recorded image) actually contains information regarding its position along the plane perpendicular to the image plane.

Perhaps the greatest limitation with the ILIDS technique concerns spatial overlapping between the different interferograms. Glover *et al.* presented a computational methodology to remedy this issue, yet despite these efforts, the conventional ILIDS technique is still limited to number densities of roughly 10^3 cm^{-1} [47]. In 2000, Maeda *et al.* presented an elegant experimental solution to the problem that extended this limit by a factor of $\sim 10^3$ [43]. By positioning a pair of cylindrical lenses along the detection path, the signal becomes optically compressed prior to detection. This reduces the size of the interference patterns which, in turn, lowers the risk for spatial overlapping without distorting the desired frequency information. Another benefit with this approach is that the integration of the signal leads to an amplification that improves the S/N.

Figure 4.10 illustrates the difference between conventional and advanced ILIDS. In this computer simulated example, the imaged area contains the interference signal from 150 randomly distributed particles. Without the implementation of image compression, almost no isolated droplets can be localized.
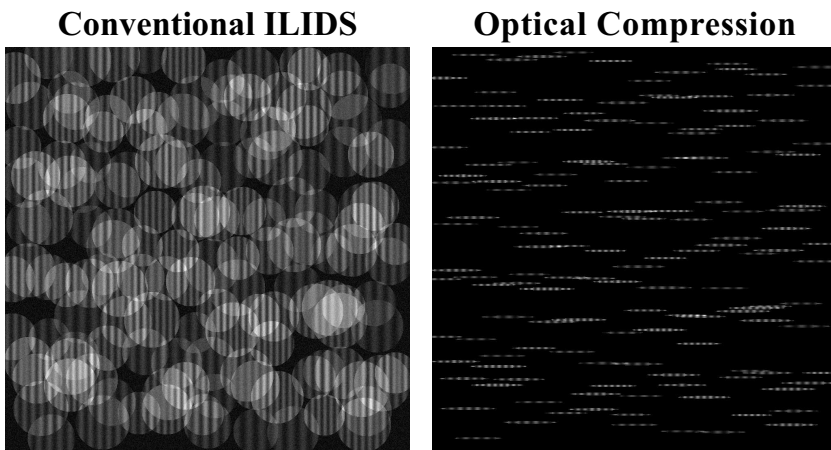
Conventional ILIDS   Optical Compression

Figure 4.10: *Comparison between ILIDS with and without optical compression. The imaged area contains 150 randomly distributed particles.*

4.4 Thermometry

4.4.1 Laser Induced Phosphorescence

One of few methods to visualize the temperature distribution within an atomizing spray is by means of Laser Induced Phosphorescence (LIP). This technique is based on exciting certain materials - phosphors - whose subsequent emission of radiation - phosphorescence - has an inherent temperature dependence. The photophysics of phosphorescence is similar to that of fluorescence but differs in that the transition from the excited state is quantum mechanically forbidden (singlet-to-triplet transition). The molecule may still relax to its ground state by emitting radiation, but

does so at a much lower rate. The lifetime[1] of the phosphorescence signal therefore becomes considerably longer (microseconds to milliseconds) compared to fluorescence (nanosecond scale) [48].

Phosphors show, in general, a strong temperature dependency both in the temporal decay (lifetime) of the emitted signal as well as in the emission spectra, characteristics which can be exploited for thermometry. The lifetime method consists in exciting the phosphors using a short laser pulse after which the phosphorescence signal is recorded using a photo-multiplier tube (PMT). The emitted light intensity decays exponentially in accordance with

$$I = I_0 \cdot \exp(-t/\tau) \tag{4.6}$$

where I_0 is the initial emission intensity, t is time and τ is the lifetime constant, which decreases with increasing temperature. The value of τ is then evaluated by fitting an exponential curve to the acquired data and comparing the result with a calibration curve. Although commonly applied for point measurements, this approach can also provide 2D temperature readings. This was demonstrated by Omrane *et al.*, who applied planar LIP on an atomizing spray [49]. To temporally resolve the intensity decay the authors employed a camera equipped with seven individual intensified CCDs, each designated to record the luminosity at different times after excitation. From these seven frames the lifetime could be evaluated on a pixel level.

The spectral method is generally considered better suited for 2D imaging. This approach relies on the fact that some energy transitions respond differently with temperature. Experimentally the procedure comprises illuminating the phosphor-seeded sample with a laser sheet and detecting the phosphorescence through two (appropriately chosen) spectral filters. The ratio between the acquired images are then extracted and the obtained values are compared with a calibration database. Thus, unlike the lifetime method that can suffer from particle movement, the spectral approach provides instantaneous temperature readings and is, from this aspect, more suitable for high-pressure spray applications [50].

4.5 Limitations With Planar Laser Imaging Techniques

4.5.1 Laser Extinction and Signal Attenuation

Due to its simplicity, relatively low cost and flexibility, planar laser imaging is one of the most commonly used imaging techniques, especially for spray and combustion research. However, the method is not limited to macroscopic imaging and can be applied in microscopy as well [51, 52]. The technique can be made species-specific and is capable of visualizing a single plane of the probed sample with both high temporal and spatial resolution.

Laser sheet imaging and most of the techniques based on it does, however, suffer from a number of uncertainties and errors when applied to optically dense media. First, the laser sheet intensity reduces exponentially as it propagates through the sample due to scattering and/or absorption. This effect, which can be expressed mathematically by Eq. 3.3, has been described in Chapter 3.4 and is referred to as

---

[1]Time taken for the intensity to decrease to $1/e$.

laser extinction. The consequence of laser extinction is a skewed image, as the droplets located at the entrance side are illuminated more intensely, compared to those situated near the exit. Even though the effect cannot be avoided, it is possible to compensate for the skewness. Abu-Gharbieh *et al.* developed an algorithm that compensates for the exponential loss of light [22]. The approach does, however, require the spray to be symmetric around its central axis, therefore limiting its applicability. Hertz and Aldén addressed the problem by measuring the fluorescence and the transmitted light intensity simultaneously and used an iterative approach to compensate for the intensity reduction [53]. The effect of laser extinction can be mitigated experimentally by illuminating the sample with counter-propagating laser sheets [54, 55].

The second source of error concerns the exponential loss of the signal that is generated by the laser sheet, i.e. signal attenuation (see Chapter 3.5). As for laser extinction, signal attenuation cannot be avoided and is, in addition, not readily compensated for since it depends on the distribution of attenuators situated in the volume between the laser sheet and the detector. For this reason, very few experimental solutions to the problem (for laser sheet imaging) can be found in the literature. Versluis *et al.* circumvented the problem elegantly by implementing bidirectional illumination [54] (note that this is the same method as presented in [55]). By taking advantage of the fact that both laser sheets are equally affected by laser extinction and signal attenuation, the absolute number density could be extracted by calculating the derivative of the logarithm of the intensity ratio. Kalt *et al.* suggested that the use of a large camera objective could homogenize the effect of signal attenuation [56]. Although this approach may provide satisfactory results when probing media where absorption is mainly responsible for signal attenuation, it is not recommended when optically dense or thick sprays are probed as the method lowers the singly to multiply scattered light ratio [24].

The complexity of laser extinction and signal attenuation is exemplified quantitatively in Fig. 4.11, illustrated by a laser sheet measurement performed on a GDI spray. The true distribution of attenuating particles are shown in Fig. 4.11 a)[2] and represents a measurement that is unaffected by laser extinction and signal attenuation. As the light propagates through the sample (from the left), the intensity gradually decreases as seen in Fig. 4.11 b), where the local intensity of the laser sheet is shown.

By knowing the incident and the transmitted light intensity, the spatially resolved optical depth can be extracted along the laser sheet profile, Fig. 4.11 c). In this example OD reaches a maximum of ∼1.5 (excluding the region attenuated by the nozzle) which is near the border between the single- and intermediate scattering regimes. Hence, the effects illustrated in this example are not as severe as those commonly encountered when probing optically dense atomizing spray systems.

Multiplying the local intensity of the laser sheet with the true distribution results in the image presented in d), thus corresponding to the a laser sheet measurement only affected by laser extinction. Notice how the detected intensity on the right-hand side of the probed sample is considerably lower than that on the left-hand side.

---

[2]What is actually shown in a) is the distribution of the extinction coefficient (the indicated values are, however, incorrect). As explained in Chapter 3.1, this is composed of the product between number density and extinction cross section but serves well in this example as a representation of the sample.
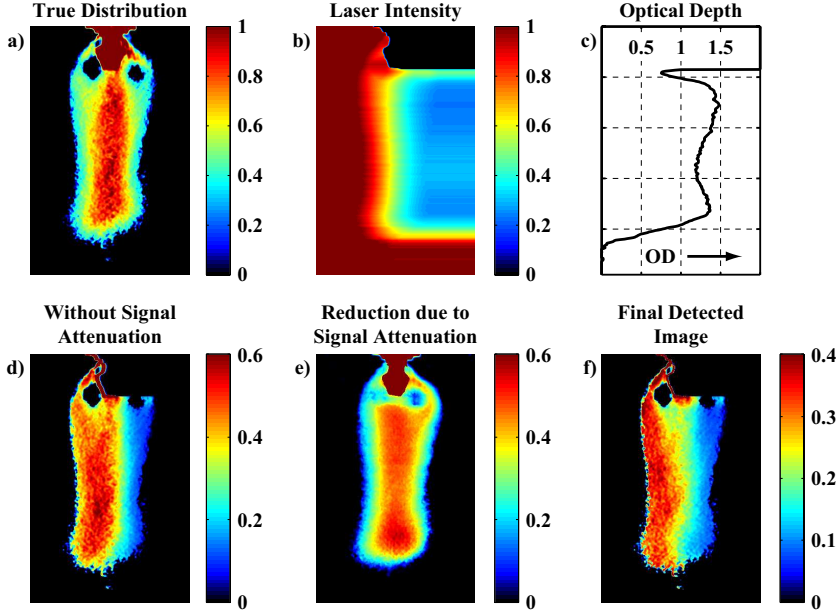
Figure 4.11: *Illustration showing the errors induced by laser extinction and signal attenuation. **a**): The true distribution of attenuating particles. **b**): The reduction of light intensity as the laser sheet propagates through the scattering sample. **c**): The optical depth along the laser sheet profile. **d**): Image recorded without the effect of signal attenuation. **e**): Local dampening by the attenuators situated in between the laser sheet section and the detector. **f**): Final image, where the intensity levels are affected by both laser extinction and signal attenuation.*

Signal attenuation can be simulated by integrating the extinction from laser sheet section to the camera. This is shown in Fig. 4.11 e), where the indicated values represent the local dampening factors (assuming detection at 90 degrees only). The smoother variations in image details noticeable here are due to the volume integration, which acts as an low-pass filter. Finally, the light that is actually detected is given in Fig. 4.11 f), where the intensity values in d) are divided with e). Notice the clear differences between a) and f), where the spatial distribution of attenuators in the latter case appears skewed towards the left-hand side.

4.5.2   Multiple Light Scattering

In the previous example no consideration was made for multiple light scattering issues. As explained in Chapter 3.6, this phenomenon leads to erroneous signal levels and misinterpretations. A not uncommon misconception is that this undesired light contribution can be removed by applying an intensity threshold on the recorded image.

To illustrate the influence of multiple light scattering experimentally requires some *a priori* knowledge concerning the sample characteristics. Figure 4.12 is an example of such a sample. Here a laser sheet is guided through a homogeneous scattering medium (a cuvette containing a mixture of water and milk). A rod is inserted between the

laser sheet and the window facing the camera, with the purpose of blocking a part of the scattered light. To ensure sample homogeneity the solution is continuously stirred using a magnetic stirrer. Both the inserted rod and the homogeneity of the sample provides sufficient knowledge to make assessments regarding intensity errors in the recorded image.
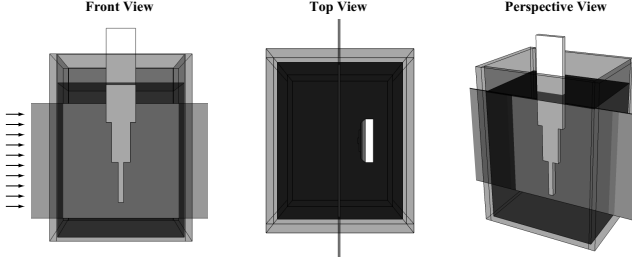

Figure 4.12: *To illustrate errors induced by multiple light scattering a homogeneous sample is probed using laser sheet imaging. The purpose of the rod is to block a part of the scattered light.*

The resulting laser sheet image of the homogeneous sample together with a vertical and horizontal summation (normalized to unity) is shown in Fig. 4.13. Despite the presence of the rod, photons appear to be originating from this region (compare with illustration in Fig. 3.7, case B and C). In addition, parts of the sample left un-illuminated also give rise to non-negligible signal levels and a broadening of the laser sheet can be observed. Furthermore, according to the Beer-Lambert law, the intensity should decay (single) exponentially with distance due to the homogeneity of the sample. This is not observed. On the contrary, the intensity appears to increase with distance (light enters from the left). This counterintuitive effect may, however, be partly attributed to the glass confinement. With support of these observations it is possible to state that a single intensity threshold would not suffice in order to remove the contribution arising from multiply scattered photons.
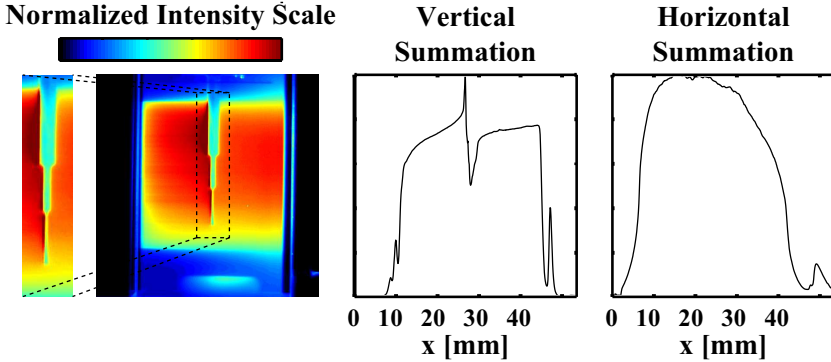

Figure 4.13: *Planar laser imaging applied on a homogeneous scattering media (OD $\approx$ 2). Despite the presence of the rod light appears to be originating from this "zero region".*

Multiple Light Scattering Suppression

Apart from X-ray absorption and Ballistic imaging (BI) which will be discussed shortly, a few techniques addressing the multiple light scattering issue can be found in

the literature. Brown *et al.* demonstrated a passive approach to avoid the detection of this undesired light. The approach is based on scanning the spray using a single beam of light, rather than illuminating it with a laser sheet. The authors argued that by minimizing the total light power that interacts with the spray would, in turn, minimize the opportunity for multiple light scattering [57]. A similar approach was presented by Pastor *et al.*, who also illuminated a light scattering sample with a beam of light. In this article, the authors used the scattered light intensity surrounding the laser beam to estimate (and thus correct for) the amount of multiply scattered light present along the beam [58]. Smallwood *et al.* used an image post-processing routine to diminish diffuse light [59]. Here the authors argued that since multiply scattered light primarily originates from out-of-focus regions, its intensity contribution should end up as low spatial frequency information in the resultant image. Low-pass filtering this image would thus provide a 2D map of this unwanted contribution which, in turn, could be used to correct the raw data image. This approach may, however, also reduce the appearance of any naturally occurring low spatial frequency information.

4.6   Advanced Diagnostics

This section is devoted to a brief description of the two most up-to-date advanced and promising techniques, both enable and are designed for measurements of the spray formation region.

4.6.1   X-ray Absorption

Quantitative investigations in the spray formation region are not readily performed using visible light mainly due to; (1) multiple interactions between droplets and the incident radiation and (2) the presence of non-spherical liquid ligaments[3]. To circumvent these issues and to gain knowledge about spray phenomena in this optically dense (or thick) region can be achieved by using a X-ray source instead of visible light.

Scattering of electromagnetic radiation is classified as either diffraction, refraction or reflection. With the wavelength of X-rays being several orders of magnitude smaller than typical droplets generated by high-pressure injection systems, the dimensionless size diameter x (Eq. 3.12) becomes extremely large. In such a case, diffraction renders no change in photon trajectory and is thus indistinguishable from undiffracted light. Reflection and refraction on the other hand occurs when the light encounters a change in refractive index m, i.e. in the interface between the air and the liquid. Thus, if the relative refractive index equals unity, neither refraction nor reflection occurs, making the droplet "invisible" (in terms of scattering). Under these conditions the X-rays are attenuated only by absorption, according to the Beer-Lambert law [18]:

$$I(L) = I(0) \cdot \exp\left(-\mu_a \cdot L\right)$$

Here, $I(0)$ is the incident light intensity, $I(L)$ is the transmitted light through a liquid bulk of thickness L and μ_a is the absorption coefficient. If μ_a is known, either through

---

[3]Most quantitative laser diagnostic techniques assume (or require) the probed droplets to be spherical, as this enables the comparison with the Mie theory.

calculations or a calibration measurement, the so-called *equivalent liquid length L* can be extracted according to

$$L = -\ln\left(\frac{I(L)}{I(0)}\right)/\mu_a \qquad (4.7)$$

The equivalent liquid length is thus a measure of the amount of liquid fuel in the beam path (absorption in the evaporated liquid is assumed to be negligible), as illustrated in Fig. 4.14. Note that the use of monochromatic X-rays is essential to accurately determine μ_a.
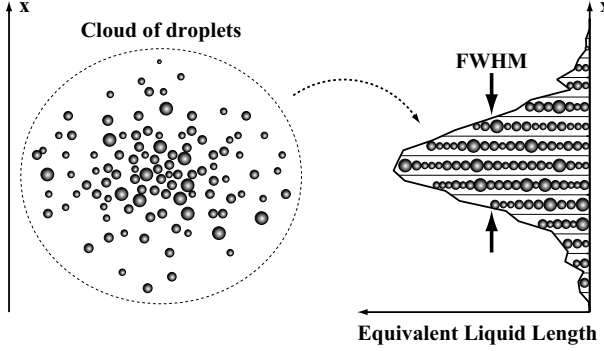

Figure 4.14: *The concept of equivalent liquid length. The curve shows the path-integrated liquid length.*

By measuring the radial distribution of L (Fig. 4.14) and assuming the liquid mass distribution to be circularly symmetric the local liquid/gas ratio - *liquid volume fraction* - can be determined. This was first demonstrated by Gomi and Hasegawa on a water jet surrounded by a flow of nitrogen in 1984 [18]. More recently, Powell *et al.* implemented the method for time-resolved measurements of the local liquid volume fraction of a transient diesel spray [60]. In this rigorous experiment, averaged absorption measurements were conducted at 900 different axial and radial positions at each operating condition. The beam size was approximately 0.5 × 0.3 mm and the system had a time-resolution below 1 μs. Apart from allowing the liquid volume fraction to be determined, this experimental setup, which is schematically illustrated in Fig. 4.15, could be used to measure the velocity of the leading and trailing edge of the spray. The most striking results reported in this publication concerns the measurement performed near the orifice of the injector. At 1 mm from the nozzle tip, a maximum liquid volume fraction of 75% was reported, which would indicate the absence of an intact liquid core.

The advantages of the X-ray absorption technique is that it is quantitative, non-intrusive, time-resolved and not significantly affected by scattering (multiple light scattering is thus negligible). Although, perhaps its primary advantage is that it can be applied in the spray formation region where almost all alternative quantitative optical diagnostics are hampered by the high number density of droplets and the presence of non-spherical droplets. However, the method is complicated and expensive, as it requires a synchrotron facility. Furthermore, it provides only point-wise path-integrated data and the evaluation of liquid volume fraction relies on the spray being symmetrical. To reduce statistical uncertainties, the measurements are usually ensemble averaged, thereby losing information regarding shot-to-shot variations. Fi-
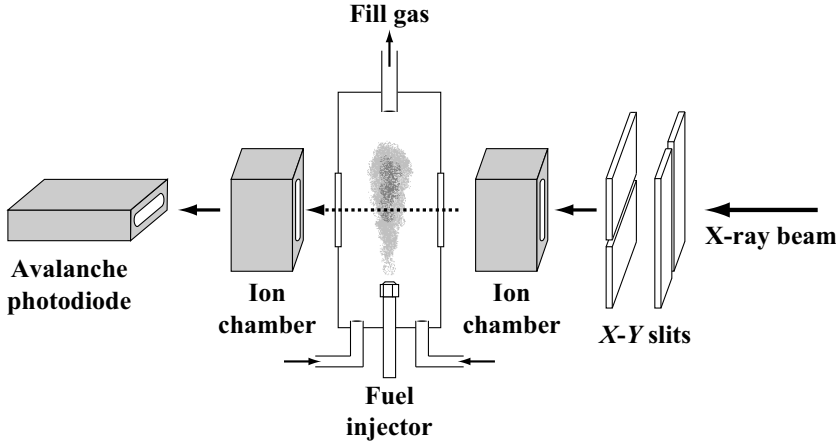
Figure 4.15: *Experimental arrangement for X-ray absorption. Adapted from [60]*

nally, X-rays are not readily manipulated and far more hazardous compared to visible light.

4.6.2 Ballistic Imaging

Ballistic imaging is a line-of-sight shadowgraphy imaging technique, primarily developed for medical applications. The method requires laser sources with short pulse durations, fast gating systems and two-dimensional array cameras. For these reasons the development of ballistic imaging was made possible first during the 1990's.

The overall aim of BI is to reject noise carrying light and to produce a high-resolution shadowgraphic images of turbid objects. The most ideal photons for this task are the ballistic ones (see Chapter 3.3.1), hence the name of the technique. As described previously, this group of photons traverse the turbid sample unperturbed, thus creating a perfect shadow. However, at high optical depths, the ballistic photons are scarce as they decay exponentially while propagating through the probed volume. Due to dynamic range issues, an image formed solely on this contribution of light would not suffice, especially since the technique is intended for samples operating within the multiple scattering regime[4]. Remedying this issue involves the inclusion of those snake photons which during their passage through the sample managed to maintain their original directionality, thereby causing only little image distortion [61].

To fulfill the original intent of BI, different filtering procedures can be applied. Firstly, the transmitted light can be spatially filtered, preserving those photons exiting within roughly the same solid angle that they entered. One can furthermore utilize the temporal characteristics of the transmitted light. As each scattering event prolongs the path-length taken across the sample, different scattering orders exit the sample at different times, resulting in a temporal spreading of the incident light (see Fig. 4.16). Using a suitably short laser pulse in combination with an ultrafast gating system thus enables the rejection of the late arriving photons [62].

---

[4]At $OD = 10$ the incident light is reduced by a factor of $\sim 2 \cdot 10^4$.
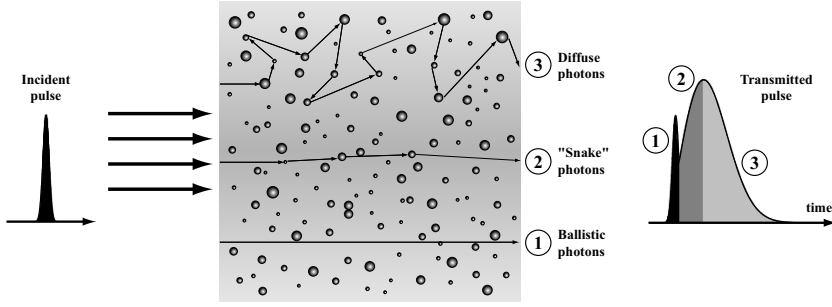
Figure 4.16: *Illustration of the different paths taken by either ballistic, snake or diffuse photons through a turbid scattering medium. Due to their prolonged path-length, diffuse photons arrive later and can be rejected by means of temporal filtering. Adapted from [17]*

One key aspect with BI is the possibility of producing instantaneous images of the turbid sample, which is of great importance when studying dynamic processes. Recent developments of BI furthermore allows velocity vectors to be extracted by implementing a double-pulsed laser source in combination with an interline transfer CCD chip [63, 64]. However, the technique is limited to line-of-sight information. Another disadvantage concerns the complexity and cost of a BI experimental setup.

Chapter 5

Structured Illumination

STRUCTURED Illumination (SI) constitutes the link between laser sheet imaging and SLIPI. This chapter provides a brief background of SI where the underlying concept is described. The chapter is divided in the two branches of structured illumination - optical sectioning and super-resolution. At the end of the chapter the first successful implementation of SI for macroscopic imaging of a two-phase flow is presented.

5.1 Background

Conventional wide-field (2D) microscopes are *diffraction limited*, meaning that two objects in the observed specimen must be separated a certain distance in order to resolve them as separate. The required distance depends on the numerical aperture (NA) of the collection optics and the wavelength of light. A large NA and a short wavelength provide a better resolving power[1]. In addition to lateral resolution, the axial (depth) resolution is also of importance since all objects are three-dimensional. The depth-resolution can be approximated by

$$\Delta z \approx \frac{n \cdot \lambda}{\text{NA}^2} \tag{5.1}$$

where n is the index of refraction of the medium in which the probed objected is immersed [65]. Thus, to maintain focus throughout the entire object a low NA should be utilized, which is in direct conflict with the desire to have high lateral resolution. Structured illumination is an imaging technique that provides a solution to this dilemma as it can produce optically sectioned images with, at least theoretically, unlimited spatial resolution.

The concept of optical sectioning is to "slice" the object of interest by optical means. This was the original intent and the motivation for the development of structured illumination microscopy (SIM). Other experimental solutions existed prior to the invention of SIM, where perhaps the best-known example is scanning confocal

---

[1]This is why Blueray disks can contain more data, the information is read by a blue laser rather than a red laser used in DVD players.
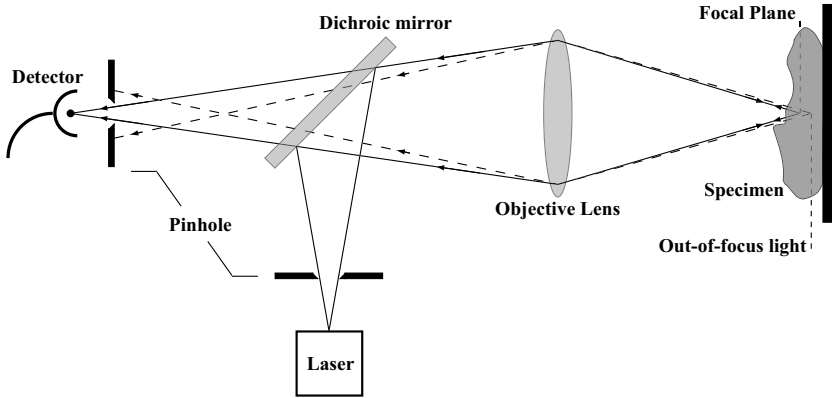
Figure 5.1: *A schematic of the optical arrangement for the scanning confocal microscope.*

microscopy (SCM). This technique has three main advantages compared to a conventional wide-field microscope. Firstly, its spatial resolution can be made ~1.5 times better. Secondly, it can reject light originating from out-of-focus regions of the three-dimensional sample and finally, due to its optical sectioning ability, it produces high-contrast images [66]. Unlike conventional microscopes, where the entire volume is illuminated simultaneously, a scanning confocal microscope utilizes point illumination. Figure 5.1 shows a schematic of the optical arrangement. The incident radiation is focused onto the sample at a certain point. The resulting signal (commonly fluorescence) is then focused through a pinhole and the intensity recorded. The incident illumination also generates signal from out-of-focus regions (dashed lines), however, this intensity will be mostly blocked by the pinhole.

As implied by its name, the method requires a scanning process, where either the beam or the specimen is physically moved, in order to acquire two-dimensional information. This renders low frame rates, typically in the order of 3 frames per second (other experimental solutions exist but yield lower spatial resolution) [65]. This feature makes the technique unsuitable for the study of dynamic samples. The need for a more time-efficient solution motivated the work leading to the invention of SIM.

5.2 Structured Illumination Microscopy

Structured illumination microscopy is commonly divided into two branches depending on the implementation. The first branch is related to optical sectioning, where SIM is used to reject out-of-focus light. The second application concerns the use of SIM to surpass the classical spatial resolution limit.

5.2.1 Optical Sectioning

Compared to confocal microscopy, structured illumination enables optical sectioning with improved speed, resolution, reduced cost while keeping a low experimental complexity. A typical optical arrangement for SIM is schematically illustrated in Fig.

5.2. A light source illuminates a mask target that adds sinusoidal intensity structure to the beam. Commonly, the mask target is attached to a mechanical actuator to control its position. A beam-splitter directs the structured light onto the sample and a part of the scattered light (or fluorescence) passes through the beam-splitter to finally be imaged onto a 2D detector array. One key difference between SIM and SCM is thus the implementation of wide-field illumination, which is the main reason for the boosted temporal resolution.
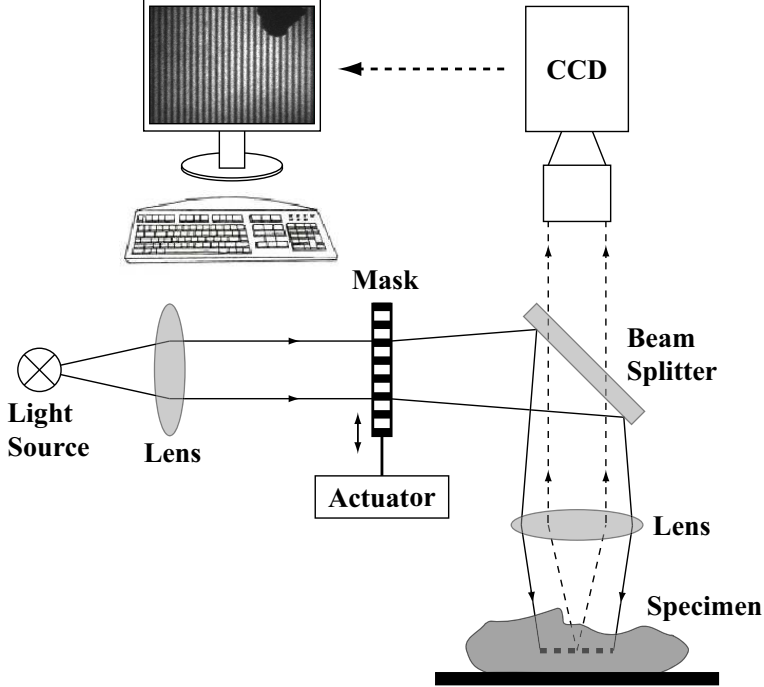

Figure 5.2: *Optical arrangement for structured illumination microscopy. The sample is illuminated with a sinusoidally modulated (2D) beam. This modulation is only visible in the in-focus plane.*

The illumination pattern used in SIM can be expressed according to Eq. 5.2 [67].

$$S_\phi(x, y) = 0.5 + m \cdot \sin\left(2\pi x \nu + \phi\right) \tag{5.2}$$

where m is the so-called *modulation depth*, ν denotes the frequency of the structure, x and y are Cartesian coordinates and ϕ is an arbitrary spatial phase of the sine wave. Note that although the beam is two-dimensional, the superimposed structure only varies along the x-direction. The value of m depends on the optical transfer function (OTF) of the system, where an undistorted illumination has $m = 0.5$ (i.e. the intensity alternates between 0 and 1). The sole purpose of the sinusoidal pattern is to give the in-focus light a recognizable signature to distinguish it from the photons originating from out-of-focus planes. It should be pointed out that, unlike SCM, the illumination scheme of SIM does not inhibit the detection of any light. However, all except the 0th spatial frequency orders naturally attenuate with defocus [68]. Thus,

if the spatial frequency of the superimposed grid pattern is chosen high enough it will only be imaged efficiently in the in-focus plane and blurred otherwise. The concept is illustrated in Fig. 5.3, where a sphere is illuminated (from above or below) with a sinusoidal intensity pattern. Since light from the entire illuminated volume is detected, the recorded image is the line-of-sight integrated intensity. This is illustrated in the example by the nine different image layers and the recored image is constructed by adding the intensity from each of these. Observe how the sinusoidal intensity pattern is only visible in the in-focus (middle) planes, making these layers distinguishable from the surrounding ones. Hence, the implementation of structured illumination allows the light originating from an optically selected layer (with a certain thickness) within the sample to be recognized in the post-processing.
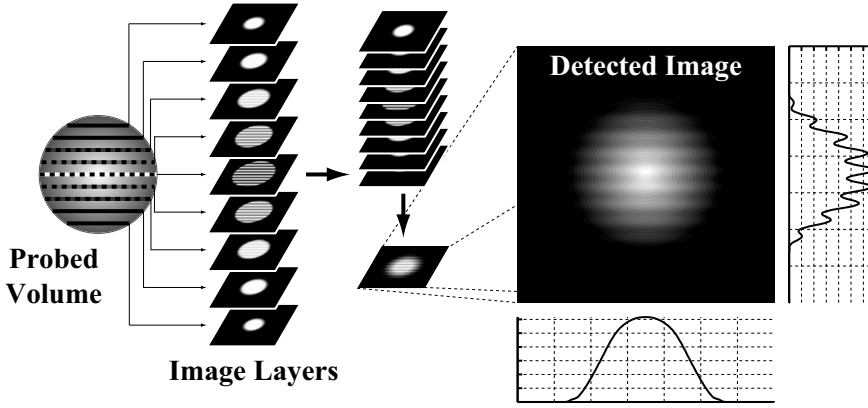

Figure 5.3: *The principle of structured illumination. A sphere is illuminated (from above or below) with a sinusoidally modulated beam. The fringes are, however, only visible in the in-focus (middle) planes.*

The illumination in Eq. 5.2 leads to an image of the form

$$I_\phi(x, y) = I_C(x, y) + I_S(x, y) \cdot \sin(2\pi x \nu + \phi) \tag{5.3}$$

Here $I_C(x, y)$ denotes the conventional image one would obtain using an ordinary wide-field microscope, hence constructed from both in- and out-of-focus light. The second term, $I_S(x, y)$, is the local amplitude of the modulation (which is represented by the sine term) and bears information from the in-focus plane of the sample. For example, an amplitude of zero at any given point within the image would indicate the presence of a void in the focal plane of the specimen. If the intensity in this specific point furthermore has a non-zero value, this light must originate from an out-of-focus region.

The aim of SIM is thus to extract I_S while simultaneously removing both I_C as well as the sine term. Neil *et al.* demonstrated that this can be achieved by recording three intensity modulated images with spatial phases 0, $2\pi/3$ and $4\pi/3$ [67] (or in degrees: 0°, 120° and 240°), see Fig. 5.4. Such a phase shift is created by physically sliding the mask using the actuator (other means of performing the phase shift are discussed in Chapter 7). This change will only be visible in the in-focus plane since the modulation pattern is completely blurred in the out-of-focus sections. It can be

shown that

$$I_S = \frac{\sqrt{2}}{3} \cdot \sqrt{(I_0 - I_{2\pi/3})^2 + (I_0 - I_{4\pi/3})^2 + (I_{2\pi/3} - I_{4\pi/3})^2} \qquad (5.4)$$

which is equal to calculating the root-mean-square (RMS) of the images [65]. By implementing Eq. 5.4, all image details which are identical in the three raw data images are removed, while unique features are preserved. The former intensity contribution comes from out-of-focus layers where the induced phase shift is not visible, while the latter arises from the in-focus plane. It is also possible (mostly for comparison reasons) to reconstruct I_C from the three images by calculating

$$I_C = \frac{I_0 + I_{2\pi/3} + I_{4\pi/3}}{3} \qquad (5.5)$$

which is simply the average of the images. Figure 5.5 illustrates the final step of the SIM approach, where the object is illuminated thrice with different ϕ. The resulting SIM image, calculated using Eq. 5.4, contains only information from a thin section. The conventional image, calculated using Eq. 5.5, is contaminated with out-of-focus light, leading to poor depth-resolution.
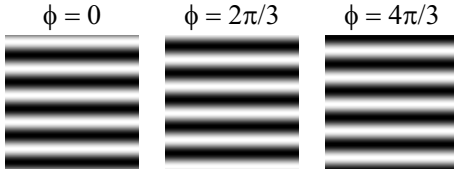

Figure 5.4: *Three sinusoidally modulated intensity patterns, offset 1/3 spatial period between each frame.*

Drawbacks

Although characterized by low cost, low complexity, simple image reconstruction algorithms and relatively fast image acquisition times, the SIM method is not always the preferred technique. The illumination scheme can lead to image artefacts in the shape of residual line structures which can be difficult to correct for. The appearance of such artefacts and means to avoid them are discussed in Chapter 7. Furthermore, the need for *three* acquisitions is particularly unfortunate as there is a broad variety of high quality equipments (double-pulsed lasers and interline transfer CCDs) available to achieve two, but not three, realizations within a short time scale. This feature often limits the usefulness of SIM to stationary objects, unless time-averaged data is sufficient. This issue was addressed by Krzewina and Kim who developed an optical system capable of producing single-exposure SIM images [69]. To achieve this the authors utilized a white light source in combination with a color grid. A color sensitive camera allowed the simultaneous recording of the three spatial phases. A second solution to this problem was presented by Wicker and Heintzmann, who utilized polarization-coded SIM, also allowing instantaneous realizations [70].
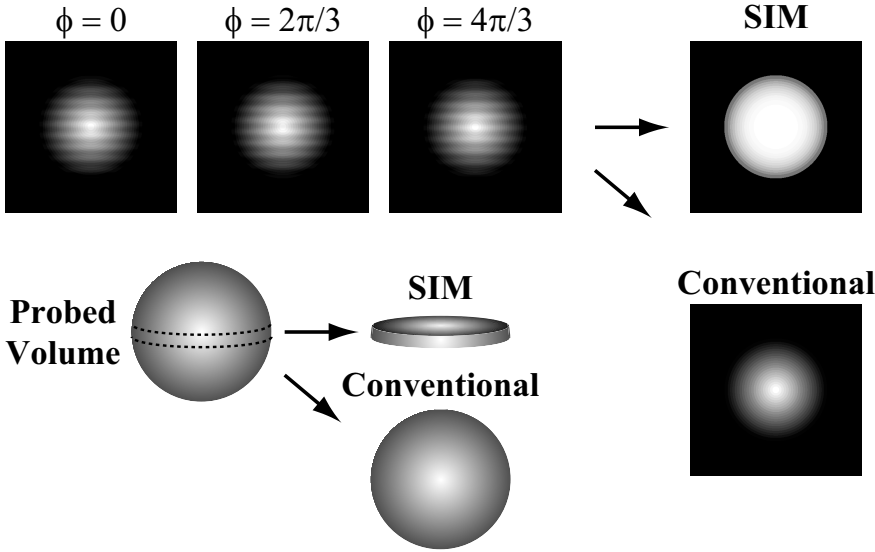
Figure 5.5: *Optical sectioning principle of SIM. The sample is illuminated three times, between which the spatial phase of the modulation is shifted 1/3 of the sine period. The incident radiation illuminates the entire volume of the specimen but by applying Eq. 5.4 only the in-focus information is retained.*

5.2.2 Improved Lateral Resolution

The maximum spatial frequency observable with a light microscope is set by $f_c = 2 \cdot NA/\lambda$, where λ is the wavelength of the detected light and NA is the numerical aperture of the objective lens [71]. Spatial frequencies beyond this limit, which is commonly referred to as the *cutoff frequency*, are completely attenuated by the OTF. As an example, the finest observable details of a sample immersed in dye emitting radiation at 500 nm captured with a numerical aperture of 1.4 is about 200 nm. In 2000, Gustafsson found a loophole in this physical law and demonstrated an approach, which is based on structured illumination, that allows image details beyond this limit to be observed [72, 73].

Even though spatial frequencies greater than f_c is physically unaccessible with a light microscope, they can be shifted into the observable region in the form of so-called *Moiré patterns*. This effect occurs when two fine patterns are superimposed multiplicatively, thus creating a beat pattern. Probably the best-known example of Moiré fringes is when two combs are put on top of each other, but the effect can be observed in everyday life as illustrated in Fig. 5.6.

The concept of extended resolution using structured illumination can be explained by converting the sample structure into reciprocal space, i.e. its Fourier transform. In short, the Fourier transform representation of a two-dimensional specimen is a mapping of its spatial frequency contents, where low resolution information (smooth variations) resides close to the center, while high resolution information (sharp changes) lies further away (see also Chapter 7). The frequencies a microscope can resolve are restricted by a circular region, set by f_c, around the center (Fig. 5.7 b)). To increase

Figure 5.6: *Examples of Moiré patterns observed in everyday life.*

the resolution of a microscope, this circular region must be expanded. This can be achieved by illuminating the sample with a sinusoidal illumination pattern.
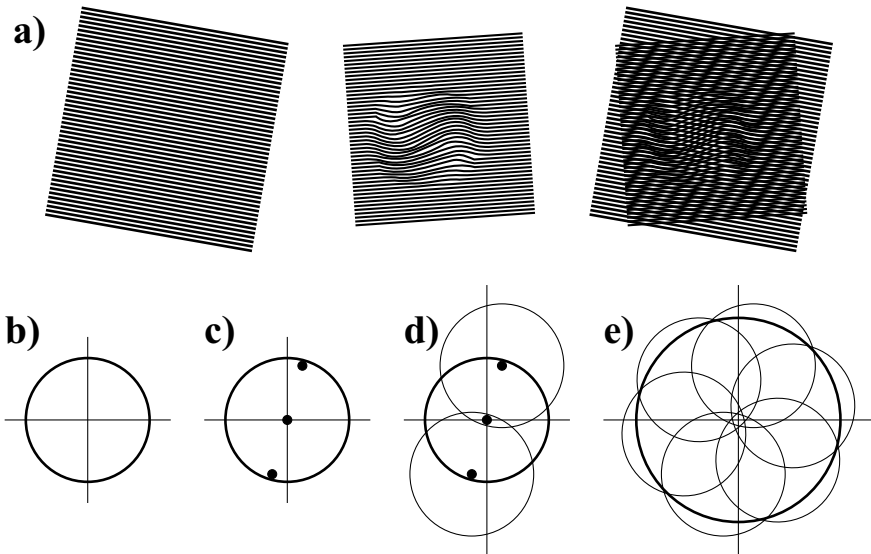

Figure 5.7: *a): Two fine patterns which are multiplied create Moiré fringes. b): The observable region of a conventional microscope in reciprocal space. c): The Fourier transform of the incident sinusoidally modulated illumination. d): The recorded image will contain information moved from the two offset regions. e): Observable region extended by recording several intensity modulated images, where the modulation has different orientation. Adopted from [72].*

A perfect noise-free sinusoidal intensity pattern contains only three non-zero points in reciprocal space (Fig. 5.7 c)). The central point is the intensity dc-offset, the remaining two describe the spatial frequency of the modulation ($\pm\nu$). Note that since the same objective lens is used to both illuminate the sample as well as detect the generated signal, the frequency of the incident sinusoidal pattern must reside within the cutoff frequency limit. To explain the technique, assume that the leftmost fringe pattern in Fig. 5.7 a) represents the incident illumination. Its frequency component is chosen to be as high as allowed by the OTF, i.e. its $\pm\nu$ components lies just within the border of the observable region (Fig. 5.7 c)). The second fringe pattern represents the sample under investigation and contains spatial frequencies

normally fully attenuated by the OTF. These cannot be observed directly, but the detected image will contain Moiré fringes (Fig. 5.7 a)). These beat patterns bear high frequency information that has been moved from the two offset regions in Fig. 5.7 d), i.e. previously unobservable contents, into the observable region. However, the structural information shifted from outside f_c is not directly accessible, since it, in the form of Moiré fringes, lies at the wrong position in reciprocal space. To gain resolution beyond the diffraction limit, these frequency components must be restored to their original position (outside f_c), which can be achieved by using a phase-shift approach in the same manner used to achieve optical sectioning using SIM [72]. Finally, to expand the observable region symmetrically around its origin, the incident sinusoidal intensity pattern must be rotated and the procedure repeated. This is illustrated in Fig. 5.7 e) for three angular positions of the illumination ($0°$, $120°$ and $240°$). By selecting $\nu \approx f_c$, the spatial resolution can be improved by a factor of almost 2. Despite the need for multiple recordings, the total acquisition time can be reduced by using a ferroelectric liquid crystal on a silicon spatial light modulator[2]. Kner *et al.* demonstrated how this experimental approach can be used in combination with structured illumination to obtain super-resolution videos with frame rates up to 11 Hz [74]. A comparison between conventional wide-field microscopy, SCM and the SI approach is shown in Fig. 5.8.
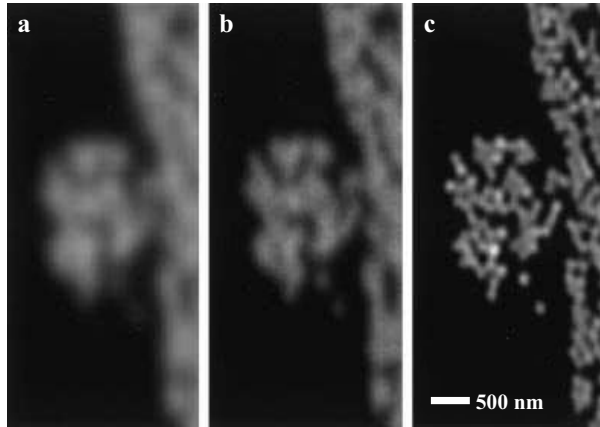

Figure 5.8: *Example illustrating the improvements in image resolution.* ***a):*** *Conventional wide-field microscopy.* ***b):*** *Scanning confocal microscopy.* ***c):*** *Structured illumination [72]. With courtesy of John Wiley and Sons.*

In 2005 Gustafsson demonstrated how to gain (theoretically) unlimited resolution using a similar concept [71]. To expand the observable region even further, a nonlinear approach is utilized. When a fluorescing sample is illuminated with high intensity, the fluorophores respond nonlinearly due to saturation. If the intensity of the light source is modulated sinusoidally, saturation leads to a distortion of the sine wave and higher harmonics, that are multiples of the fundamental spatial frequency ν, appear. The effect is illustrated in Fig. 5.9 a), where each point residing beyond f_c represents such a harmonic. Each of these frequency components will move higher resolution

---

[2]This device is in principle a reflecting screen, where the reflectivity of the pixels can be modified rapidly. The intensity profile of a reflected beam will thus depend on the "image" written onto the screen. The drawbacks with this device is its low damage threshold and the fact that the "image" is discrete with pixel values that can only be turned either on or off.

information within its corresponding offset circle (Fig. 5.9 b)) towards lower spatial frequencies in the form of Moiré patterns. Since there is no direct limit on the number of harmonics that can be generated, unlimited resolution can, in principle, be achieved. In practice, however, the method is limited because of the unavoidable noise level which not all harmonics are strong enough to exceed. As for the linear approach, the method requires different orientations of incident light source to expand the observable region symmetrically around its origin (Fig. 5.9 c)).
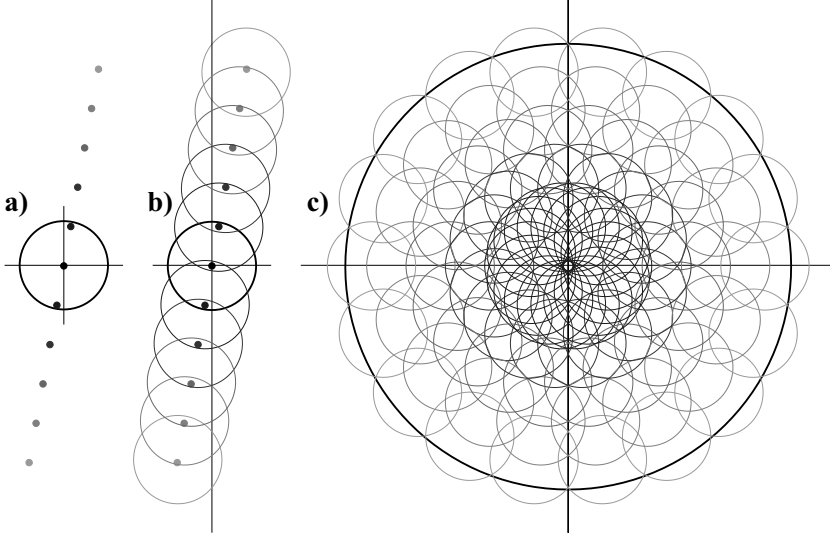

Figure 5.9: *Principle of unlimited image resolution using SIM. **a)**: Under conditions of saturation, the incident sinusoidal structure is distorted and harmonics of the fundamental frequency component are created. **b)**: Each harmonic component brings high-frequency information towards lower frequencies. **c)**: By illuminating the sample with different orientations of the sinusoidal pattern, the observable region can be expanded, in theory, indefinitely. Adopted from [71].*

5.3 Macroscopic Imaging

5.3.1 Background

Despite the clear benefits with structured illumination, only a handful of publications concerning applications within macroscopic imaging can be found in the literature[3]. Caulier *et al.* implemented SI to inspect the quality of high-reflective surfaces [75], an approach not much different from the one demonstrated by Cortizo *et al.*, who used SI to study the topography of the sole of the foot during a walk [76].

In Paper I the applicability of SI for macroscopic imaging of non-static objects was investigated, with the purpose to determine whether the technique could act as

---

[3]The terms microscopic and macroscopic imaging are somewhat vague and undefined, without a clear border. Here, the term macroscopic imaging refers to object scales observable by the human eye without the aid of lenses.

a supplement to laser sheet imaging. Even though the SI approach was expected to perform less satisfactory, this work was motivated by the fact that laser sheet measurements require a minimum of two optical ports, one for insertion of the light sheet and one for observation. Structured illumination, on the other hand, requires only a single optical access. Reducing the number of optical ports is, especially for combustion related research, key in order to achieve more realistic measurement scenarios. One example where the number of optical components is hindering the achievable operating conditions is in in-cylinder studies of IC engines. Here, the laser sheet is commonly inserted into the cylinder via a quartz liner, whereas the generated signal is detect through a quartz piston. Due to different heat transfer properties between quartz and metal, the use of optical ports affects the in-cylinder conditions. Furthermore, the required optical components cannot withstand too high engine loads. In other cases, two optical ports are simply unobtainable, e.g. inside full-scale industrial combustors (furnaces).

Structured illumination is, however, not the only single-ended approach available. Eckbreth and Davis developed a coaxial light detection geometry that rejects out-of-focus light [77]. The method consists of positioning an obscuration disk in front of the collection optics which blocks the central part of the lens. The disk inhibits the detection of light incident with a low angle, leading to a decreased depth-of-field (DOF). This approach is, however, mostly suitable for point measurement applications. A second alternative method is the LIDAR (LIght Detection and Ranging) technique, which is based on temporally resolving the back-scattered light from a pulsed laser [78]. Unlike the obscuration disk method, LIDAR is suitable for both point and 2D measurements, yet achieving an axial resolution of $\sim 10^{-3}$ m requires an ultrashort laser pulse (picosecond range) in combination with a camera with an adequate temporal resolution, making a LIDAR system very expensive.

5.3.2   Experimental Arrangement

For the SI method to function properly, the superimposed sinusoidal structure should only be visible in the in-focus plane. This can be achieved using two approaches; (1) creating a sharp image of the line pattern that quickly defocuses with distance or (2) using a detection system with a small DOF. Often in SIM the same objective is used to both illuminate the sample and collect the signal [79]. In these cases the depth-resolution is set by either (1) or (2), whichever is lowest. In the measurements presented in Paper I, the second method was used, due to the difficulty of achieving both a relatively wide illuminating beam (to get a reasonable field-of-view) in combination with rapid defocussing.

To determine the DOF of the system, a flat reflecting object (mounted on a translational stage) was positioned within the cameras field-of-view (FOV). By moving the object axially, the variations in modulation depth m, as a function of distance, could be determined. The result of this procedure is shown in Fig. 5.10, where the graph shows the ratio between the magnitude of the fundamental frequency component and the dc-offset (maximum value normalized to unity). From this plot, the DOF (FWHM of the curve) of the optical arrangement was determined to be ~ 4 mm.
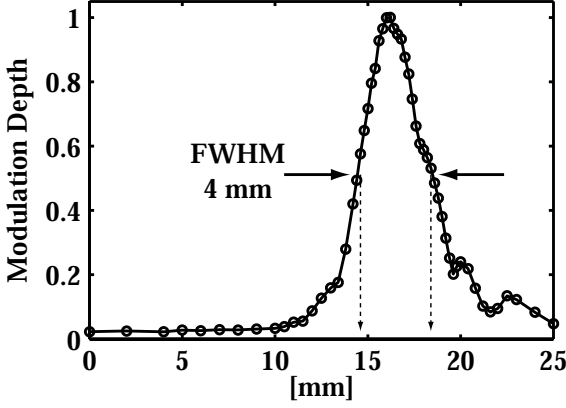
Figure 5.10: *Plot showing the ratio of the magnitude of the 1st and 0st order frequency components as a function of distance. From the full width at half maximum (FWHM), the DOF was determined to be ~ 4 mm.*

Figure 5.11 illustrates the result in Fig. 5.10 visually. In this example, an object consisting of five different layers is illuminated (see schematic in Fig. 5.11). By traversing the object it can be seen how the different layers falls within the focal plane. Since the distance between some of the layers is less than the DOF of the imaging system, the modulation is sometimes apparent in two layers at the same time.
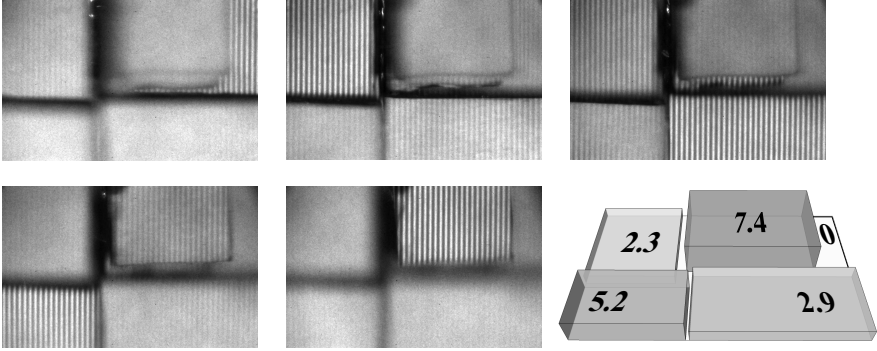

Figure 5.11: *An object consisting of five layers, illuminated with the SI system at different axial positions. The numbers given in the schematic indicate the relative thicknesses of the layers (in mm).*

5.3.3   Results

The capabilities of the macroscopic single-ended SI system was tested on a flow of water droplets, generated by a nebulizer. A stream of nitrogen was introduced in the central region of the flow, with the purpose of adding an internal (recognizable) structure to the sample. A region of approximately 16×14 mm^2 directly above the nebulizer was imaged and the object was arranged so that the focal plane coincided with the nitrogen outlet (tube $\varnothing \approx 5$ mm).

The results are provided in Fig. 5.12, showing one of the three modulated images, the conventional result as well as the structured illumination image. A vertical sum-

mation (between the dashed lines in the modulated image) is also presented beside each image. Note that the conventional image is constructed from the three subimages (Eq. 5.5) and not by illuminating the sample with a non-modulated wide-field beam.

Without suppressing the of out-of-focus light, the flow of nitrogen is barely visible (conventional case). Because of the lack of scatterers in this region, the modulation amplitude drops significantly here. This can be seen both in the vertical summation and in the magnification of the top image. The intensity in the SI image drops accordingly here, indicating a successful implementation of the technique. Note that the SI intensity is not expected to reach zero in the nitrogen region, due to the shape of the DOF function. Finally, it can be mentioned that unlike the results presented in Paper I, no noise reduction, by means of low-pass filtering, has been performed on the results in Fig. 5.12.
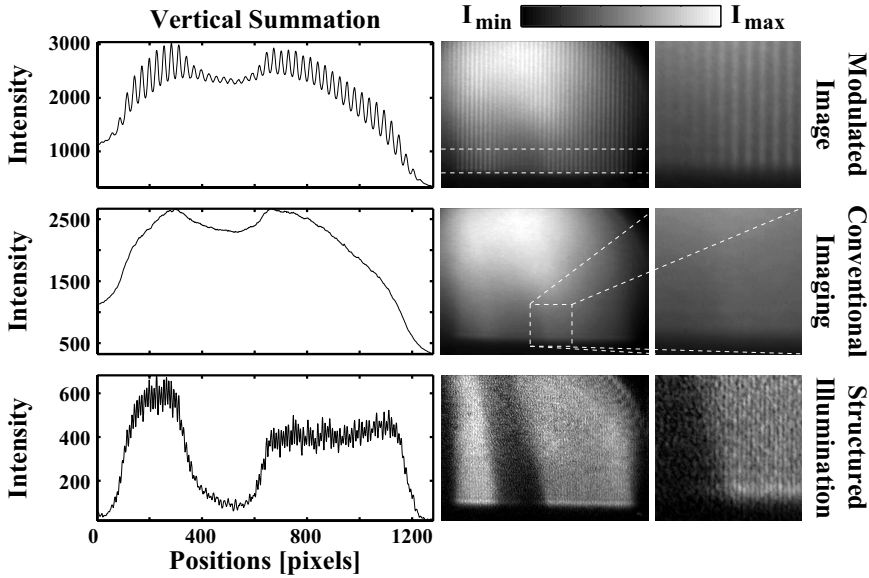

Figure 5.12: *Comparison between conventional backscattering imaging and structured illumination, here tested on a flow of water droplets. To add internal structure to the sample, a stream of nitrogen was inserted into the center of the flow. Conventional imaging collects light from the entire illuminated volume, making the internal flow barely visible. By implementing structured illumination, out-of-focus light is discriminated against, allowing visualization of the internal geometry of the sample. The dashed lines in the top image indicate the boundaries for the vertical summation.*

Part II

SLIPI

Chapter 6

Structured Laser Illumination Planar Imaging

SLIPI combines the benefits of structured illumination with those of planar laser imaging. If accurately executed, the SLIPI technique discriminates against multiply scattered light, leading to improved and enhanced visualization of sprays and other turbid media.

This chapter starts by providing a brief introduction to the SLIPI technique. The remainder of the chapter is thereafter divided in two parts, focusing on either qualitative or quantitative imaging. Some of the known limitations with the SLIPI technique are also discussed at the end.

6.1 Introduction

Although the majority of publications concerning structured illumination use a wide-field (2D) illumination scheme, the method can easily be combined with laser sheet imaging. In fact, this approach has three main advantages compared to wide-field illumination; (1) the generated signal is detected at 90 degrees, thus avoiding signal losses due to the beam-splitter (see Fig. 5.2), (2) optically thicker samples can be probed and (3) the intensity profile of a laser sheet is, in principle, one-dimensional and can therefore more easily be made uniform. The last point is important because it reduces the risk for residual line structures, which is a common issue with structured illumination.

The planar approach of SI was first implemented in the field of microscopy in 2007 by Breuninger *et al.* who demonstrated its contrast-enhancing capabilities by applying the technique on a static biological sample (fruit fly) [80]. In their work they referred to the technique as SPIM-SI, standing for Single Plane Illumination Microscopy - Structured Illumination. However, for the work presented in this thesis the abbreviation SLIPI (Structured Laser Illumination Planar Imaging) will be used instead, to differentiate between microscopic and macroscopic imaging.

6.1.1 Multiple Scattering Suppression

Experimentalists using laser sheet imaging do not strive for super-resolution, nor is there a need for optical sectioning since this feature is already embedded in the technique. It might therefore seem somewhat peculiar to combine planar laser imaging with structured illumination, since the two main advantages associated with SI - improved lateral resolution and optical sectioning - are seemingly unnecessary. These arguments are valid when optically dilute ($OD < 1$) samples are of interest. However, when optically dense or thick samples are probed, the laser sheet thickness increases due to multiple light scattering which can severely reduce the sectioning capability of the technique. The implementation of structured illumination can remedy this undesired effect.

The main purpose for spatially modulating the intensity profile of a laser sheet is to create a predetermined condition for *where* in space scattering events are allowed to take place. To understand the concept, it is useful to think of the incident laser sheet as though constructed out of several parallel lines, in-between which the intensity is initially zero[1]. The singly scattered photons are thus "forced" to scatter according to the superimposed line structure, whereas the multiply scattered light can appear to originate from the intermediate (zero intensity) region (compare with Fig. 3.7), analogous to the out-of-focus light in SIM. Figure 6.1 illustrates the effect for five spray systems with different levels of turbidity, ranging from approximately $OD = 0.5$ to $OD = 6$. Even thought the line frequency is significantly different from case to case, it is clearly noticeable how the line structure diminishes more rapidly with distance as the optical thickness increases. In the diesel spray, the line pattern is only observable at the entrance side. This comes as no surprise as the unperturbed light intensity (which carries the line structure) at the exit side is, according to the Beer-Lambert law, only 0.25% of that at the entrance side at an optical depth of 6. For a 14-bit camera this corresponds to a drop in photon counts from 16383 to merely 41. A good dynamic range is thus imperative when probing optically dense media using SLIPI in order to fully resolve the entire sample.
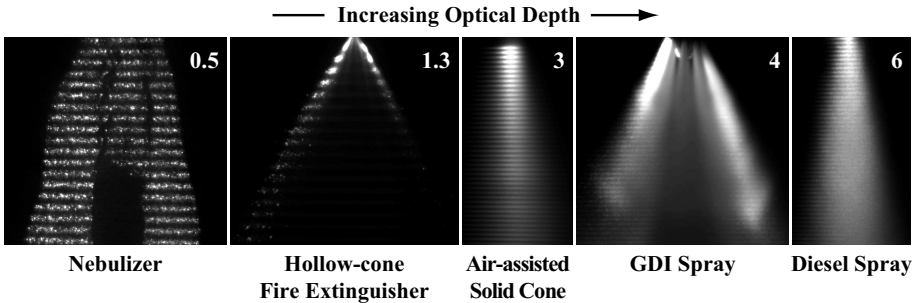

Figure 6.1: *A structured laser sheet propagating through different scattering media with different levels of turbidity (an estimate of the OD is given in the upper right corner). With increasing optical thickness, the line structure become less and less prominent. In the images, which are histogram normalized, light enters from the left.*

---

[1] Assuming a "perfect" modulation depth m (see Eq. 5.2).

Another way to view the approach is in terms of modulation. When illuminating a sample with a structured laser sheet, the intensity recorded from a given point comprises a dc offset and an amplitude, the latter being a measure of the local unperturbed light intensity. In an ideal measurement environment, free from distortions and noise, these two components are equal (see Eq. 5.2). However, in more realistic scenarios, as those shown in Fig. 6.1, the amplitude decreases with distance in comparison to the dc offset. This is because singly scattered light carries the incident structured pattern, whereas the multiply scattered light appears as an intensity offset[2]. The aim of SLIPI is to extract the local amplitude of the modulation and to fully remove the dc offset induced by multiple light scattering. This can be achieved by using the same approach utilized to remove out-of-focus light in SIM, i.e. by altering the spatial phase of the modulation. By doing so, a slightly different region within the sample is illuminated and if the line structure is sufficiently fine, this shift will go unnoticed for the multiply scattered light. Under these circumstances, the undesired diffuse light intensity contribution can be removed by applying Eq. 5.4. An example of the approach is given in Fig. 6.2, showing the three modulated subimages (I_0, $I_{2\pi/3}$ and $I_{4\pi/3}$) from which either a SLIPI or a conventional image can be formed. The term "conventional" is used to differentiate between a normal laser sheet image and the one constructed by implementing Eq. 5.5. However, in theory, they are equal. This terminology will be used for the remainder of the thesis.
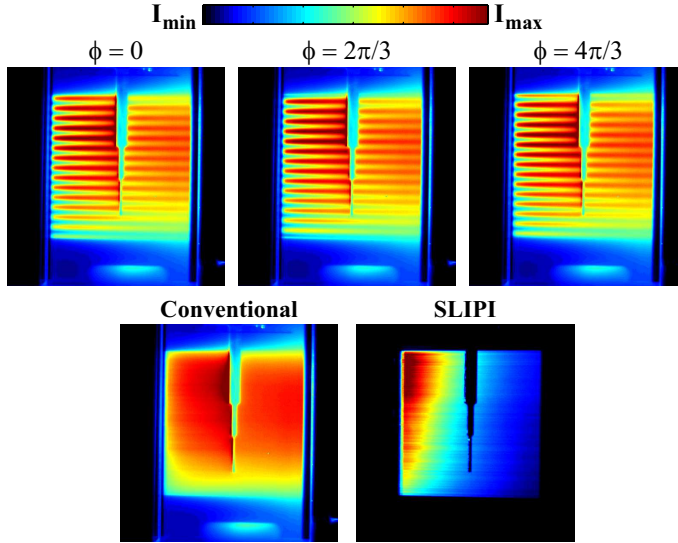

Figure 6.2: *Multiple scattering suppression using SLIPI, illustrated here on the same sample as in Fig. 4.13. Notice how the removal of multiply scattered light leads to a negligible intensity in the "zero area".*

Regardless of the optical arrangement (planar or wide-field illumination), structured illumination requires a minimum of three intensity modulated images, phase-shifted 1/3 of the spatial period, to accurately reconstruct the whole sample. However,

---

[2]This statement is not entirely accurate since the incident intensity modulation has an embedded dc offset; the factor 0.5 in Eq. 5.2.

it is possible to use a larger number of raw data images instead. By recoding N spatially modulated images, with a relative phase shift of $2\pi/N$, a structured illumination image can be formed by applying

$$S = \frac{\sqrt{2}}{N} \cdot \left(\sum_{i=1}^{N-1} \sum_{j=i+1}^{N} (I_i - I_j)^2 \right)^{1/2} \tag{6.1}$$

which is a generalized form of Eq. 5.4, valid for N number of subimages ($N \geq 3$). It should be pointed out that it is still unclear whether an increased number of modulated images improves the multiple scattering suppression ability of SLIPI.

6.1.2 SLIPI Optical Arrangment

A typical optical arrangement for SLIPI (illustrated in Fig. 6.3) is in many ways similar to a SIM setup. Although not a requirement, it is preferable to obtain a near top-hat intensity profile as this leads to fewer uncertainties and image artefacts. Such a profile can be achieved by first expanding the beam by means of a Galilean telescope and then physically blocking the periphery of the Gaussian intensity profile with an aperture. A mask, situated directly after the aperture, adds structure to the light beam. The mask ordinarily consists of a target either with a sinusoidally varying transmission or with alternating opaque and transmissive stripes (commonly referred to as a Ronchi grating or, sometimes, simply a grid). Being more light efficient, the latter of the two alternatives is the preferred choice in most applications [81]. In addition, Ronchi gratings usually have a higher damage threshold because the opaque strips reflect the incoming light, rather than absorbing it. This is usually not an issue in microscopy but can be an important aspect when implementing pulsed laser systems, where the mask is subjected to a large amount of energy during a short time interval.
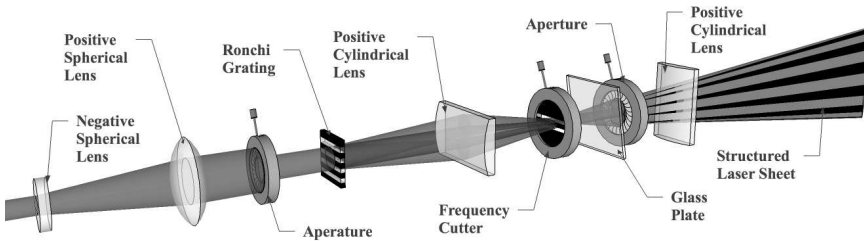

Figure 6.3: *Optical arrangement for a typical SLIPI setup.*

Depending on the choice of the mask, spatial filtering of higher order harmonics may be required. A square wave target (Ronchi grating) produces odd harmonics of the fundamental frequency, which, as will be illustrated in the following chapter, can render undesired residual line structures in the final SI image. Regardless of the mask, a complete SLIPI setup requires means to shift the superimposed structure. As mentioned in the previous chapter, an actuator linked to the mask is well suited for this task. An alternative approach is to tilt a glass plate, situated directly after

the spatial frequency cutter, to certain predetermined angles. By doing so, the whole beam is parallel displaced. The drawback compared to the actuator approach is that a calibration must be performed to determine the correct angles. A positive cylindrical lens is then finally used to compress the laser beam into a structured laser sheet.

6.2   Average Imaging

Due to the requirement for multiple acquisitions, the most straightforward approach is to apply SLIPI for averaged imaging. Compared to "single-shot" imaging (which will be discussed shortly), this approach reduces the experimental complexity, cost and data post-processing.

The first demonstration of average SLIPI imaging was presented in Paper III. The nozzle used in the experiment was a *Danfoss* 1910 pressure-swirl nozzle type, which produces a mist of droplets commonly used to extinguish fires. The liquid was pressurized to 50 bar and continuously issued into an optical chamber at atmospheric gas pressure. Figure 6.4 shows a comparison between the images obtained using either conventional planar laser imaging or SLIPI.
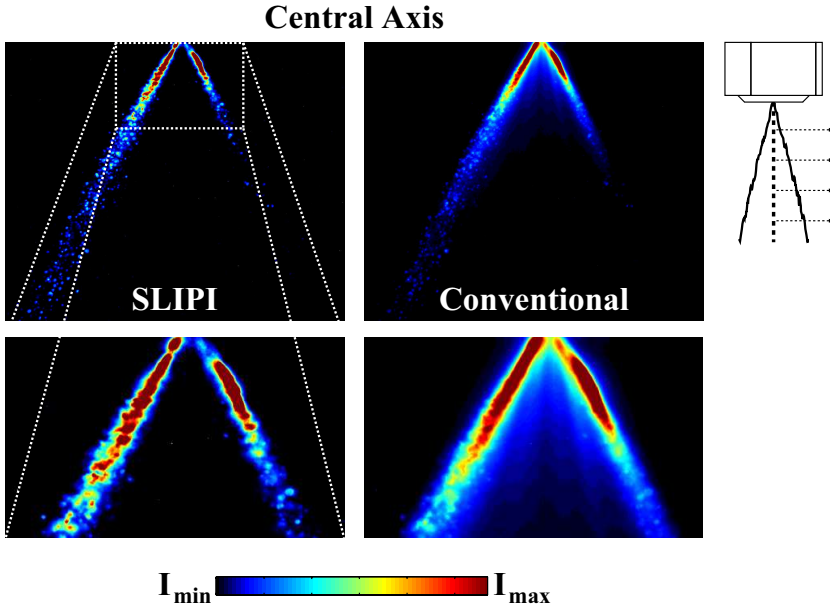
Central Axis

Figure 6.4: *SLIPI and conventional laser sheet imaging (histogram normalized) applied on a hollow-cone water spray. The structured laser sheet was positioned along the central axis of the spray, as indicated by the drawing. The light enters from the left.*

According to the manufacturer, the pressure swirl nozzle should produce an inner conical structure, mostly free from droplets. Smaller droplets may, however, be transported into the central region due to e.g. vorticities in the air flow, but the scattered intensity from these are expected to be significantly lower compared to the scattering intensity from the surrounding liquid sheet. Despite this, a non-negligible intensity

contribution is observed in this region in the conventional laser sheet image. This is a direct consequence of multiple light scattering, making photons falsely appear as though originating from the hollow region (compare with Fig. 3.7).

As seen in the figure, SLIPI efficiently removes this erroneous intensity contribution as well as the blurriness surrounding the downstream droplets, leading to sharper image gradients and more detailed information. Note that both the conventional image and SLIPI are constructed from the same raw data images.

Accurate suppression of the diffuse light can only be achieved by analyzing the contribution from multiple scattering in each pixel and to perform a non-uniform 2D intensity thresholding. This is the key feature of SLIPI which distinguishes it from other planar imaging techniques. Figure 6.5 demonstrates how the use of a uniform intensity threshold leads to losses of important spray features. Choosing an intensity threshold to make the inner region appear completely hollow cannot be achieved without sacrificing structural information regarding the dilute downstream flow where the intensity is relatively weak.
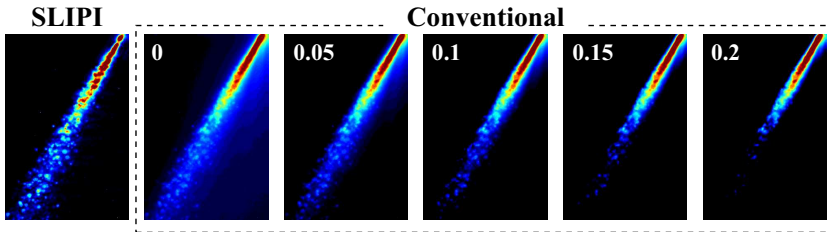

Figure 6.5: *Uniform intensity thresholding applied on the conventional image. The images are normalized to unity and the threshold is specified in each image. Notice how the approach leads to a loss of information regarding the dilute downstream region.*

Apart from multiple scattering, both conventional planar laser imaging and SLIPI suffer from laser extinction and signal attenuation. The exact influence of signal attenuation is not readily identified as it depends on the three-dimensional distribution of droplets between the laser sheet and the camera. However, assuming the spray to be circularly symmetrical, the reduction of intensity from the two regions where the laser sheet intersects the liquid sheet should be of comparable magnitude. Under these conditions, the apparent difference in intensity between the entrance and exit side is mainly caused by laser extinction. SLIPI does not correct for this, but rather enhances the effect as multiply scattered light, which illuminates the exit side of the sample, is suppressed. Bidirectional illumination could remedy this undesired effect but would double the acquisition time. It should be pointed out that the optical depth of the probed spray was estimated to ∼1.3, i.e. the spray was not far from being classified as optically dilute. Thus, the effects illustrated in Fig. 6.4 will be enhanced even further when probing optically thicker media.

Unlike steady-state two-phase flows, which can be probed using continuous laser sources, the visualization of transient sprays requires pulsed lasers in order to freeze the motion in time. Figure 6.6 illustrates such a measurement, where averaged SLIPI was utilized to visualize a 10-hole GDI injector at different times after start of injection. SLIPI provides similar improvements in image details as those discussed above.
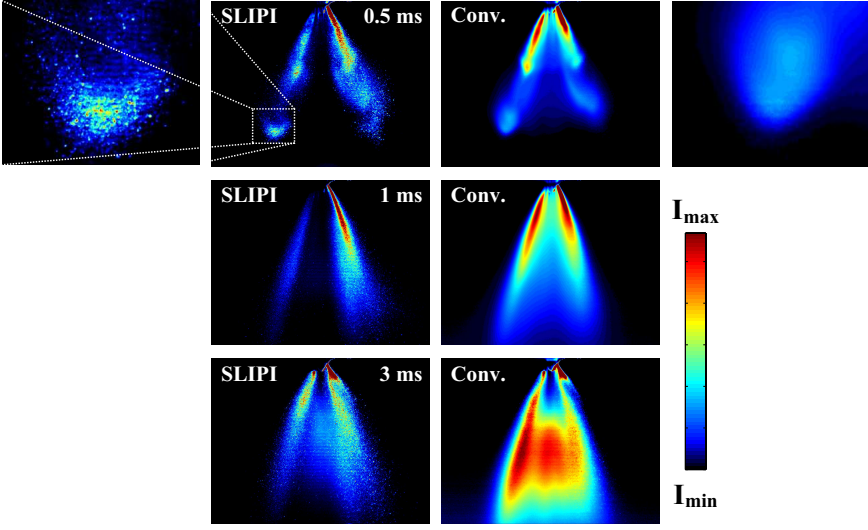
Figure 6.6: *Averaged SLIPI and conventional imaging applied on a 10-hole GDI injector. The magnified area shows the leading edge of the spray. Laser enters from the right.*

6.3   Time Resolved Imaging

6.3.1   High-Speed SLIPI System

Because the SLIPI technique requires three modulated images to be acquired in order to rebuild the sample without sacrificing spatial resolution the method is more suitable for average imaging. However, by recording the three images on a sufficiently short time scale the flow of a dynamic motion can be frozen in time, thereby allowing a semi-"single-shot" SLIPI image to be extracted. Depending on the time scales governing the flow of interest, different experimental solutions can be employed. Paper II demonstrates such an experimental approach, capable of acquiring three modulated laser sheet images within $\Delta t \sim 100~\mu$s. To extract a "single-shot" SLIPI image using this setup, the flow must remain static during Δt. However, the temporal resolution of the system is not only governed by the acquisition time but depends also on the spatial resolution. For the results reported in Paper II, a pixel-to-pixel displacement occurred for sample elements having a lateral velocity greater than $\sim$25 cm/s. This temporal resolution is not sufficient for atomizing spray systems, where droplets can reach velocities well above 100 m/s, but adequate for studying a flow of droplets produced by a low-pressure nebulizer. Attempting to probe a flow with droplets velocities greater than the temporal resolution of the system leads to an error called *ghosting*. The effect is shown in Fig. 6.7. Ghosting arises as individual droplets move during the time in-between the laser pulses.

The system in Paper II used two Nd:YAG lasers, one running in single-pulsed mode and one in double-pulsed mode, to create the three required laser pulses. Even though the laser sources utilized throughout the experiment were capable of producing double-pulses with a time-separation of $\sim$25 μs, this lower limit was not practically achievable due to intensity losses in the setup. The spatially overlapped beams were
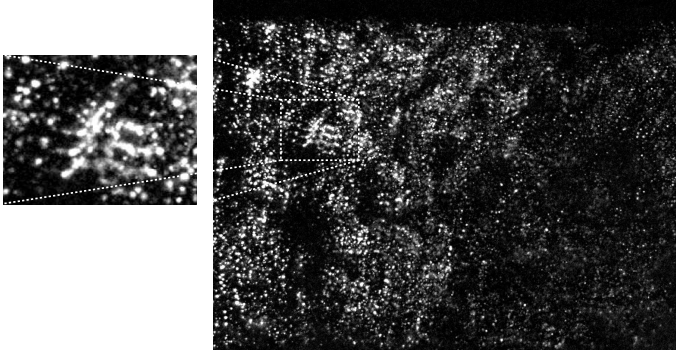
Figure 6.7: *Ghosting caused by the displacement of droplets during the acquisition time. The image was acquired in the spray region of the hollow-cone spray shown in Fig. 6.4.*

guided through a grating to add structure to the beams. A relatively thick oscillating glass plate, situated after the grating, was used to perform the phase shifting. The structured laser sheet, which was created by one negative cylindrical and one positive spherical lens, was then finally sent through the sample. Because of the short time-separation between the pulses, a multi-frame intensified CCD (ICCD) camera system was employed to record the scattered light. In this case, where three individual CCD chips are utilized, accurate background removal becomes essential, in contrast to average SLIPI imaging where the natural background intensity offset is equal in all three frames and thus removed when applying SLIPI. A further complication concerns the precise pixel-to-pixel overlap required when several CCDs are employed.

Figure 6.8 shows three examples of instantaneous SLIPI images of an optically dilute flow of water droplets obtained using the high-speed SLIPI setup. Also included is a magnification of each measurement, to emphasize differences in image details between SLIPI and conventional laser sheet imaging. In the two bottom measurements, an inner flow of nitrogen was added in the center, thus producing a droplet-free region where a zero intensity is expected. However, despite the low level of turbidity ($OD \approx 0.5$, i.e. in the single scattering regime), the contribution of multiply scattered light is clearly seen in this region. Note that in the bottom image, two additional nebulizers have been added in front of the camera to produce a cloud of droplets to (for illustrative purposes) increase the level of multiple scattering. This leads to a noticeable aureole of light blurring the image.

Image Contrast Improvements

In Paper II the improvements in image quality, and thus the effectiveness of multiple light scattering suppression, was quantified by evaluating the contrast in intensity between the induced droplet-free region and the surrounding scattering volume according to

$$C = \frac{I_{max} - I_{min}}{I_{max} + I_{min}} \tag{6.2}$$

where I_{max} and I_{min} represents the average intensity in the surrounding volume and the droplet-free region, respectively. Complete suppression of the multiply scattered
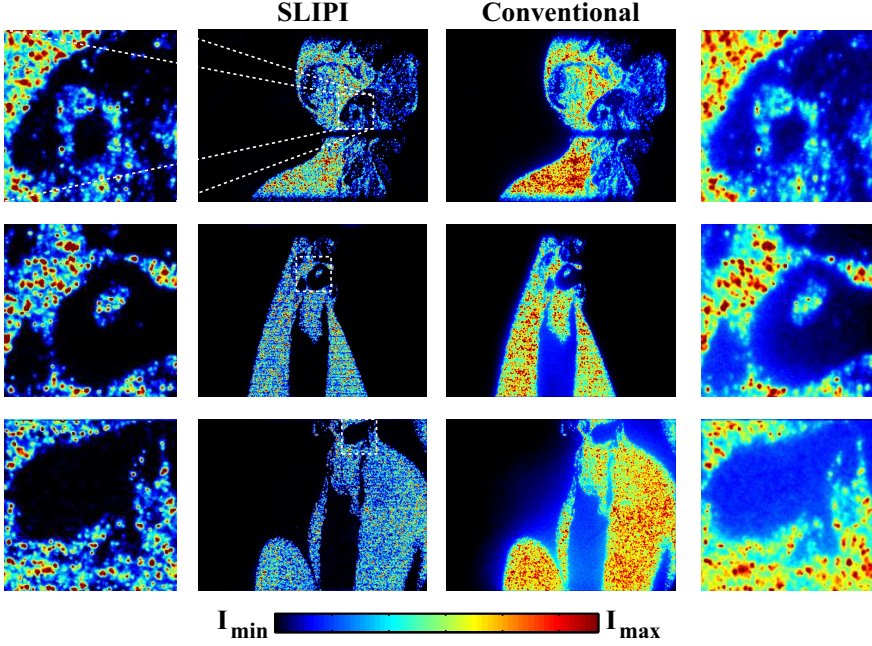
SLIPI   **Conventional**

I_{min} ▬▬▬▬▬ I_{max}

Figure 6.8: *"Single-shot" SLIPI images of a dilute flow of water droplets generated by a nebulizer. In the two bottom cases a flow of nitrogen was added in the center, with the purpose of creating a droplet-free region, from which no light should originate. A magnified area is also provided for each measurement to emphasize differences in image details. Each image has been histogram normalized.*

light thus leads to a contrast close to unity. With no additional nebulizers situated in front of the camera, the value of C was approximately 0.75 and 0.95 for conventional and SLIPI imaging, respectively. An increase in multiple scattering and signal attenuation reduced the contrast for conventional imaging to ∼0.6 whereas the SLIPI cases were only marginally affected ($C \approx 0.93$).

The detection of diffuse light leads to a reduction of image gradients. This is illustrated in Fig. 6.9, where edge-detection[3] is performed on a small region of interest (ROI) with the aim to determine the location of the boundary between the droplet-free and the droplet region. Three different intensity thresholds were used in this analysis and were selected by first determining an "optimal" intensity threshold I_{opt}. In short, I_{opt} was determined by altering the threshold followed by an edge-detection routine. The threshold value giving rise to the lowest number of edges was set as I_{opt}[4]. The location of the boundary was then evaluated by applying an intensity threshold of $I_{opt}/2$, I_{opt} and $2I_{opt}$, corresponding to the gray, yellow and white line in Fig. 6.9, respectively. The result demonstrates how the implementation of SLIPI leads to sharper image gradients and thus, less sensitive to the threshold value.

---

[3]Performed using the "canny" edge-detection routine in Matlab©.

[4]A low threshold gives rise to a large number of edges due to low intensity (background) noise. A similar increase in number of edges occur when the threshold is set too high.
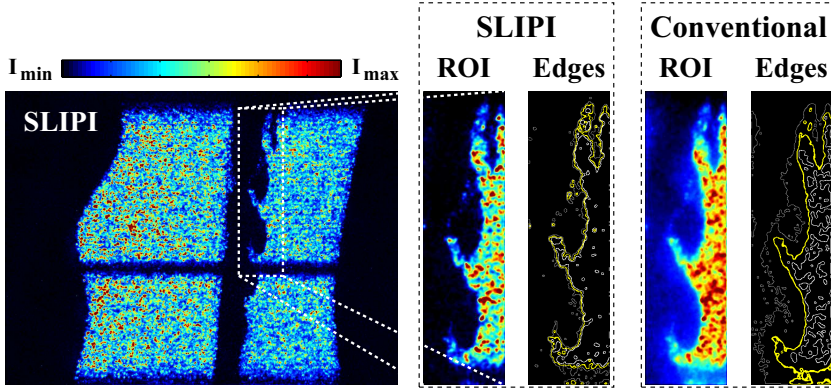
Figure 6.9: *Demonstration of the improvement in image gradients when applying "single-shot" SLIPI. The different line colors indicate the estimated boundary between the nitrogen and the droplet region for different intensity thresholds, where gray = $I_{opt}/2$, yellow = I_{opt} and white = $2I_{opt}$. In the SLIPI case the edges are almost completely overlapped.*

6.3.2 Nanosecond SLIPI System

To obtain "single-shot" SLIPI images of high-pressure spray systems, free from ghosting and without sacrificing spatial resolution, the three modulated images must be recorded within a few hundreds of nanoseconds. Because the time-separation between consecutive laser pulses of a double-pulsed Nd:YAG laser must be kept above 25 μs, an experimental solution based on such a system is not sufficient for the task at hand.

Paper IV describes a SLIPI system capable of acquiring the three laser sheet images within less than 50 ns, allowing droplet velocities of $\sim$600 m/s to be frozen in time (as previously mentioned, this also depends on the spatial resolution). A specially designed "multi-YAG" system, consisting of four individual Q-switched, flash lamp-pumped Nd:YAG lasers (pulse duration $\sim$10 ns) was incorporated to reduce the time-separation between pulses. The system was originally designated for high-speed imaging of turbulent flows as it, when running in double-pulsed mode, provides a rapid burst of up to eight spatially overlapped pulses with time-separations as short as 6.25 μs between consecutive pulses. Since the lasers are individual, the delay between the pulses can be set arbitrarily from 0 to 100 ms when running in single-pulsed mode.

The original design of the multi-YAG system incorporates frequency doubling crystals to spatially overlap the beams. Unfortunately this approach involves nonlinear processes and is therefore not suitable for SLIPI as it would lead to a distortion of the sinusoidal pattern. Instead, three of the four available beams were each sent through an individual Ronchi grating (with the correct spatial phase) and spatially overlapped by means of two beam-splitters, with either 50% or 67% transmission, respectively. Compared to beam-overlapping using frequency doubling, this approach unfortunately introduce significant energy losses ($\sim$67% of the initial energy). The optical arrangement is illustrated in Fig. 6.10.

Each individual Ronchi grating was mounted on a translation stage and moved so the distance to the measurement region was equal for all three components. This was

essential to avoid errors in the image reconstruction procedure. The spatial phase of each beam was adjusted by tilting a glass platelet (thickness 0.5 mm), situated directly after each Ronchi grating. To align the three beams, all recombination optics (the prisms and beam-splitters) were mounted on translational- and rotational stages and the overlapping was monitored both in the near-field and in the far-field (at a distance of ~8 m).
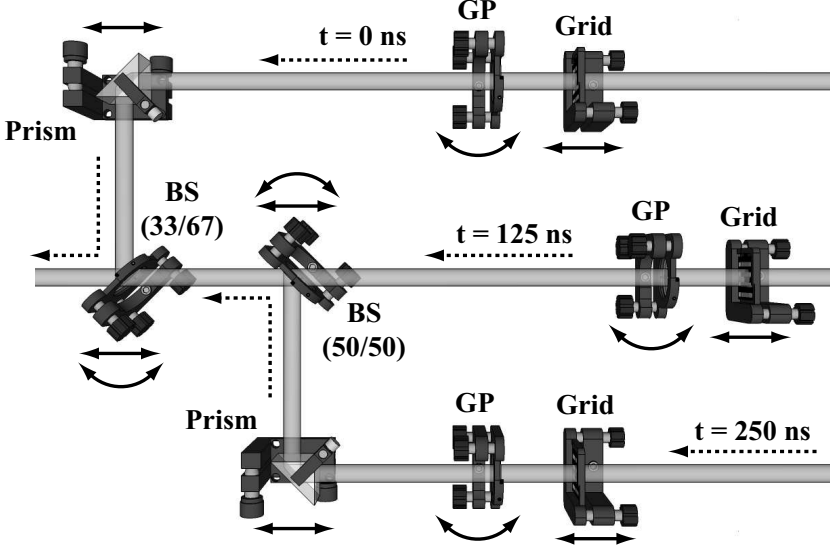

Figure 6.10: *Schematic of the beam overlapping arrangement for the nanosecond "single-shot" SLIPI setup. GP = glass plate, BS = beam-splitter.*

Figures 6.11 illustrates some examples of "single-shot" images acquired using the so-called nanosecond system of a hollow-cone spray (entrance side only), recorded with an inlet pressure of 40 bar. The images denoted "Multiple scattering" corresponds to the intensity being removed in the SLIPI process. These are included primarily to illustrate the non-uniform intensity thresholding carried out by SLIPI. Distinct black dots are visible in these images, indicating that the light originating from such a region is composed mainly of singly scattered light.
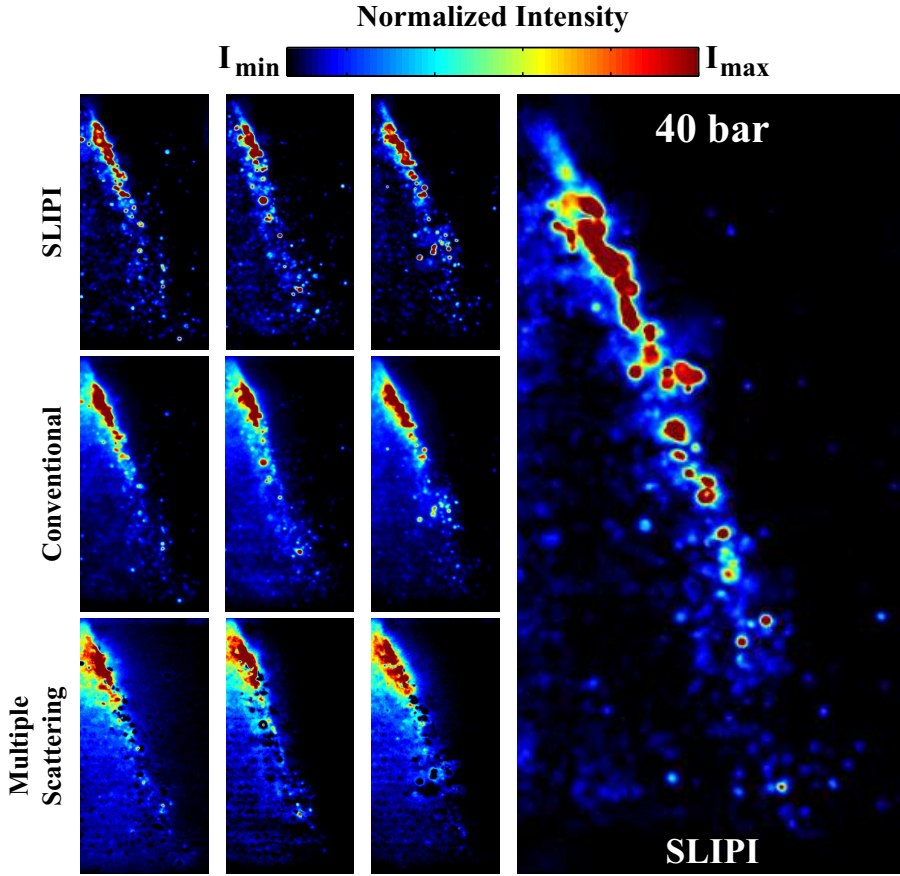
Figure 6.11: *"Single-shot" images of a hollow-cone water spray, where the injected liquid was pressurized to 40 bar. The smaller images show three SLIPI and conventional planar laser imaging "single-shot" images, together with the respective contribution of multiply scattered light. Each image has been histogram normalized.*

6.4 Dual-SLIPI

6.4.1 Background

The dual-SLIPI technique was developed primarily to overcome the two remaining sources of error for laser sheet imaging that is not accounted for with SLIPI, namely laser extinction and signal attenuation. The main concept of dual-SLIPI is to measure the extinction coefficient spatially resolved in 2D. If measured correctly, this will produce a quantitative description of the sample where each pixel element reveals the local reduction of light intensity. This value is, in turn, coupled to the product between the number density of droplets and their sizes, as described in Chapter 3. Even though the extinction coefficient is not uniquely set[5], it provides a comparable

---

[5]Different droplet compositions can have equal extinction coefficients.

description of the illuminated sample which is independent of factors such as laser power, intensity profile, detection sensitivity, collection optics *etc.* In addition, no dye or tracer compound is needed since μ_e is an intrinsic optical property. These qualities makes the extinction coefficient one of the most vital optical properties in spray diagnostics. In addition, if the measurement of μ_e is combined with a sizing technique number density can extracted and *vice versa.*

Alternative experimental approaches to measure μ_e can be found in the literature. Wang *et al.* employed time-gated transillumination detection to deduce the line-of-sight integrated extinction [82]. In this study the authors emphasized how the rejection of multiply scattered light improves the measurement accuracy. Ansmann *et al.* utilized Raman LIDAR to determine the extinction of light in the atmosphere, providing results spatially resolved in one dimension [83]. More recently, Lim *et al.* performed tomographic imaging on a turbulent spray, allowing the local extinction coefficient to be calculated in two dimensions [84].

Unlike these alternative solutions, dual-SLIPI aims at determining the extinction coefficient spatially resolved in 2D solely by means of side-scattering detection. A second uniqueness regards the implementation of SLIPI, thus actively accounting for multiple light scattering, which, if detected, will lead to an underestimation of μ_e.

6.4.2 Principle

To explain the principle of dual-SLIPI, consider the arrangement provided in Fig. 6.12, wherein a structured laser sheet is traversing the sample along a given z-position. Two (ideally identical) cameras, positioned at either $z = 0$ or $z = L$, simultaneously view the scattered light from two opposite sides.
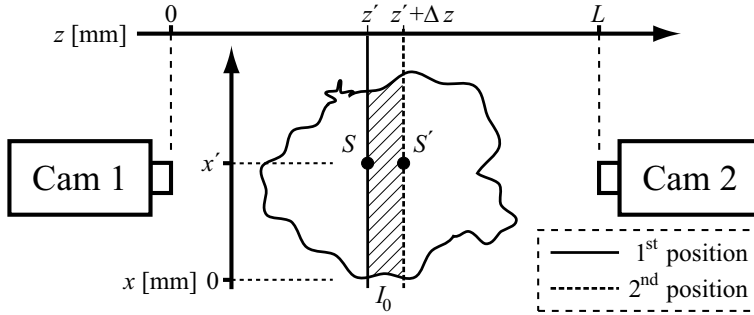

Figure 6.12: *Schematic of the detection arrangement for dual-SLIPI. The dashed region between the two laser sheets indicates the probed volume over which the average extinction coefficient is calculated. The laser enters from below.*

The singly scattered light detected with the first camera at an arbitrary point $(x = x')$ along the initial direction of the laser pulse (positioned at $z = z'$) can be written

$$I_1^1(x', y') = \quad C_1 \cdot S(x', y', z') \cdot I_0(y') \cdot \underbrace{\exp\left(-\int_0^{x'} \mu_e(x, y', z')dx\right)}_{\text{Laser extinction}} \cdot$$

$$\underbrace{\exp\left(-\int_0^{z'} \mu_e(x', y', z)dz\right)}_{\text{Signal attenuation}} \tag{6.3}$$

where C_1 includes detection parameters such as solid angle of collection, detection sensitivity, lens properties *etc.*, S is the three-dimensional source function and I_0 is the one-dimensional incident laser intensity profile. A similar description for the second camera can be made:

$$I_2^1(x', y') = \quad C_2 \cdot S(x', y', z') \cdot I_0(y') \cdot \exp\left(-\int_0^{x'} \mu_e(x, y', z')dx\right) \cdot$$

$$\exp\left(-\int_{z'}^{L} \mu_e(x', y', z)dz\right) \tag{6.4}$$

where the subscript in C differentiates between the different cameras, which may have somewhat different characteristics. The subscript and superscript in I indicate either camera and recording number, respectively. Note that the two expressions are identical, apart from a change in integration limits and eventual differences in C. Thus, by extracting the ratio of the images, the unknown intensity profile, sample function and intensity losses due to laser extinction cancel, giving Eq. 6.5.

$$\frac{I_1^1}{I_2^1} = \frac{C_1 \cdot \exp\left(-\int_0^{z'} \mu_e(x', y', z)dz\right)}{C_2 \cdot \exp\left(-\int_{z'}^{L} \mu_e(x', y', z)dz\right)} \tag{6.5}$$

The procedure is then repeated but with the structured laser sheet displaced Δz mm, leading to the following expression for camera 1

$$I_1^2(x', y') = C_1 \cdot S(x', y', z' + \Delta z) \cdot I_0(y') \cdot \exp\left(-\int_0^{x'} \mu_e(x, y', z' + \Delta z)dx\right) \cdot$$

$$\exp\left(-\int_0^{z' + \Delta z} \mu_e(x', y', z)dz\right) \tag{6.6}$$

and for camera 2

$$I_2^2(x', y') = C_2 \cdot S(x', y', z' + \Delta z) \cdot I_0(y') \cdot \exp\left(-\int_0^{x'} \mu_e(x, y', z' + \Delta z)dx\right) \cdot$$

$$\exp\left(-\int_{z'+\Delta z}^{L} \mu_e(x', y', z)dz\right) \tag{6.7}$$

Once again the ratio of the two expressions cancel most of the unknowns, leading to

$$\frac{I_1^2}{I_2^2} = \frac{C_1 \cdot \exp\left(-\int_0^{z'+\Delta z} \mu_e(x', y', z)dz\right)}{C_2 \cdot \exp\left(-\int_{z'+\Delta z}^{L} \mu_e(x', y', z)dz\right)} \tag{6.8}$$

The exponential term in the numerator in Eq. 6.8 can be rewritten as the product of two exponential terms according to

$$\frac{I_1^2}{I_2^2} = \frac{C_1 \cdot \exp\left(-\int_0^{z'} \mu_e(x', y', z)dz\right) \exp\left(-\int_{z'}^{z'+\Delta z} \mu_e(x', y', z)dz\right)}{C_2 \cdot \exp\left(-\int_{z'+\Delta z}^{L} \mu_e(x', y', z)dz\right)} \tag{6.9}$$

In a similar fashion the denominator in Eq. 6.5 can be rewritten as

$$\frac{I_1^1}{I_2^1} = \frac{C_1 \cdot \exp\left(-\int_0^{z'} \mu_e(x', y', z)dz\right)}{C_2 \cdot \exp\left(-\int_{z'}^{z'+\Delta z} \mu_e(x', y', z)dz\right) \exp\left(-\int_{z'+\Delta z}^{L} \mu_e(x', y', z)dz\right)} \tag{6.10}$$

From these mathematical descriptions the purpose of the experimental approach becomes clear. Almost all remaining unknowns can be canceled by dividing Eq. 6.10 with Eq. 6.9, leaving only the term describing the exponential reduction of light intensity as photons travel the distance Δz, according to

$$\frac{I_1^1 \cdot I_2^2}{I_2^1 \cdot I_1^2} = \exp\left(2 \cdot \int_{z'}^{z'+\Delta z} \mu_e(x', y', z)dz\right) \tag{6.11}$$

from which the average extinction coefficient over Δz can be derived, giving Eq. 6.12.

$$\bar{\mu}_e(x', y') = \ln\left(\frac{I_1^1(x', y') \cdot I_2^2(x', y')}{I_2^1(x', y') \cdot I_1^2(x', y')}\right) \cdot \frac{1}{2\Delta z} \tag{6.12}$$

To summarize, by performing two SLIPI measurements, separated Δz mm, and simultaneously recording the scattered light from two opposite sides the approach

allows the average extinction coefficient to be extracted in 2D. Unlike other experimental approaches designed to measure μ_e, the dual-SLIPI method takes advantage of signal attenuation to gain quantitative information. The lateral spatial resolution of the system depends on the collection optics and the number of pixels, whereas the depth-resolution is set by Δz.

Figure 6.13 shows an example of the method, where for example the symmetry of the spray is revealed in the resulting dual-SLIPI image. Also noticeable is how the procedure removes non-uniformities present in the incident laser sheet intensity profile.
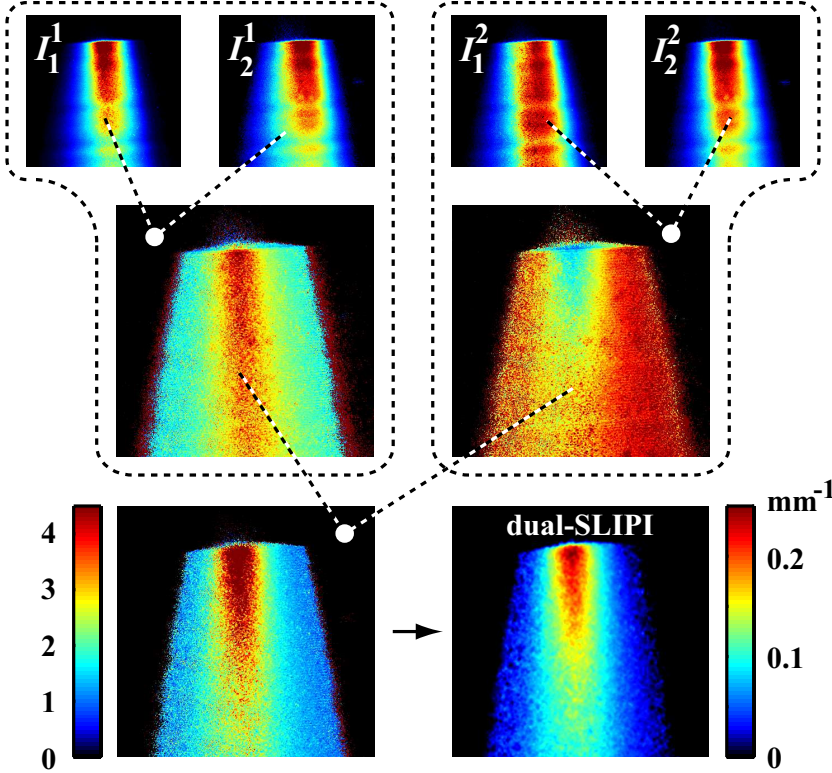

Figure 6.13: ***Top row****: The four required SLIPI images.* ***Middle row****: Ratio between SLIPI images, Eqs. 6.9 and 6.10.* ***Bottom row:*** *Image resulting from Eq. 6.11 and the final dual-SLIPI image. Note that the dual-SLIPI image has been low-pass filtered to reduce high frequency noise.*

6.4.3   Limitations

The validity of the derivations in Eqs. 6.3-6.12 relies on a number of assumptions. Firstly, the implementation of the Beer-Lambert law is only valid for the singly scattered light intensity. Consequently, if the SLIPI approach is unable to fully diminish the multiply scattered light, the calculated μ_e will be underestimated. Secondly, the detection scheme assumes light to be detected at ± 90 degrees only. To achieve this,

a small detection acceptance angle must be employed (or, alternatively, spatial filtering) which reduces the collected signal. Thirdly, the light scattering properties must be identical at +90 and -90 degrees, making dual-SLIPI unsuitable for measurements in the spray formation region due to the presence of non-spherical liquid ligaments. Finally, due to the use of two cameras, exact pixel-to-pixel overlapping is essential.

The dual-SLIPI method has one important prerequisite which should be addressed; the approach relies on the presence of scatterers in the two probed sections. In fact, these sections serve merely as a means to gain knowledge about the distribution of attenuators in-between them. This implies that no such information can be obtained if one (or both) of the image pair lacks scatterers at a given position. For example, a void, sufficiently small to only appear in I_1^1 and I_2^1 but not in the second image pair, would lead to an evaluated extinction of being negligible or infinitely large.

As the extinction coefficient is obtained by taking the logarithm of an image ratio, the method becomes very noise-sensitive. In addition, the level of uncertainty for the evaluated μ_e increases with distance, as illustrated in Fig. 6.14, due to the exponential loss of the singly scattered light. In the example in Fig. 6.14 a homogeneous sample is probed, having an average extinction coefficient of 0.15 mm^{-1} and a physical dimension of 10×10 mm^2. The optical depth of the sample is thus 1.5, i.e. classified as optically dense. Three different scenarios are provided, where the noise level is gradually increased. $I_0 = 1$ in all cases and the depth-resolution is set constant at $\Delta z = 3$ mm. The noticeable effects are; (1) the apparent growth of noise in the evaluated extinction coefficient with distance and (2) the sensitivity to the added noise level. This example demonstrates the need for good S/N, which unfortunately seldom accompanies a measurement performed on a turbid scattering medium.
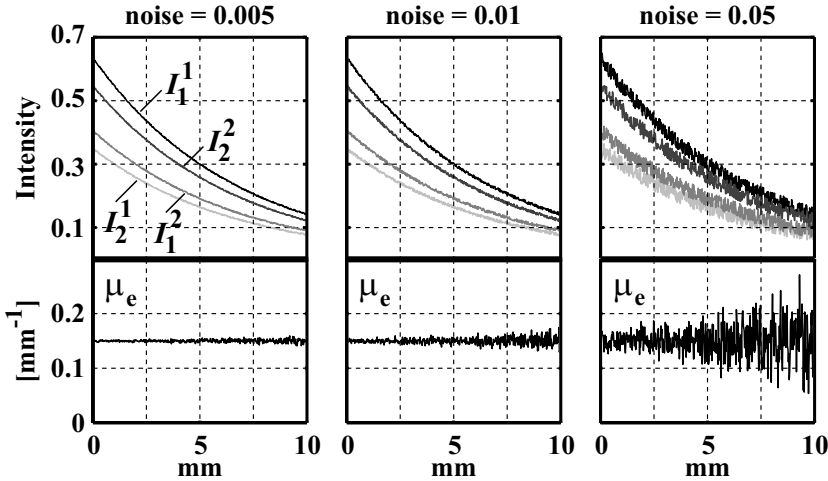

Figure 6.14: *A homogeneous sample with an OD of 1.5 and the physical dimension 10×10 mm^2. The sample is probed at $z = 3$ mm (I_1^1, I_2^1) and $z = 6$ mm (I_1^2, I_2^2). The added noise (uniform distribution) simulates different measurement conditions.*

Mitigation of the noise can be achieved by increasing the distance between the two laser sheets, as illustrated in Fig. 6.15. In this example Δz is altered from 1 to

6 mm, leading to a reduction of the noise level but at the cost of depth-resolution. The added noise level is set to 0.025 for all cases.
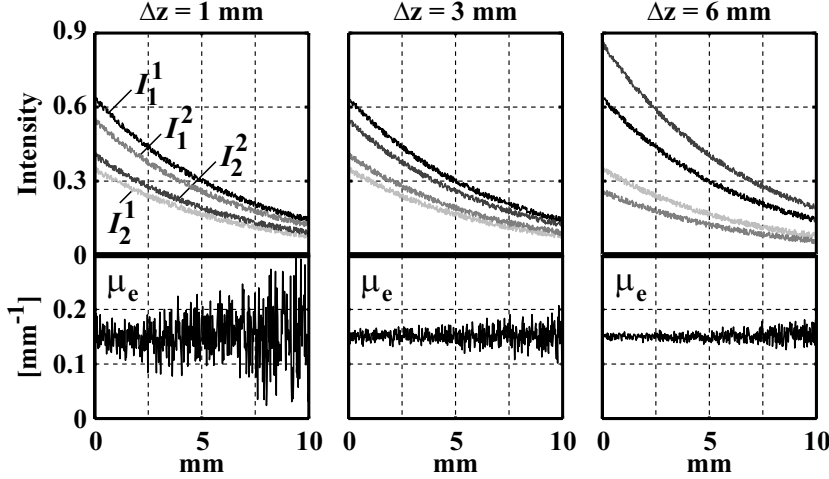

Figure 6.15: *The influence of Δz, illustrated on the same homogeneous sample as in Fig. 6.14. The added noise is set constant to 0.025.*

Another factor affecting the noise in a dual-SLIPI measurement is the value of the extinction coefficient. Although the technique relies on extinction and is therefore not suitable for optically dilute samples, a too high μ_e leads to a poor S/N and, consequently, noisy results. This is illustrated in Fig. 6.16, where three differently turbid homogeneous samples are probed. In the example the noise level is set constant to 0.005 and Δz fixed at 3 mm.
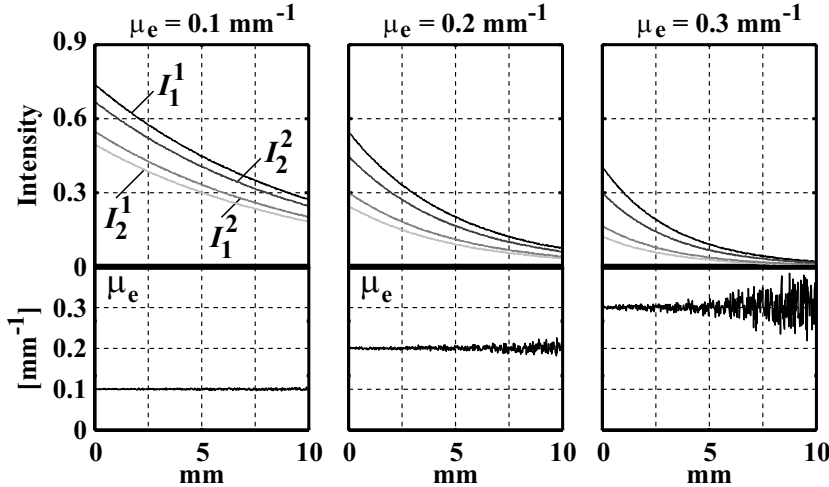

Figure 6.16: *The influence of the turbidity, illustrated for three different μ_e. The noise level is set constant to 0.005 and the depth-resolution at 3 mm for all cases.*

6.4.4 Pixel-to-pixel Overlapping Routine

Due to non-perfect alignments the field-of-view for the individual cameras will be slightly different, which, in effect, renders errors in the dual-SLIPI process. To overcome this issue, geometrical transformation can be implemented, a procedure which relocates the different image elements to a common reference coordinate system. This can be achieved in various ways, one common approach is to image a target consisting of vertical and horizontal grid lines and to mark each intersection manually. This will provide a 2D map of reference points that subsequently can be used as input to a geometrical transformation routine. This approach was utilized in Paper II and IV. The drawback with the method is the difficulty of automatizing the procedure. For the results presented in Paper VI, an alternative (automated) approach was implemented, where the an image target consisting of dots was used instead. The different steps of the procedure are exemplified in Fig. 6.17.
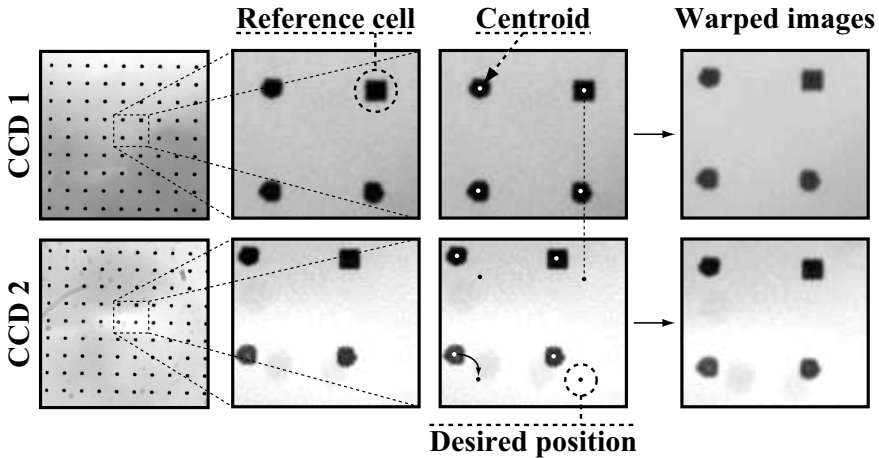

Figure 6.17: *Pixel-to-pixel overlapping procedure. A dotted pattern is imaged by both cameras. A computer program locates the centroids of each dot, thus providing a 2D map of reference points which are used as input to a geometrical transformation algorithm.*

In short, a dot-pattern was printed onto a transparent slide[6] and imaged by both cameras, the result of which is shown on the left-hand side in Fig. 6.17. The initial misalignment is apparent in the two leftmost magnified regions. An image processing routine then calculates the centroid (geometric center) of each dot, thus providing a 2D map of reference points for each CCD and used as input to the geometrical transformation algorithm. Due to the large number of reference points available, high order polynomial functions can be implemented to correct for the displacement of the image elements. For severe misalignments it is recommended to add a "reference cell" in the target, as shown in Fig. 6.17.

---

[6]The use of a transparent slide is needed as the two cameras are positioned on either side of the sample.

6.4.5 Results

The capability of the dual-SLIPI technique was investigated on two different atomizing air-assisted spray systems; one solid cone spray and one 6-hole injector. The results are provided in Fig. 6.18 for three values of Δz. Also included in the figure is a measurement performed on a homogeneous mixture of non-absorbing polystyrene spheres ($\varnothing = 0.5$ μm). For comparison, the corresponding images obtained using conventional laser sheet imaging and SLIPI are also provided. Noise-reduction by means of low-pass filtering is performed on the dual-SLIPI images, at the cost of lateral resolution.

These results illustrate both the advantages and the disadvantages with dual-SLIPI. As apparent in Fig. 6.18, the main limitation of the technique is the depth-resolution, which is inferior to both conventional laser sheet imaging and SLIPI. Reducing Δz renders noisy and less trustworthy results. Hence, the technique should therefore only be employed when a relatively poor depth-resolution is acceptable. However, unlike most other existing measurement techniques, dual-SLIPI provides quantitative 2D data, corrected for laser extinction, signal attenuation and multiple light scattering, and it is applicable for inhomogeneous turbid scattering and absorbing media, given that a three-way optical access is available. Furthermore, no calibration is required and the technique can be applied directly to the central region of the sample.

Figure 6.19 shows dual-SLIPI images of a diesel spray, together with the corresponding SLIPI and conventional images (recorded simultaneously). Figure 6.20 illustrates an additional benefit with quantitative imaging. The figure shows two measurements performed on an air-assisted solid cone water spray but at two different downstream locations. By merging the two images into one, a larger FOV is achieved.
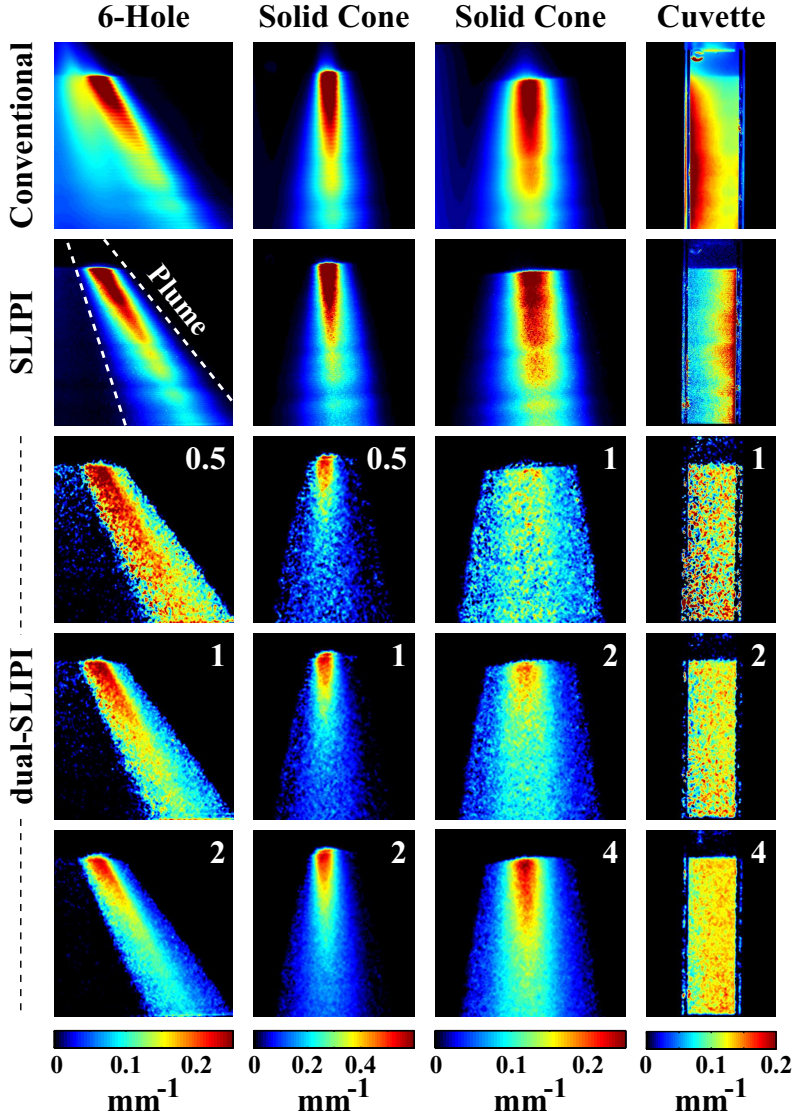
Figure 6.18: *Images obtained using either conventional planar laser imaging, SLIPI or dual-SLIPI. **Left column:** One spray plume from a 6-hole injector. **Middle columns:** Solid cone spray, acquired either 11 mm (left) or 23 mm (right) from the nozzle outlet. **Right column:** Homogeneous sample. The numbers given in the dual-SLIPI images indicate Δz in mm. In all cases the laser sheet approached the medium from the right.*
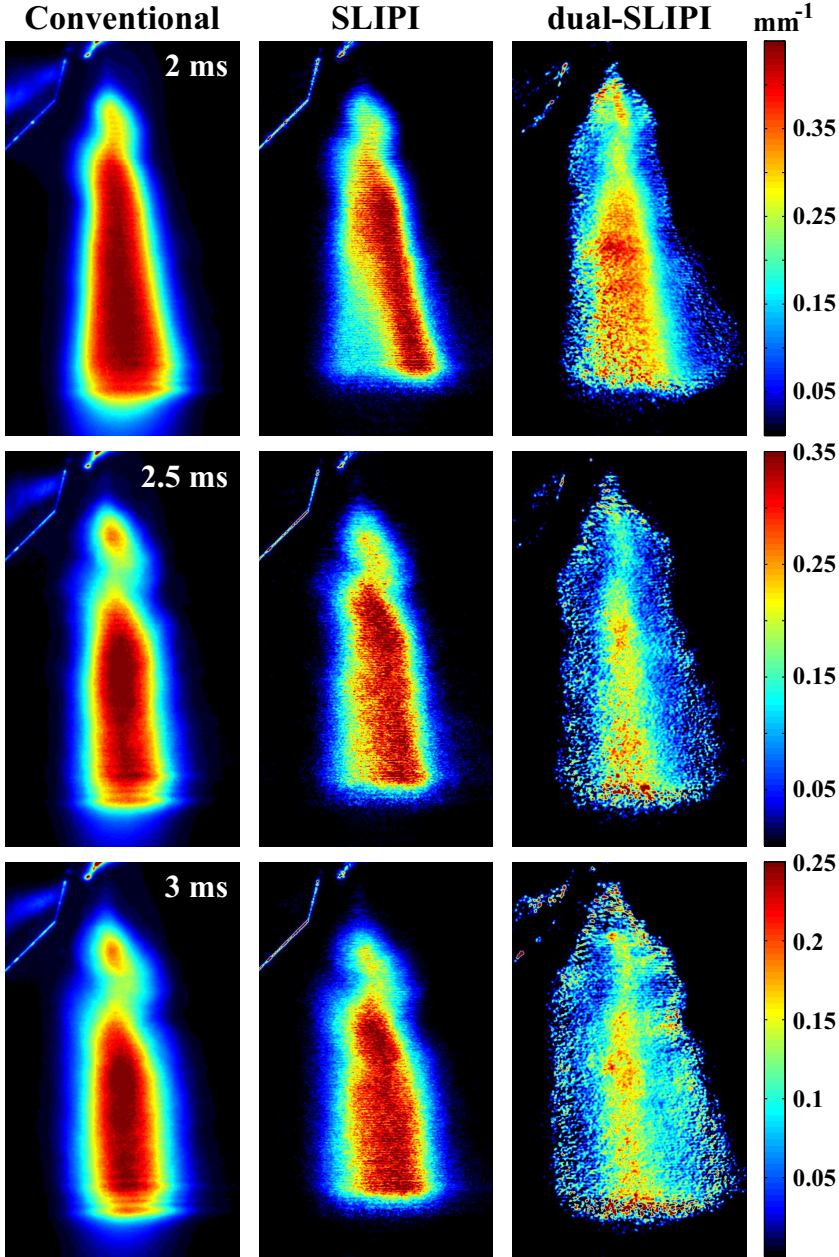
Figure 6.19: *Dual-SLIPI applied on a diesel spray ($\Delta z = 2$ mm). The numbers in the upper right corners indicate the time after SOI.*
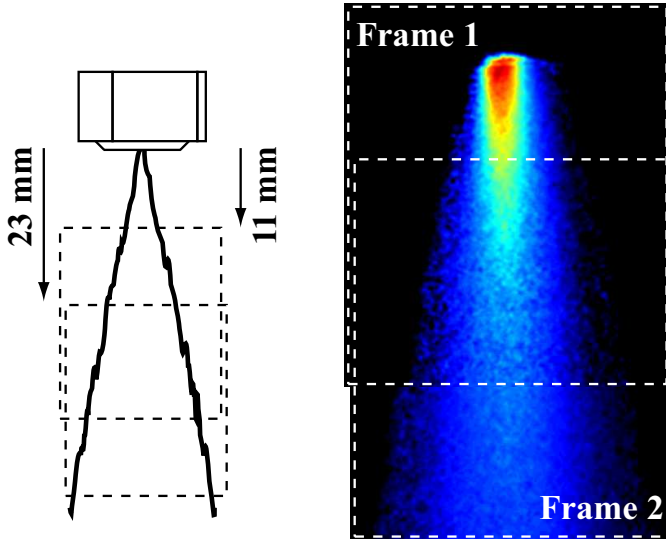
Figure 6.20: *Two dual-SLIPI images, acquired at 11 mm and 23 mm from the nozzle orifice. Due to the quantitative nature of the acquired data, the images can be merged into one, thus increasing the field-of-view.*

6.5   SLIPI-Scan

6.5.1   Introduction

The SLIPI-scan technique[7] presented in Paper VIII provides means to measure the extinction coefficient spatially resolved in three dimensions without the limited depth-resolution associated with dual-SLIPI. The technique, which is based on SLIPI, was inspired by the work performed by Koh *et al.* [85] and Inagaki *et al.* [86]. The essential idea, common for the techniques presented by these authors as well as for SLIPI-scan, is to probe the sample in a "bread slicing" manner, see Fig. 6.21. This can be performed by mounting the sample on a translational stage. With this approach, intensity reductions caused by signal attenuation can be estimated and accounted for by examining each individual slice, starting with the one at the very border. This particular slice is unique in the sense that signal attenuation effects are negligible here. Under these conditions it is possible to calculate the local extinction coefficient if the scattered light and the path-integrated attenuation are measured simultaneously. One prerequisite for the validity of this calculation is that the scattered light intensity must scale in accordance with the extinction, which is true for spherical scattering and absorbing objects[8] and if signal attenuation effects are either negligible or have been compensated for.

With knowledge of the extinction coefficients in the first slice, signal attenuation in the adjacent slice can be compensated for, once again allowing the calculations of μ_e. The procedure is repeated for all deeper-lying slices, resulting in a 3D matrix of the extinction coefficient.

---

[7]Note that the experimental approach is not referred to as SLIPI-scan in Paper VIII.

[8]The technique does not apply for purely absorbing object, the extinction of light must be partly due to scattering.
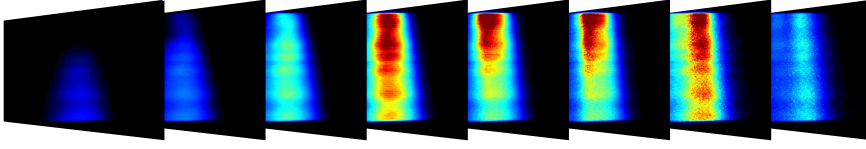
Figure 6.21: *"Bread-slicing" approach used in the SLIPI-scan. By traversing the sample, different sections are probed.*

6.5.2 Experimental Procedure

Carrying out the SLIPI scanning procedure is experimentally challenging and the full setup requires careful alignment. It is preferable and advised, but not required, to arrange the setup in a way so that each recorded image contains; (1) the scattered light generated as the structured laser sheet propagates through the sample, (2) the transmitted light and (3) a part of the incident beam (representative of the incident laser fluence). Figure 6.22 illustrates such an optimum operating condition, where all these parts are measured using a single camera. Quite naturally, this cannot be achieved for all types of samples. In such scenarios, a two-camera setup must be utilized, one camera designated to record the scattered light, the other to monitor the incident laser fluence as well as the transmitted light. The laser fluence information is used to normalize each SLIPI measurement, an essential part if the light source exhibits temporal fluctuations. However, if the light source is known to be temporally stable, it is possible, yet not advisable, to exclude this part.
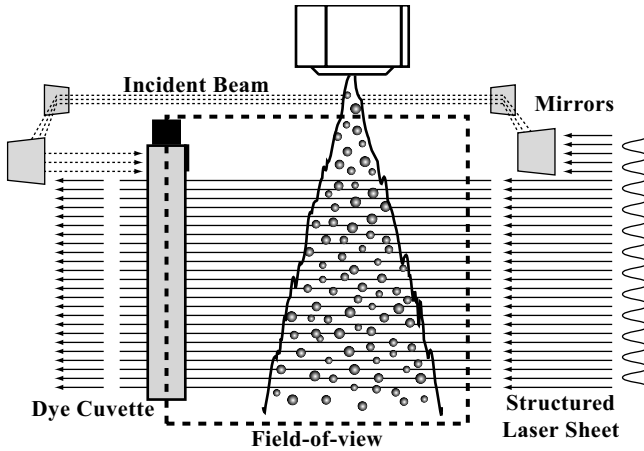

Figure 6.22: *Field-of-view for an optimum SLIPI-scan setup, where the scattered light from the probed sample, the transmitted light as well as a part of the incident beam is visualized within a single frame.*

The transmitted light can be measured using different approaches. The measurements presented in Paper VIII utilized a dye cuvette (DC) situated as near the sample as possible. The cuvette was furthermore used to monitor the laser fluence by rerouting a portion of the laser sheet around the sample, as shown in Fig. 6.22.

A word of caution, when implementing a non-coated glass cuvette to measure the path-integrated attenuation one should be aware that ∼4% of the light incident on its surfaces is reflected, with the risk of illuminating the sample from behind. This will introduce an error in the scattered light intensity and the cuvette must be positioned so that the reflected light passes either in front of or behind the sample. Depending on the level of multiple scattering, the back-reflected light might only be visible in the final SLIPI image.

The extinction coefficients are calculated using an in-house developed algorithm, which, in turn, relies on the Beer-Lambert law. Thus, if the algorithm is to function properly, its input data - the scattered and the transmitted light - must be free from any intensity contribution arising from multiple scattering. It is thus imperative to utilize structured illumination to measure both these quantities.

6.5.3   Data Processing

The input data needed to perform the calculations in 3D are:

I_i: 2D matrix of the incident irradiance

I_f: 2D matrix of the transmitted irrandiance

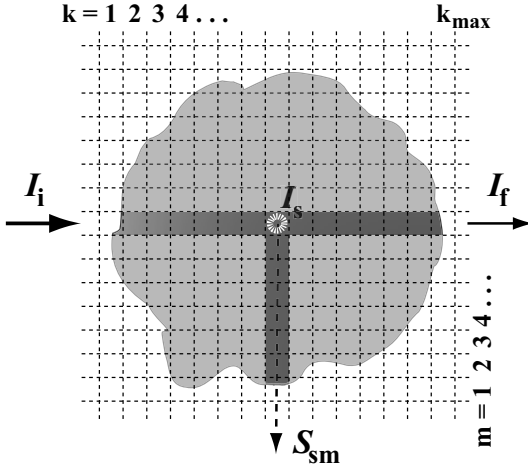S_{sm}: 3D matrix containing the SLIPI measurements

Figure 6.23: *2D scattering sample illuminated with a 1D beam. The scattered light I_s from voxel (k,m) is detected at 90 degrees. When the laser beam is positioned at $m = 1$, signal attenuation is negligible.*

The data processing procedure of the SLIPI-scan technique is mainly composed of two steps; (1) compensation for signal attenuation and (2) calculating the spatially resolved extinction coefficient once signal attenuation is accounted for. To explain the procedure (here in 2D), consider a 2D scattering sample illuminated with a 1D laser beam, see Fig. 6.23. As the light interacts with the sample it generates a signal I_s. A camera positioned at a 90 degree angle can only detect a portion (S_{sm}) of this signal, due to the limited solid angle of collection. The relation between the intensities are given by

$$S_{sm}(k,m) = K_a \cdot I_s(k,m) \cdot (1 - a(k,m)) \tag{6.13}$$

where K_a represents an unknown camera function whose value is given by the solid angle of collection times the camera efficiency. The term $(1 - a(k, m))$ denotes the attenuation of the signal as the light propagates from voxel (k,m) through the scattering medium to the camera. Note that the term represents the light transmission and equals unity if signal attenuation is negligible, i.e. $a = 0$. Under the assumption that light is detected at 90 degrees only, a can be expressed as

$$a(k, m) = 1 - \exp\left(- \sum_{m'=0}^{m-1} \bar{\mu}_e(k, m')dz \right) \tag{6.14}$$

where m equals the axial position (depth) of the laser beam and $\bar{\mu}_e$ is the average extinction coefficient in voxel (k, m').

The camera function in Eq. 6.13 can be determined by estimating factors such as lens properties, quantum efficiency, solid angle of collection *etc.*, yet this approach is questionable as it is likely to introduce errors. A second method to determine K_a, which is a necessity for the SLIPI-scanning technique, is by measuring the incident light intensity I_i and the path-integrated attenuation I_f. The difference between these quantities equals the sum of the scattered and/or absorbed light, according to

$$\sum_{k=1}^{k_{max}} I_s(k, m) = I_i(m) - I_f(m) \tag{6.15}$$

Combining this with Eq. 6.13 leads to the following expression

$$\sum_{k=1}^{k_{max}} \frac{S_{sm}(k, m)}{K_a \cdot (1 - a(k, m))} = I_i(m) - I_f(m) \tag{6.16}$$

Under most conditions K_a can be assumed to be independent of the k-position and can therefore be moved outside the summation, yielding the following expression for K_a

$$K_a = \frac{\sum_{k=1}^{k_{max}} \frac{S_{sm}(k,m)}{(1-a(k,m))}}{I_i(m) - I_f(m)} \tag{6.17}$$

Hence, the ratio between the sum of the signal (divided with the signal attenuation term) and the loss of light equals the previously unknown camera function. One important prerequisite for the validity of this expression is, however, that the entire width of the scattering sample must be visualized. Any loss of light occurring outside the field-of-view of the camera will lead to an inaccurate estimation of K_a.

Finally, substituting K_a in Eq. 6.13 with the expression in Eq. 6.17 leads to the following expression for I_s

$$I_s(k, m) = \frac{S_{sm}(k, m) \cdot (I_i(m) - I_f(m))}{(1 - a(k, m)) \cdot \sum_{k=1}^{k=k_{max}} \frac{S_{sm}(k,m)}{(1-a(k,m))}} \tag{6.18}$$

The only unknown factor in Eq. 6.18 is a. However, by starting the measurements at the very border of the sample (plane nearest the camera), intensity losses due

to signal attenuation can be neglected. Hence, the scattered irradiance I_S can be calculated at $m = 1$ using Eq. 6.18.

The next step in order to calculate the extinction coefficients is to calculate the position-dependent laser irradiance I. This is done by subtracting the irradiance scattered within a voxel ($I_s(k, m)$) from the laser irradiance before it enters that voxel, according to

$$I(k + 1, m) = I(k, m) - I_s(k, m) \tag{6.19}$$

Since the incident irradiance is known, $I(k, 1)$ can be calculated for all values of k. The irradiance before and after each voxel can also be expressed using the Beer-Lambert law:

$$I(k + 1, m) = I(k, m) \cdot \exp\left(-\bar{\mu}_e(k, m)dx\right) \tag{6.20}$$

The extinction coefficient is finally obtained by combining and rearranging Eqs. 6.19 and 6.20, leading to the following expression

$$\bar{\mu}_e(k, m) = -\ln\left(\frac{I(k, m) - I_s(k, m)}{I(k, m)}\right) \cdot \frac{1}{dx} \tag{6.21}$$

When probing the $m = 2$ plane, intensity reductions caused by signal attenuation can no longer be neglected. However, knowing $\bar{\mu}_e(k, 1)$, for all k, allows the term $(1 - a(k, 1))$ to be calculated using Eq. 6.14, after which Eq. 6.18 can be used to calculate $I_s(k, 2)$. This, in turn, enables the calculations of the position-dependent extinction coefficients. The procedure is then repeated for each position m until $\bar{\mu}_e$ has been extracted for all probed sections.

Note that even though Eqs. 6.13-6.21 were derived here in two dimensions only, the concept is easily transferable to three dimensions. For the full derivation in three dimensions, see Paper VIII.

An example of the different steps of the SLIPI-scanning procedure is provided in Fig. 6.24. In the leftmost graph the true distribution of μ_e is shown together with I_s, calculated using Eq. 6.18. Notice how the measured intensity distribution appears to be shifted towards the entrance (left) side, a consequence of laser extinction. By applying Eq. 6.19, the irradiance before and after each voxel is extracted (middle graph). Finally, the position-dependent extinction coefficient is extracted by means of Eq. 6.21 (rightmost graph).
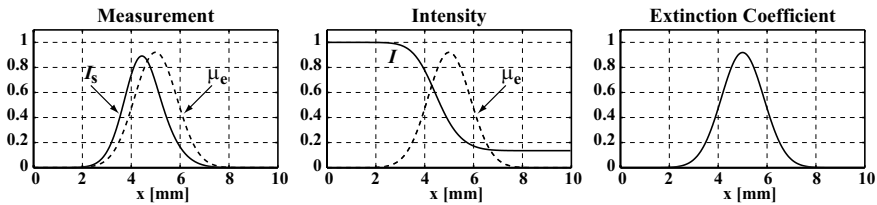

Figure 6.24: *The calculative steps for the determination of $\bar{\mu}_e$, here demonstrated in the absence of signal attenuation. **Left:** I_s calculated using Eq. 6.18. **Middle:** The position-dependent laser irradiance I, calculated according to Eq. 6.19. **Right:** The resulting $\bar{\mu}_e$, calculated using Eq. 6.21.*

6.5.4 Limitations

The theoretical approach given in Eqs. 6.13-6.21 relies on the full suppression of the multiply scattered light in both S_{sm} as well as in I_f (I_i, which is measured without the presence of the sample, is assumed to be free from errors due to multiple light scattering). Incomplete rejection of this undesired contribution of light intensity will lead to an underestimation of the extinction coefficients. Figure 6.25 illustrates such a scenario, where the path-integrated attenuation is erroneously measured. In the top graphs the measured optical depth is 20% lower than the true value, while the error is increased to 35% in the lower graphs. From these plots it can be observed how an error in the evaluated OD leads to an underestimation of $\bar{\mu}_e$. The consequence of this is particularly severe for the accuracy of SLIPI-scan as it will affect the compensation for signal attenuation in the consecutive layers. For more information regarding this problem and advisable means of remediation, see Paper VIII.
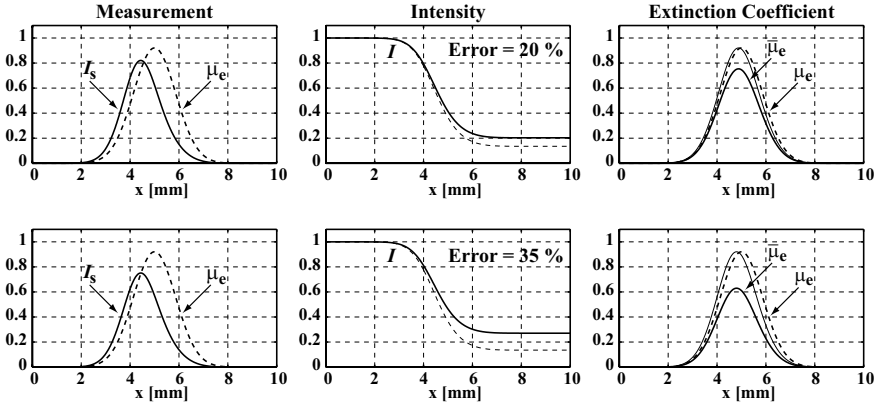

Figure 6.25: *Error in the calculated values of $\bar{\mu}_e$ due to an erroneously measured OD.* **Top row:** *OD 20% lower than the true value.* **Bottom row:** *OD 35% lower than the true value. The thin solid line in the rightmost graphs shows the normalized (evaluated) $\bar{\mu}_e$ curve, where it can be noticed how the peak position is slightly shifted towards the entrance side.*

6.5.5 Results

Before applying the SLIPI-scanning technique its performance was tested on a homogeneous sample. In this case, the evaluated extinction coefficient should not vary over the probed volume. The sample consisted of a glass cuvette containing a homogeneous mixture of distilled water and 0.5 μm monodisperse and non-absorbing polystyrene microspheres. 16 SLIPI measurements were conducted in total, each separated $\Delta z = 500$ μm. Figure 6.26 shows a comparison between the resulting images acquired using either SLIPI, conventional planar laser imaging or SLIPI-scan. To more easily view and compare the results the intensity values in each image have been averaged along the vertical axis.

The intensity reductions caused by laser extinction and signal attenuation are easily detectable in the SLIPI results (laser enters from the left), that shows an exponential decay of intensity both along the x- and the z-axis. The slope of these
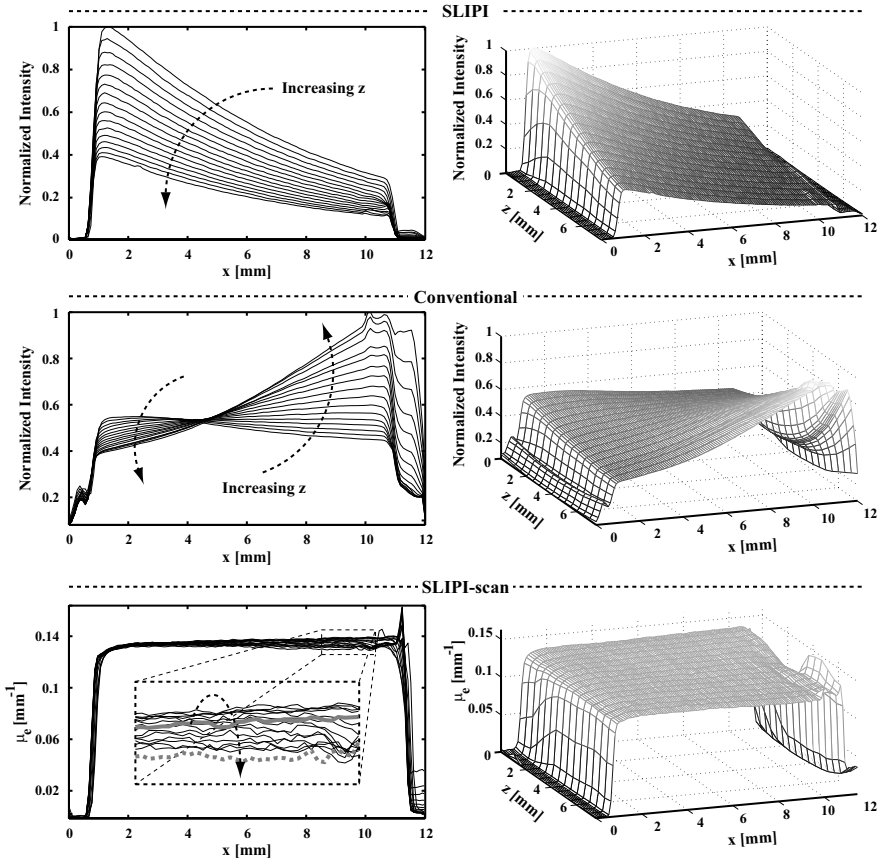
Figure 6.26: *Comparison between SLIPI, conventional planar laser imaging and SLIPI-scan, here applied on a homogeneous medium. The graphs in the left column shows the (vertically averaged) intensity curves for 16 measurements. The right column shows a 3D view of the same curves. The plane at $z = 0$ mm correspond to the one nearest the camera.*

curves holds information regarding the average extinction coefficient and was, by means of curve fitting routines, found to be 0.132 mm^{-1}.

The results obtained with conventional planar laser imaging shows a strange, yet consistent, trend. At $x < 4.5$ mm the intensity decreases with increasing z, a sign of signal attenuation. The trend is inverted at $x > 4.5$ mm, indicating that the amount of multiply scattered light being detected is increasing with z. However, perhaps most striking is that all curves coincide at $x = 4.5$ mm. Regardless of the underlying reason for this unpredictable result, it is obvious from these trends that applying the SLIPI-scan methodology on this non-decaying conventional PLI dataset would yield erroneous results (see demonstration in Paper VIII).

Applying SLIPI-scan leads to a direct visualization of the sample homogeneity, with an average extinction coefficient of 0.134 mm^{-1} and a standard deviation of 0.017 mm^{-1} and is thus in agreement with the extinction coefficient extrapolated from the curve fitting routine. However, even though the implementation of SLIPI-scan leads

to significant improvements, the resulting curves, which should be identical, show some discrepancies. Firstly one can notice the slight dispersion of the curves with increasing x. Secondly, there seems to be a systematic trend in the evaluated μ_e (see inset), where the values first increase and then decrease as deeper-lying sections are probed (indicated with the dashed arrow in the inset). To differentiate between the measurements the μ_e corresponding to $z = 0$ is marked as a thick solid gray line, whereas the deepest probed layer is shown as a thick dashed gray line. The reason for this trend is probably associated with a non-complete rejection of the multiply scattered light, yet this needs to be further investigated.
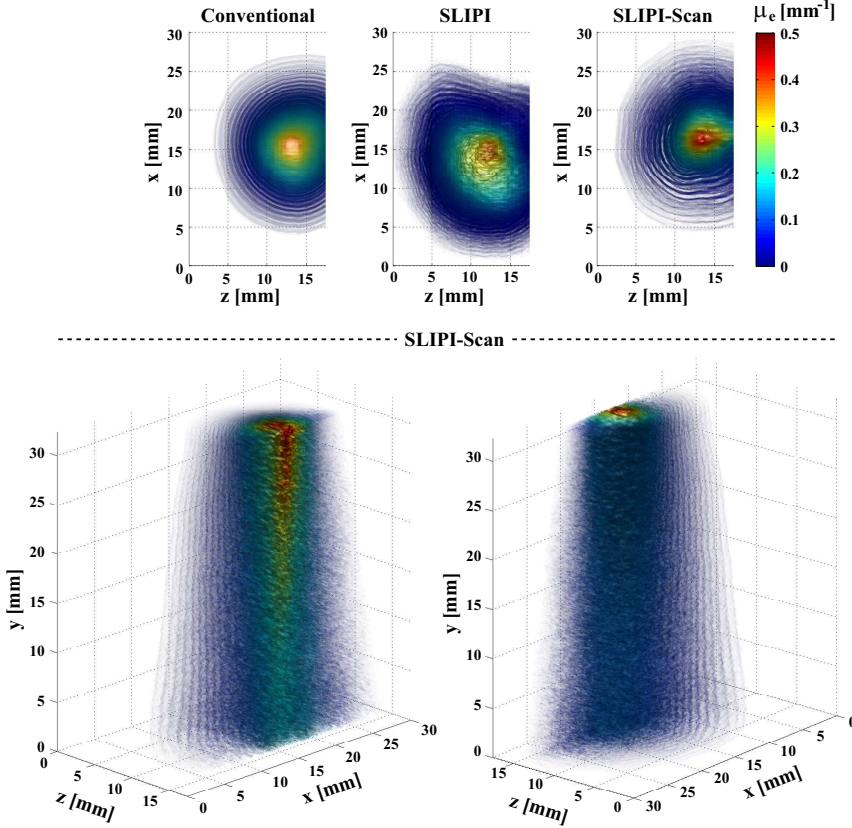

Figure 6.27: ***Top row:*** *Images of the conventional, SLIPI and extinction coefficient (viewed from above). The symmetric spray structure seen in the conventional image is due to the detection of multiply scattered light, counteracting attenuating effects. Removal of this erroneous light leads to an asymmetric spray structure. By calculating the local extinction coefficient by means of SLIPI-scan restores the symmetry.* ***Bottom row:*** *3D representations of the extinction coefficient, covering a spray volume of $30 \times 33 \times 14.5$ mm^3.*

The top row in Fig. 6.27 shows the results (viewed from above) when applying the three different techniques on an air-assisted solid cone water spray, 23 mm below the nozzle tip. At this distance and with the operating conditions employed, the light transmission reached a minimum of 5%, corresponding to an OD of 3. The 3D

renditions were created by plotting semi-transparent isosurfaces with values ranging from 5% to 90% of the maximum signal in each case. With the level of turbidity being more than twice that of the cuvette measurement, laser extinction and signal attenuation is expected to significantly influence the SLIPI results, whereas the conventional case should, on top of these two sources of error, be affected also by multiple light scattering.

The result obtained when applying conventional planar laser imaging shows an almost perfectly symmetric spray structure. This contradictory result is due to the detection of diffuse light, which counteracts attenuation. When filtering out this undesired contribution of intensity by means of SLIPI the effect of signal attenuation and laser extinction becomes clearly visible, and the result shows an asymmetric spray structure. Thus, the fact that the symmetry is preserved in the conventional data is not a guarantee that attenuating effects are negligible. Calculating the extinction coefficient by applying the SLIPI-scanning algorithms on the SLIPI data restores the spray symmetry but with a shape that is different from the one based on the conventional data. For a more detailed comparison between the different approaches see Paper VIII.

6.6 Computed Tomographic Imaging

6.6.1 Background

The discovery that X-rays penetrate human tissue lead to the development of several instruments dedicated for medical applications. Computed tomographic (CT) imaging constitutes the culmination of this endeavor. By recording a set of X-ray transmission measurements combined with a reconstruction algorithm, this technique provides means to visualize (in two or three dimensions) the contents of a non-transparent objects interior. With the progress made since the first successful measurement in the early 1970's, CT is nowadays a vital tool for medical nosology [87].
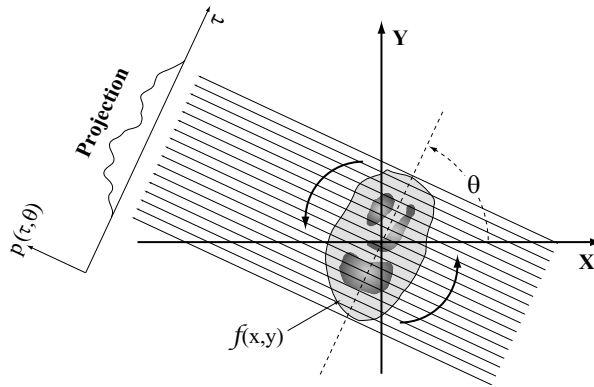

Figure 6.28: *Example of parallel-beam projection.*

Computed tomographic imaging is based on solving the inverse *Radon transform*, which consists of a certain number N of *projections* acquired at different viewing an-

gles θ. A "projection" is a set of line integrals, see Fig. 6.28, and the different incident angles are achieved by either rotating the object itself or the source-detector arrangement. This set of data, which is an incomplete sampling of the Radon transform, is commonly referred to as a *sinogram*[9]. The sinogram bears information regarding the spatial distribution of the attenuators inside the object. The aim of CT is to extract this information by performing an inverse Radon transform and thereby reconstructing the sample quantitatively, in either two or three dimensions. Achieving this end can be accomplished by various algorithmic means.
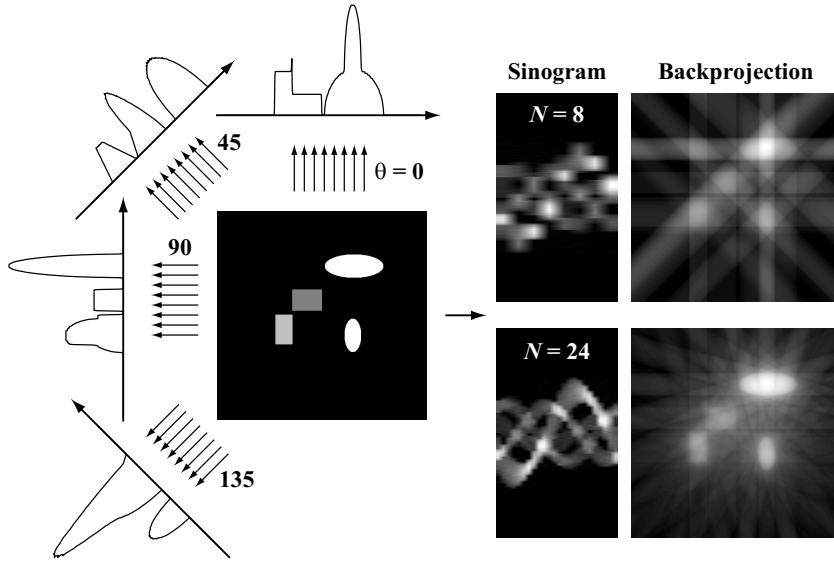

Figure 6.29: *Principle for simple backprojection.*

Perhaps the most straightforward reconstruction method is called *simple backprojection*. In practice, this approach is seldom employed as it leads to blurry unsatisfactory results, yet it illustrates the basic idea behind CT well. The elementary operation for simple backprojection is to "smear" each projection in the reverse direction from which it was originally acquired. The final image is formed by taking the sum of all the backprojected views. Figure 6.29 illustrates the principle for either eight or 24 viewing angles.

The crude reconstructions of the sample in Fig. 6.29 demonstrate the need for a large number of viewing angles. As seen, undersampling leads to inaccurate results with unacceptable image artefacts. This is a general concern for CT and not only for simple backprojection. The examples in the top row in Fig. 6.30 shows how the number of samplings affects a backprojected sample reconstruction (original object same as in Fig. 6.29). The apparent blurring noticeable when N is sufficient (case $N = 360$) is an undesired characteristic feature for simple backprojection and is the reason why the method is avoided. The bottom row in Fig. 6.30 illustrates the progression of the "smearing" process, where the backprojection routine was

---

[9]The name stems from the fact that a fixed point in the object will trace a sinusoidal path in the projection space.

interrupted after 10, 30, 80 or 120 projections. In the two first cases (10 and 30 viewing angles), the structure of probed object can hardly be seen, yet as the number of projections included in the reconstruction process increase beyond a certain limit, the four isolated attenuators starts to become visible.
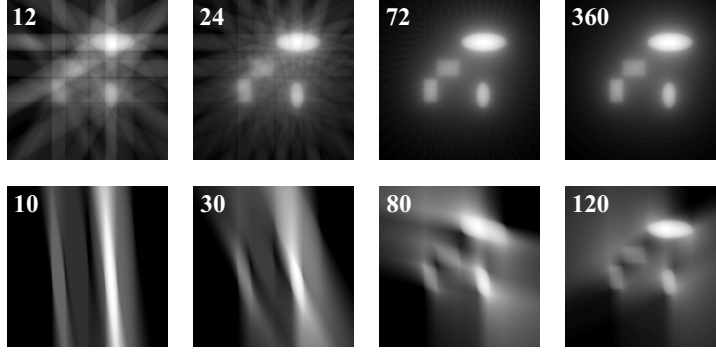

Figure 6.30: *Top row: A larger number of viewing angles reduces the appearance of image artefacts. The number of incident angles are specified in each backprojected image. **Bottom row**: The progression of simple backprojection. The reconstruction has been interrupted after 10, 30, 80 and 120 projections (total of 180 angles). All examples were constructed from the sample shown in Fig. 6.29.*

Filtered-backprojection (FBP) is a technique to remedy the blurring encountered in simple backprojection. With this approach, each projection is convoluted with a one-dimensional filter kernel prior to being back-projected. Figure 6.31 illustrates the difference between the two methods. Notice how the blurring is avoided when using the filtered approach. This technique was used for the results presented in Paper IX.
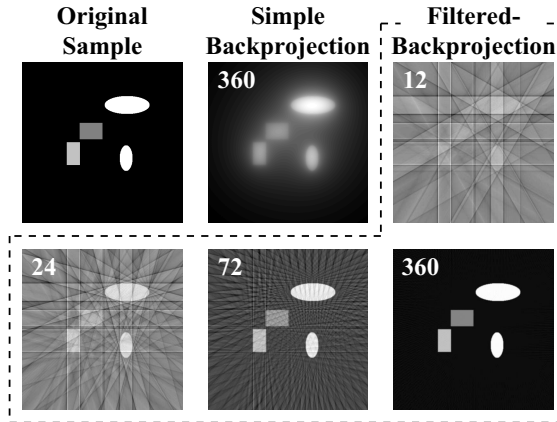

Figure 6.31: *Difference between simple- and filtered-backprojection.*

6.6.2 Tomography and Structured Illumination

Computed tomographic imaging relies on accurate transmission readings, free from multiple light scattering intensity contributions. From an optical diagnostic point of view, X-rays are perfectly suited for almost all CT applications due to their weak interaction with matter. This property is also beneficial for spray studies, not only for CT but also to enable visualization of the interior of the nozzle during operation [88–90]. However, compared to visible laser sources, X-rays are impractical, hazardous, complex and expensive, making the use of X-ray based techniques less wide-spread in the field of spray research.

To enable accurate CT measurements on optically dense or thick media by means of visible light, the problem regarding multiple light scattering must be addressed. This was the aim of Paper IX where transmission imaging based on structured illumination was combined with computed tomography[10]. In addition, a slightly different illumination scheme named "crossed"-SLITI (crossed-Structured Laser Illumination Transmission Imaging) was implemented in this study. Instead of modulating the intensity in one direction only, crossed-SLITI utilizes both vertical and horizontal modulation, with the purpose to improve the filtering capabilities of SI even further[11]. The approach was inspired by the work performed by Lei and Zumbusch, who used a four-faceted glass pyramid to create four beams that, via interference, create an intensity modulation in both the x- and y-direction [91]. However, this approach was avoided in the measurements performed in Paper IX as it leads to undesired residual line structures in the final processed SLITI image.

Figure 6.32 illustrates the optical setup used for the transmission measurements in Paper IX. Two laser pulses, slightly separated in time ($\sim$100 ns), each illuminated a Ronchi grating after which the beams were spatially overlapped using a beam-splitter component, which, unfortunately, leads to a loss of 50% of the energy. To modulate the beams both vertically and horizontally, the gratings were rotated 90 degrees relative each other. A second negative aspect (besides the losses introduced by the beam-splitter) with this approach compared to the four-faceted glass pyramid is that the Ronchi grating generates unwanted spatial frequencies that must be rejected. This was accomplished by focusing the laser pulses onto a so-called frequency cutter (schematically illustrated in Fig. 6.32), permitting only the $\pm 1^{\text{st}}$ orders of diffraction. With this approach, each laser pulse is thus divided in two beams, which, with distance, overlap and create (via interference) the desired intensity modulation. However, with the two original laser pulses being separated in time, they do no interfere, thereby avoiding the issue with the approach presented by Lei and Zumbusch. Finally, the beams were guided through the sample, which was mounted on a rotational stage, and onto a screen which was imaged by a camera. By setting the acquisition time sufficiently long the camera recorded the sum of the two pulses.

This optical arrangement renders some complications. Firstly, the demodulation process requires nine subimages to be recorded, thus tripling the acquisition time. Secondly, the incident light source is slightly divergent, which can lead to errors in the CT reconstruction procedure. Unfortunately, the most favorable condition, which

---

[10]Paper V, which is a pre-study to Paper IX and VIII, also investigates the possibility to reduce errors induced by multiple light scattering for transmission imaging.

[11]Note that the potential improvements regarding the multiple light scattering suppression capabilities with this illumination scheme is yet to be investigated.
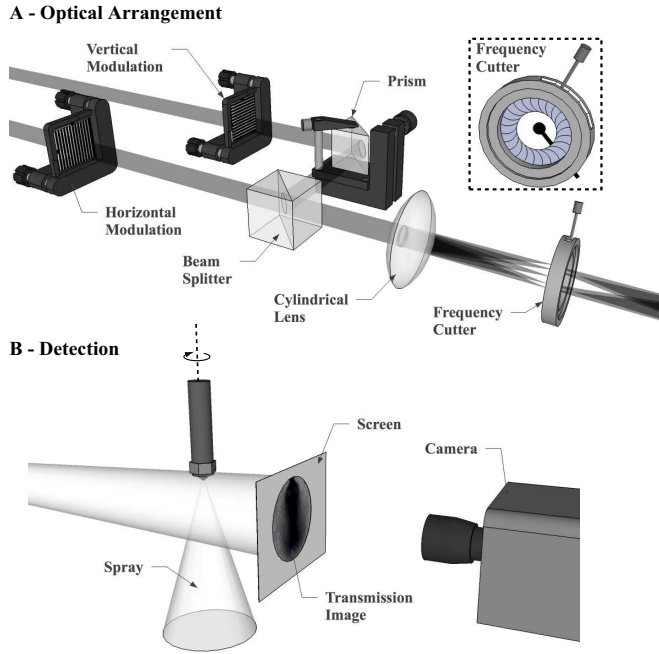
A - Optical Arrangement

B - Detection

Figure 6.32: *A: Optical arrangement for the crossed-SLITI setup. Two laser pulses, slightly separated in time, each illuminate a Ronchi grating (oppositely orientated). A frequency cutter device physically blocks higher harmonics generated by the Ronchi gratings. **B**: The doubly modulated light is sent through the spray, which is mounted on a rotational stage. The transmitted light is then imaged as it falls onto a screen.*

requires the least complex calculations, *parallel-beam projection*, cannot be achieved with SI[12]. To reduce these potential errors the angle of divergence was chosen as low as possible (~ 1.5 degrees). By computer simulating the chosen optical scheme it could be deduced that this would not cause any significant errors in the sample reconstruction, see Fig. 6.33. Naturally, the use of more sophisticated reconstruction algorithms will increase the level of accuracy, however, this was beyond the scope of Paper IX.
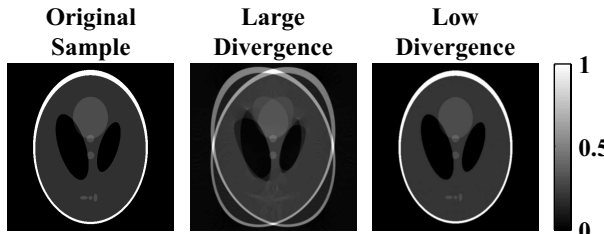
Original Sample **Large Divergence** **Low Divergence**

Figure 6.33: *Errors in the sample reconstruction procedure due to a divergent illumination. The rightmost case corresponds to the measurement conditions used in Paper IX.*

---

[12]There are, as always, exceptions. Choi *et al.* demonstrated a tomographic imaging instrument with parallel-beam projection, capable of measuring the index of refraction in 3D based on structured illumination [92]. The technique is, however, only suitable for optically dilute media.

A second motivation for using the crossed-SLITI approach concerns the presence of residual lines structures (this topic is discussed in more detail in the following chapter). These fringes are created in the required demodulation process and can be detected (if not visually) in the Fourier transform of the final SI-image. Figure 6.34 illustrates the difference between the crossed-SI approach used in Paper IX and traditional SI, the former being nearly completely free from such undesired image artefacts. This feature will have a greater impact for applications where the incident modulation must, for various reasons, be made coarser, as this will bring any accompanying residual lines towards lower - more easily visible - frequencies. Also included is a transmission measurement performed on a neutral density filter using the approach presented by Lei and Zumbusch, which, as seen, leads to unacceptable residual line structures both along the x- and y-axis.
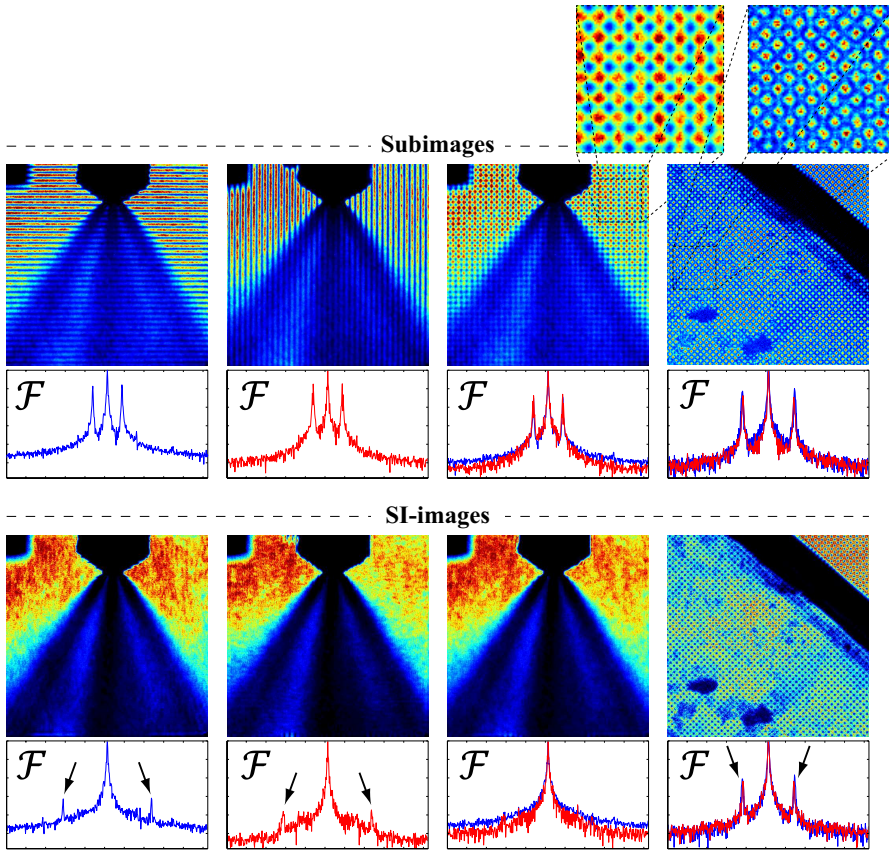

Figure 6.34: *Comparison between vertical (left), horizontal (second from the left), crossed intensity modulation using either two laser beams (second from the right) or one laser beam (right). The corresponding Fourier transform (logarithmic scale) is provided below each subimage (red = horizontal cross section, blue = vertical). The approach presented by Lei and Zumbusch leads to both vertical and horizontal residual line structures. Traditional SI (two leftmost cases) reduces the amount of residuals, yet these do not completely disappear. The crossed-SLITI approach shows no sign of residuals. The arrows in Fourier transform graphs indicate the residual lines.*

6.6.3 Validation

To determine whether the crossed-SLITI approach is suitable for tomography, its performance was investigated by quantitatively measuring the response of the system. The evaluation process, which was repeated six times, comprised probing a turbid sample (cuvette), in which the level of turbidity was increased in a controlled fashion. This was achieved by mixing various amounts of water with a scattering (milky) solution, thereby altering the number density of scatterers and, in effect, the optical depth. According to the Beer-Lambert law (Eq. 3.3) the transmitted light intensity should reduce exponentially with increasing concentration, or, alternatively, the measured OD should increase linearly with number density. The results are provided in Fig. 6.35.
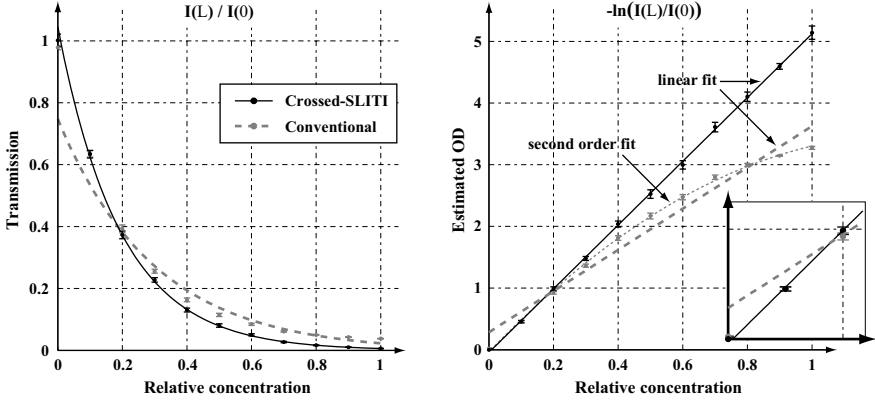

Figure 6.35: *Left graph*: *Ratio $I(L)/I(0)$ as a function of relative concentration. Included in the graph is a single exponential fit.* **Right graph**: *Estimated optical depth as a function of relative concentration, together with linearly fitted curves. A second order polynomial fit, that captures the trend more accurately, is provided for the conventional case. The error bars indicate standard deviation. The inlet shows a magnification of the curves at low OD where it can be noticed that the data points for SLITI and conventional transmission imaging overlap.*

At low concentrations, crossed-SLITI and conventional[13] transmission imaging show similar trends. Hence, in the single scattering regime there is no apparent benefit with crossed-SLITI. However, as the evaluated OD exceeds unity the results starts to diverge and the conventional signal is no longer in accordance with the Beer-Lambert law. This is particularly interesting since $OD = 1$ constitutes the border between the single- and intermediate scattering regimes, thus demonstrating the negative impact multiple light scattering has on conventional imaging techniques and that the errors induced by this extraneous light should not be disregarded. In contrast, the crossed-SLITI intensity continues to decrease exponentially throughout the entire span, thus demonstrating the potential for exceeding this limit by relatively simple and inexpensive means. However, it is important to note that the degree of accuracy still remains uncertain - the linear response with relative concentration does not guarantee accuracy in absolute numbers.

---

[13]As for previous cases, the "conventional" image is calculated with Eq. 5.5.

Figure 6.36 illustrates differences between crossed-SLITI and conventional transmission imaging both qualitatively and quantitatively. In these measurements a solid object was inserted into a cuvette (dimension $34 \times 44 \times 100$ mm^3), containing a mixture of water and milk. The turbidity of the scattering medium was altered using the previous approach[14]. Ideally the intensity should drop to zero as photons are being blocked by the object ("zero region"), providing a contrast in intensity of 100% between the object and its surrounding. However, due to multiple scattering events, photons will falsely appear to be originating from the "zero region", thus leading to a reduced contrast. The numbers labeled C_5, C_3 and C_1 in each image indicate the evaluated contrast over the three different object thicknesses, calculated using Eq. 6.2. Note that all images are histogram normalized, misleadingly improving the visual image contrast. The indicated values are, however, calculated prior to histogram normalization.
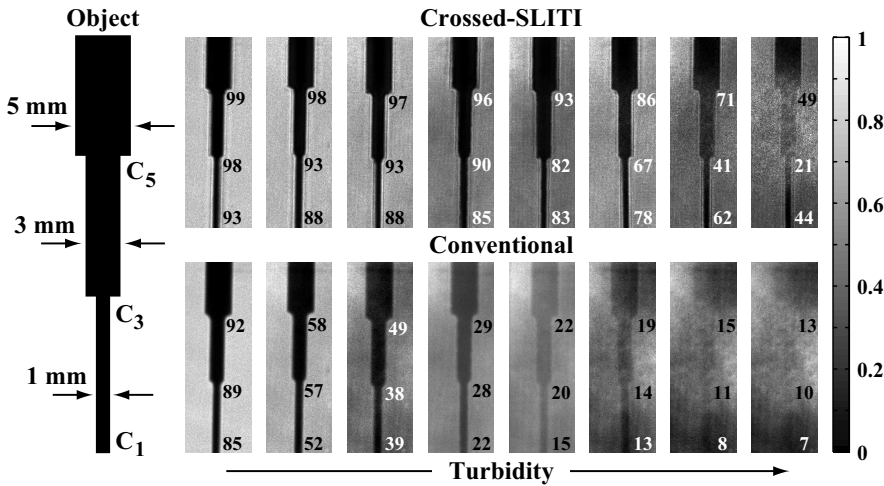

Figure 6.36: *Transmitted light intensity through a cuvette with a mixture of water and milk with incrementally increasing turbidity. The numbers specify the estimated image contrast (Eq. 6.2), measured over the three different thicknesses of the object.*

Similar trends as those seen in Fig. 6.35 can be noticed here. At low milk concentrations the evaluated contrasts are comparable and there is no reason to employ SI. However, as the relative amount of milky substance increases the object becomes blurred, accompanied by a rapid drop in image contrast for the conventional results. As the turbidity reaches its maximum value, the object is almost completely hidden. These results demonstrate how conventional transmission imaging (based on visible light) of optically turbid media is unsuitable for CT as its implementation would lead to a significant underestimation of the extinction coefficient.

---

[14]Note, however, that the incrementation of the level of turbidity is not matched with that in Fig. 6.35.

6.6.4   Results

Crossed-SLITI was applied for 3D tomographic imaging on three different air-assisted atomizing liquid spray systems; a 6-hole water spray run in steady state, a transient iso-octane spray generated by a GDI injector and a steady state solid cone water spray. Figures 6.37-6.39 shows 2D cross-sections of the extinction coefficient extracted from the 3D results at various positions. Being free from any skewness caused by laser extinction or signal attenuation, these images clearly demonstrate the advantages of 3D CT. By computing semi-transparent isosurfaces the results can also be visualized in 3D, see Fig. 6.40-6.42.

Perhaps the main benefit with 3D CT imaging is that it measures a physical quantity that is directly related to the sample itself. Hence, as for dual-SLIPI and SLIPI-scan, there is no need to add any dye or tracer compound, thereby reducing the uncertainties when comparing different measurements and operating conditions. The method is, in principle, applicable for all types of sprays, granted that the optical depth of the sample does not exceed ~6. However, two optical ports are required for the process and the spray must be rotatable, two prerequisites unfortunately restraining the method in many engine-based applications. It is furthermore important to note that due to the presence and high density of irregular liquid ligaments near the orifice of the nozzle, the reduction of the incident light may deviate from the Beer-Lambert law and one should be careful when analyzing the data in this region.

There are a number of factors affecting the reconstruction process that needs to be considered when performing CT measurements. Firstly, sample fluctuations must, under all circumstances, be avoided or averaged out. Secondly, the accuracy of the reconstruction is closely coupled to the number of viewing angles. One benefit with filtered-backprojection is that the data analysis can be initialized directly after the first acquisition, making it possible to judge whether the chosen angular resolution is sufficient at an early stage. If deemed inadequate, one can simply perform complementary measurements. Another issue concerns the rotation of the sample, since the sample must be rotated around its central axis and any vertical or horizontal displacements are essential to avoid. Finally, the crossed-SLITI CT approach is considerably time-consuming, each 3D rendition is the result of approximately 4 hours of data acquisition[15]. Despite the large number of potential sources of error, the reconstructed samples show very few signs of image artefacts.

From the obtained 3D matrices of the extinction coefficient it is possible to artificially extract a 2D map of the path-integrated optical depth which, in turn, can be used to inspect the validity of the reconstruction algorithm. Figure 6.43 shows such a comparison for two different viewing angles (0 and 90 degrees) of the 6-hole water spray. The graphs shows a quantitative comparison between the measured OD and the computer generated OD, which, if the computer algorithm performs accurately, should be identical. Although some discrepancies are noticed, the computer model performs well in reconstructing the probed volume.

---

[15]Traditional SI will reduce the time by a factor of 3 and may therefore be the preferred choice in many cases.
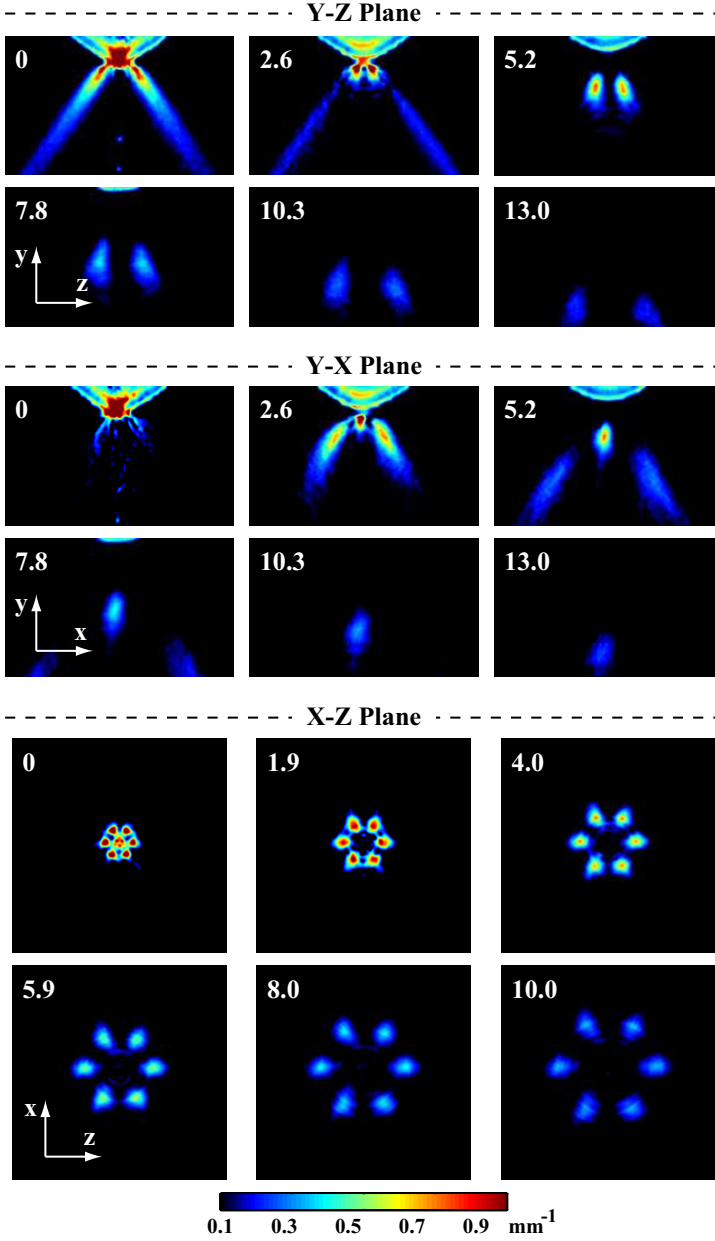
Figure 6.37: *2D views of the 6-hole water spray at different planes. The number indicate the distance (in mm) from the nozzle of the current plane.*
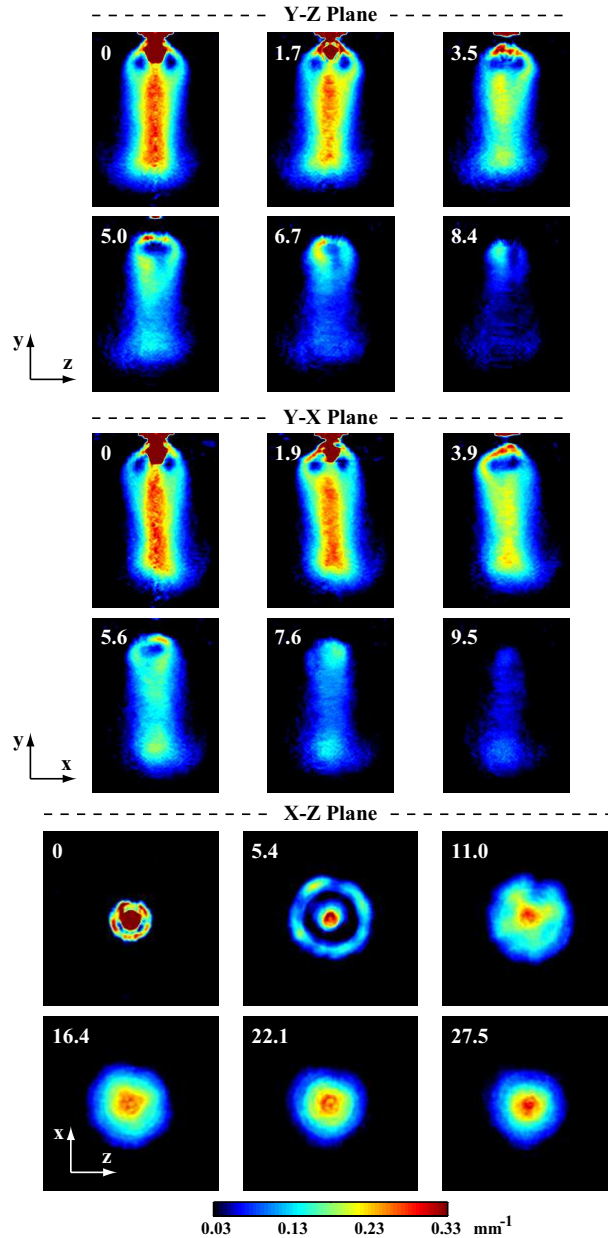
Figure 6.38: *2D views of the GDI spray at different planes. The number indicate the distance (in mm) from the nozzle of the current plane.*
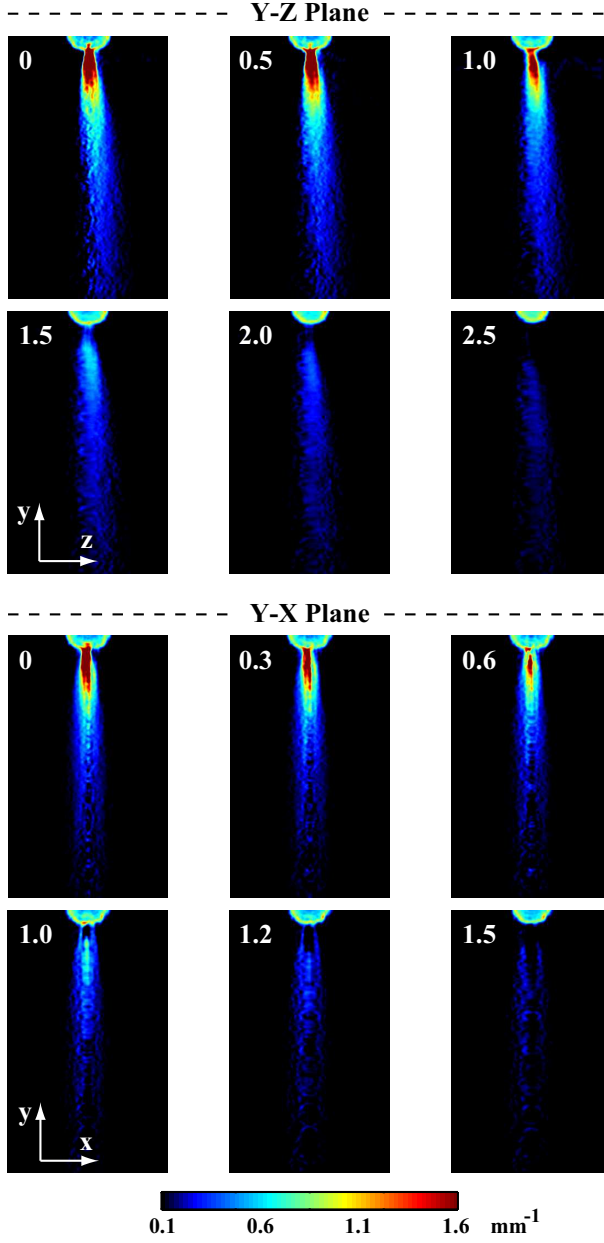
Figure 6.39: *2D views of the solid cone spray at different planes. The number indicate the distance (in mm) from the nozzle of the current plane.*
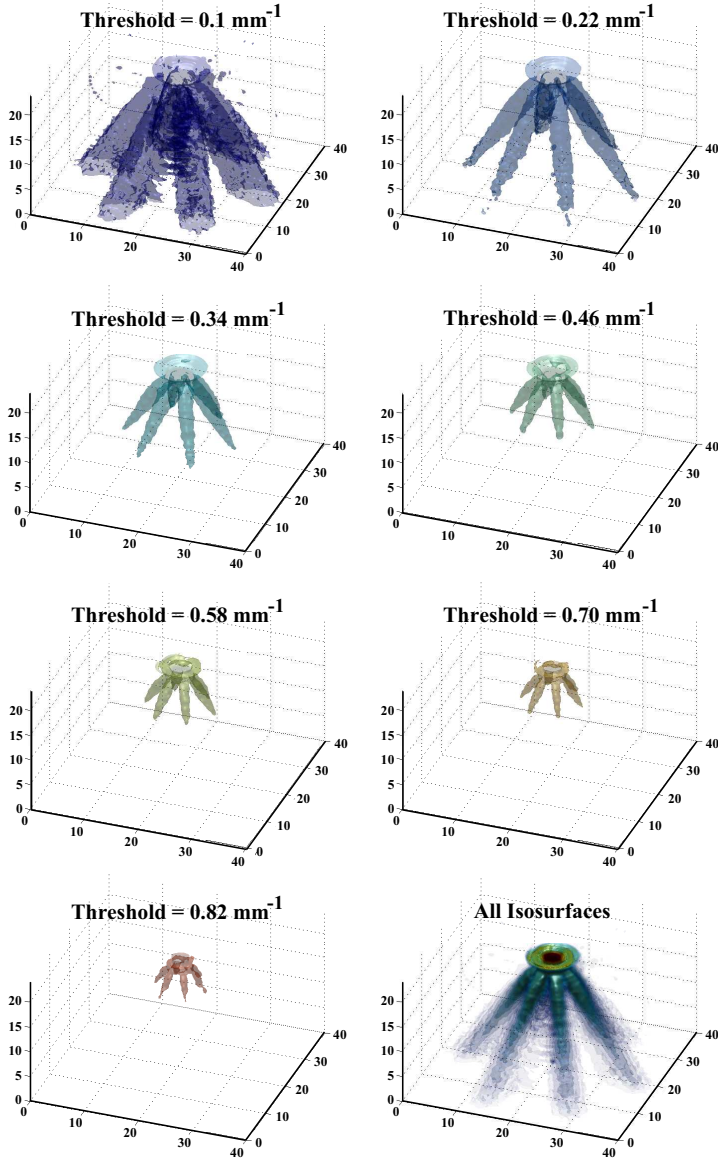
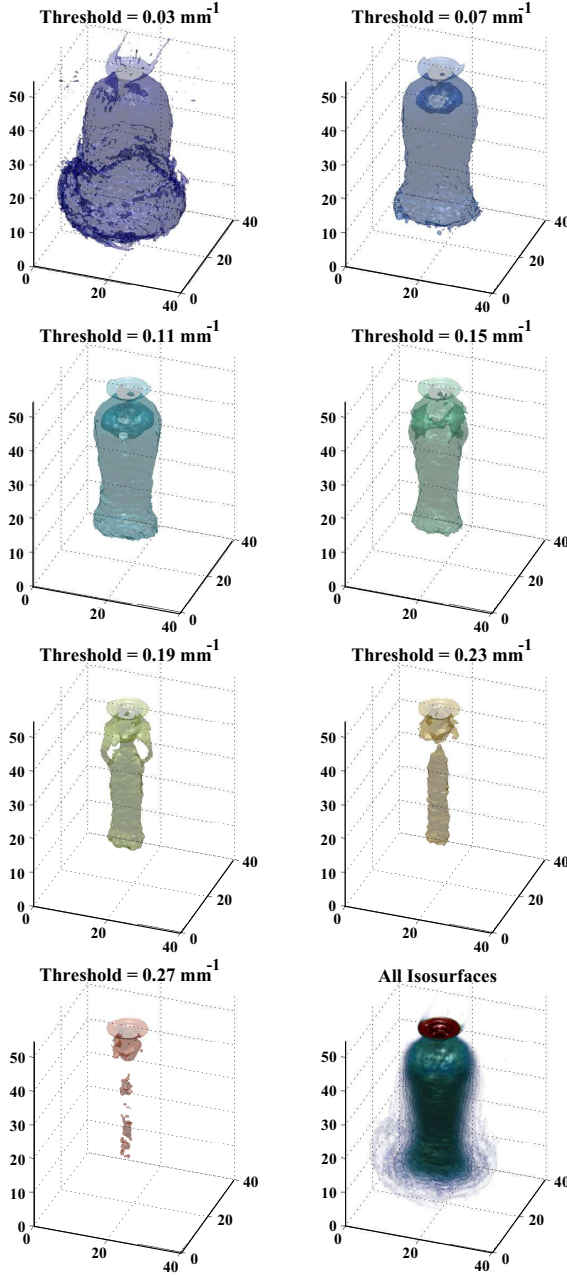**Figure 6.40:** *3D views of the 6-hole water spray for different μ_e thresholds.*

Figure 6.41: *3D views of the GDI spray for different μ_e thresholds.*
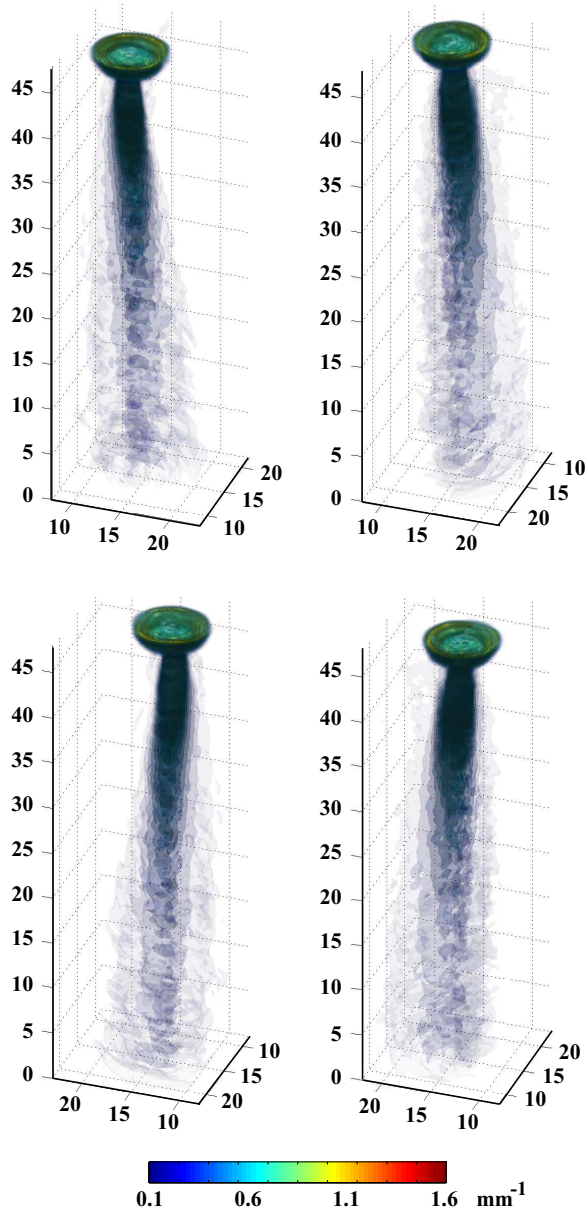
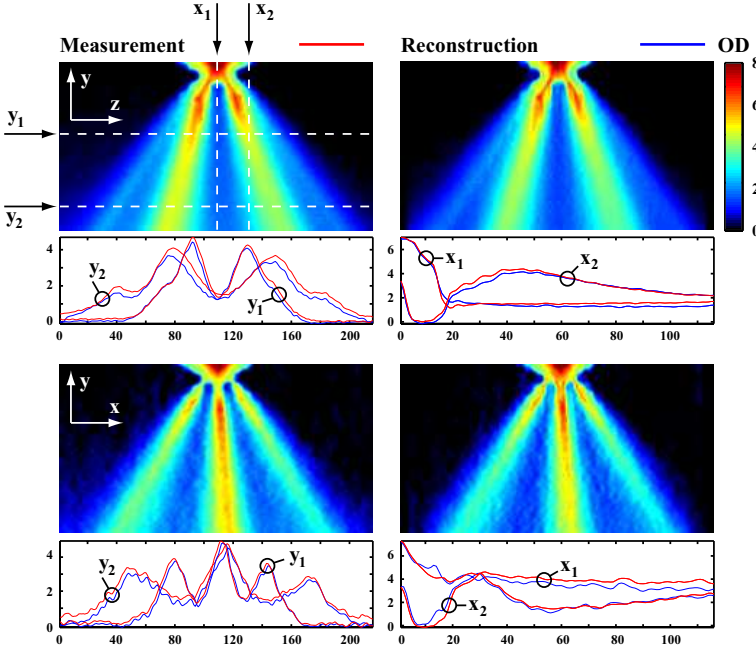**Figure 6.42:** *3D views of the solid cone water spray.*

Figure 6.43: *Evaluation of the validity of the CT reconstruction algorithm, showing two comparisons between the OD acquired either experimentally (left) or calculated from the CT 3D model (right). The graphs show cross-sections of the OD values (see dashed lines in the top left image). The top and bottom images show the OD along the x- and z-axis, respectively.*

6.7 Considerations and Limitations

Forward Scattering

The diffuse light filtering process of SLIPI relies on a change in photon trajectory. This implies that if photons are scattered more than once but in the exact forward direction prior to detection, the SLIPI process will be unable to suppress this intensity contribution. Hypothetically, the removal of these unique, yet undesired, photons would require a laser sheet with an intensity modulation along its incident direction (i.e. horizontal intensity modulation).

As discussed and illustrated in Chapter 3.2.1, the probability for forward scattering depends on the scattering phase function which, in turn, depends on the dimensionless size parameter x. In the Mie scattering regime, an increase in D/λ leads to a more pronounced forward scattering peak (shown in Fig. 3.4). This implies that SLIPI will not perform equally well when two equally turbid samples but with different droplet size distributions are probed (see Paper VII for more information on this topic).

For qualitative imaging this size dependence is an attractive feature as the preservation of the forwardly scattered photons makes the probed object falsely appear less turbid. Consequently, the negative impact of laser extinction and signal attenuation

is reduced, leading to better S/N-values (especially on the exit side of the sample). However, for quantitative imaging of μ_e the size dependency is a highly undesired feature as the evaluated extinction coefficients will be underestimated. Moreover, the error in μ_e depends on the local droplet size distribution of the spray, making correction approaches difficult (if possible).

Instead of compensating for the issue, there are means to mitigate the effect. The most straightforward approach is to increase the line frequency of the superimposed modulation. This will improve the sensitivity of SLIPI and allow the detection (and thus the suppression) of low-angle zigzagging snake photons. Figure 6.44 illustrates the improvements in multiple scattering suppression achieved by increasing the line frequency. In this demonstration a homogeneous scattering solution (water mixed with milk) is probed with an intensity modulation of either $0.08 \cdot f_c$ or $0.16 \cdot f_c$ (where f_c is the cutoff frequency of the OTF).
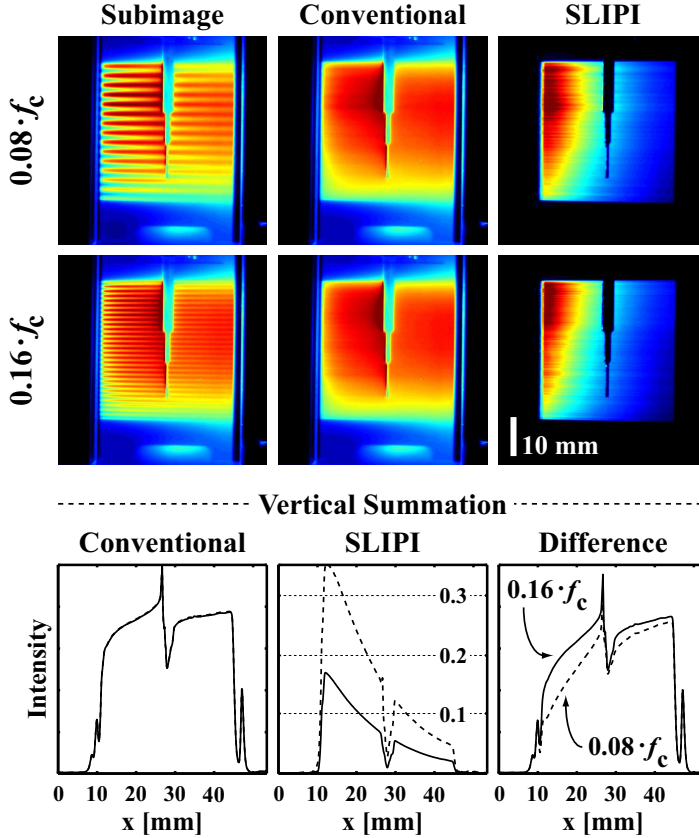
Figure 6.44: *Demonstration of the influence of the line frequency, where more narrow lines results in a better removal of multiply scattered light. All images as well as the vertical summations of the conventional curves are normalized to unity. The graph denoted "Difference" shows the difference in intensity between the conventional and SLIPI summations. Worth noticing is the fact that the conventional images are unaffected by the line frequency.*

107

Although the two SLIPI images qualitatively appear identical they differ in terms of absolute values, as shown in the vertical summations (conventional curves normalized to unity). The graph denoted "Difference" show the intensity difference between the conventional and the SLIPI summations. As seen, the use of a more narrow line structure leads to a greater intensity removal and the SLIPI curve tends towards a single exponential curve (which is interpreted as an improvement in its filtering capability). These results demonstrate the potential for accurate suppression of multiple light scattering, which is required when aiming at quantitative results.

Resolution

The spatial resolution of the detector also influences the multiple light scattering suppression ability of a SLIPI system. Poorly resolved lines will increase the inability to detect, and thereby discriminate against, the snake photons. This is illustrated in Fig. 6.45. Basically, a snake photon cannot be differentiated from a ballistic photon if it, during its path through the sample, remains within the same row of pixels. Hence, better resolved lines will reduce the amount of snake photons in the final SLIPI image.

Figure 6.45:   *The influence of the spatial resolution. Better resolution lead to the detection, and thus rejection, of snake photons, which only marginally deviate from their original trajectory.*
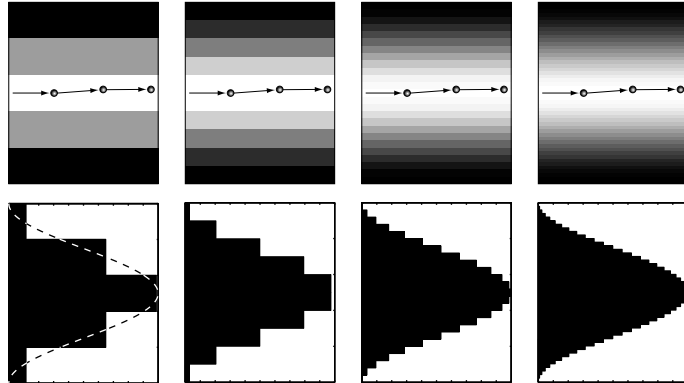
Level of Turbidity and Dynamic Range

As discussed earlier, a good dynamic range is essential when studying an optically dense, light scattering medium. Actually, this is a general concern but becomes especially apparent when utilizing SLIPI, as illustrated in Fig. 6.46. In this example six differently turbid, homogeneous, light scattering samples (level of turbidity unknown) are probed using either SLIPI or conventional PLI (light enters from the left). Due to laser extinction, the signal from the singly scattered light decreases significantly over the imaged area and in the most optically thick case (Fig. 6.46 F) only a fraction of the sample can be visualized using SLIPI. In these situations, where the singly scattered light intensity is below the unavoidable noise level of the detection system, alternative means to probe the sample should be considered, e.g. ballistic imaging.

Apart from illustrating the limitations of SLIPI (in terms of turbidity), the example in Fig. 6.46 also illustrates well the inaccuracy of conventional PLI when applied on optically dense, light scattering media. As the level of turbidity increases (going

from A to F), two distinct errors are observed; (1) in contrast to the exponential decay of intensity predicted by the Beer-Lambert law, the signal level increases with distance and (2) the laser sheet becomes wider, illuminating more of the surrounding volume. Vertical summations of the images are presented in the graphs.
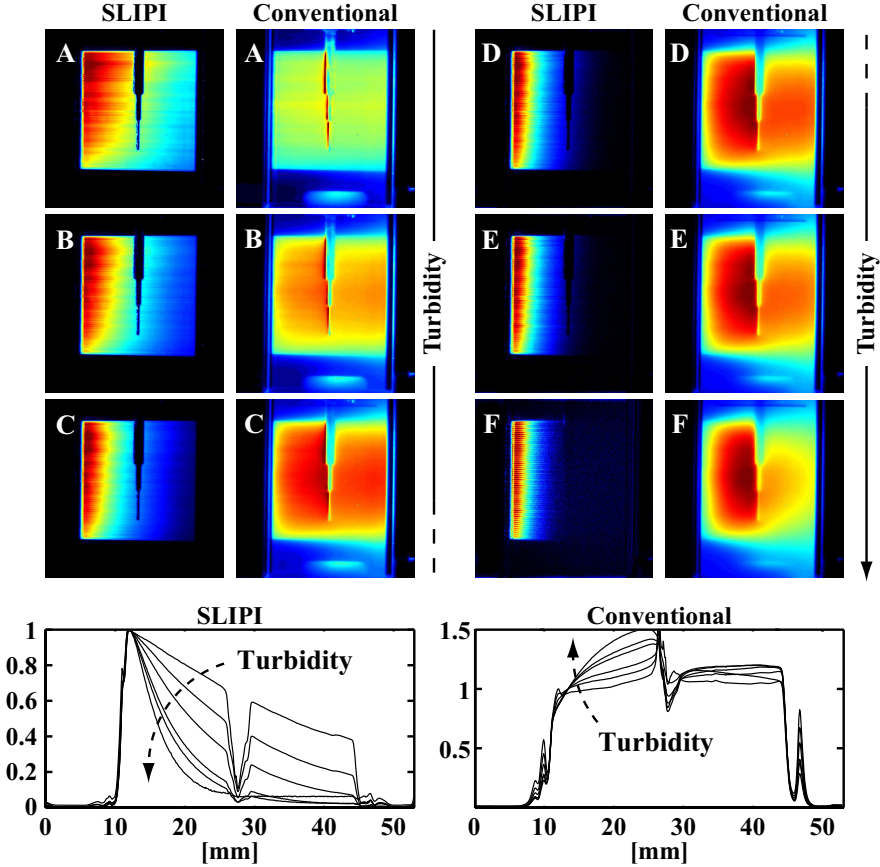
Figure 6.46: *Conventional PLI and SLIPI applied on six differently turbid, homogeneous, light scattering samples. Due to the homogeneity, the scattered light intensity should decrease exponentially with distance, as is observed when applying SLIPI. However, due to the detection of multiply scattered light, an inversed trend is observed in the results obtained when using conventional PLI. At a certain the level of turbidity, laser extinction becomes too severe and SLIPI can only visualize a fraction of the illuminated sample.*

Chapter 7

Experimental Arrangement and Post-Processing Routines

THIS chapter is dedicated to those who intend to implement SLIPI. Various methods to create and phase shift a structured illumination are described. The appearance of residual line structures as well as the recommended steps on how to mitigate these undesired fringes are discussed in detail.

7.1 Intensity Modulation

7.1.1 Grid Projection

A spatially modulated laser sheet can be created using various approaches. As briefly mentioned previously, probably the most straightforward method - grid projection - consists in imaging a mask target with a sinusoidally varying transmission pattern. This concept was employed in Paper I - IV and VII. The approach requires only two lenses; one to form an image of the sinusoidal target and one to optically compress the beam into a structured light sheet. A schematic of the optical arrangement is provided in Fig. 7.1 (A), where the sheet-forming optical component is omitted. Even though the creation of the structured laser sheet is principally simple using grid projection, it renders some experimental challenges. Firstly, the modulation depth m of the imaged sinusoidal pattern varies with distance, having its maximum at the image plane. If the distance between the target and the imaging lens (with a focal length of f) is D, the maximum modulation depth is obtained approximately at

$$L = \frac{1}{1/f - 1/D} \tag{7.1}$$

Therefore a flexible system, where the position of the target can be altered, is imperative to ensure a maximized m. In addition, the focal length f should be chosen long enough to avoid m to vary within the imaged area, as this will be interpreted as variations in the singly scattered light. Failing to properly adjust and align the op-

tical components often leads to residual image artefacts. Finally, since these targets are based on absorption, their damage threshold is relatively low.
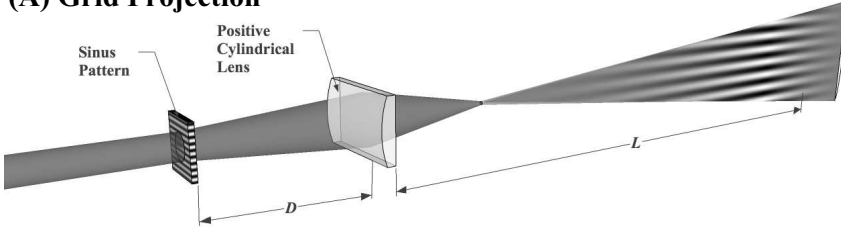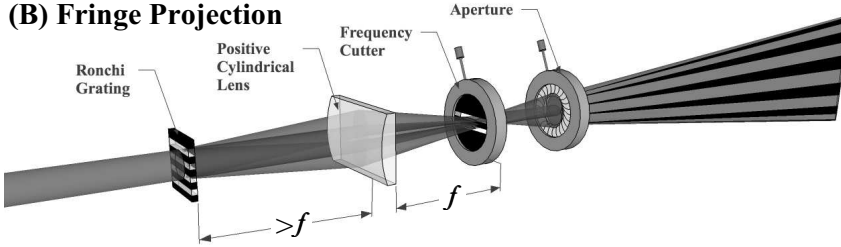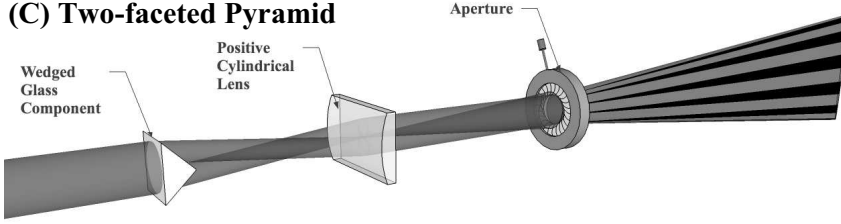
Figure 7.1: *Simplified schematics for three different methods to create a structured light sheet.*

7.1.2   Fringe Projection

The second approach in Fig. 7.1 uses two coherent beams which interfere to achieve structured illumination, first demonstrated by Neil *et al.* [93]. Two plane waves which are incident on an object at angles $\pm\theta$ form a fringe pattern with a periodicity T_f given by Eq. 7.2 [91].

$$T_f = \frac{\lambda}{2\sin(\theta)} \tag{7.2}$$

One of the benefits with this approach is that the modulation depth of the pattern remains nearly constant with distance, thus eliminating the alignment problems associated with grid projection. Secondly, the illumination field will only contain a

single spatial frequency, which lowers the risk for eventual residual line structures in the final SLIPI image.

There are different approaches to create two coherent plane waves. Neil *et al.* split the incident beam using a beam-splitter and refocused them onto the specimen [93]. This method is not readily applicable in macroscopic imaging, as it leads to a relatively large θ due to the required spacing between the optical components involved in the setup. As seen in Eq. 7.2, a large incident angle produces a narrow line structure that may fall outside the cutoff frequency of the detection system. For instance, a θ of 1° produces a fringe pattern with a periodicity of merely 15 μm when $\lambda = 532$ nm.

The work presented in Paper V-VI and VIII-XI implements an alternative fringe projection method, where the incident angle can be reduced significantly, thereby making it suitable for macroscopic imaging. The approach is based on illuminating a Ronchi grating, consisting of alternating opaque and transmissive stripes. Unlike for the grid projection method the opaque stripes reflect the incident light, thereby increasing the damage threshold.

When illuminating a square wave target with equidistant stripes the incident light source is dispersed and split into several *orders of diffraction*. Each order has a certain magnitude and direction which, in turn, depends on the mask. The current case gives rise to odd harmonics of the fundamental frequency, as seen from its Fourier series expansion

$$T = 0.5 + \frac{2}{\pi} \left(\cos\left(2\pi\nu x + \phi\right) + \frac{1}{3}\cos\left(3\left(2\pi\nu x + \phi\right)\right) + \frac{1}{5}\cos\left(5\left(2\pi\nu x + \phi\right)\right)... \right) \quad (7.3)$$

where T represents the transmitted light intensity. The dispersion angle θ_n of each diffraction order n depends on the spatial frequency ν_g of the grating and the wavelength λ according to

$$\theta_n = \sin^{-1}\left(n \cdot \nu_g \cdot \lambda\right) \quad (7.4)$$

Reconstructing the initial square pattern is principally impossible since all diffraction orders must contribute in the image formation process. Due to their large dispersion angle, the information carried by the higher diffraction orders are lost, which explains why such an illumination field is not implemented in structured illumination.

Obtaining the desired coherent plane waves consists in rejecting all but the ± 1 diffraction orders (see Fig. 7.2 and 7.3). This can be accomplished by focusing the transmitted light onto a "frequency cutter" device positioned at the Fourier plane. Such an apparatus can be constructed in various ways. For the work presented in this thesis, the device consisted of two blades (mounted on translational stages) which block higher orders of diffraction. This can be performed with relative ease as the 1st and 3rd orders are well separated in space. The same is not true for the 0th order. Being only marginally separated from the desired ± 1 orders, the rejection of this un-diffracted light is more challenging but can be performed by positioning a thin thread in-between the blades. As will be demonstrated, complete rejection of the 0th order is crucial to avoid residual line structures in the final SLIPI image. If the spatial frequencies are located too narrowly one solution is to increase the fundamental grid frequency ν_g, as this leads to a larger separation between the frequencies (see Eq. 7.4).

Figure 7.2: *Device to perform spatial frequency filtering when illuminating a square wave target. Two blades, each mounted on a translation stage, block higher order frequencies. A thread is used to reject the 0th diffraction order.*
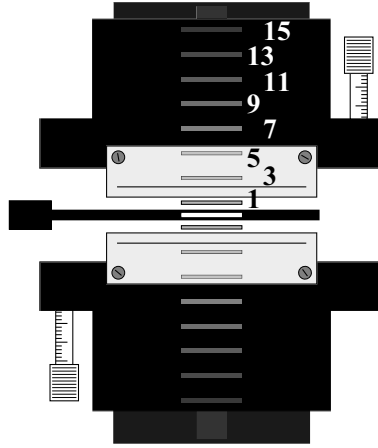
With distance, the expanding ±1 diffraction orders eventually overlap and interfere, thus creating the desired sinusoidal intensity pattern. The full procedure is exemplified in Fig. 7.3, where it also can be noticed how the spatial frequency of the modulation decrease with distance. Unfortunately the approach leads to a substantial loss of energy (∼50%) due to the required rejection of the 0th and higher spatial frequency orders.
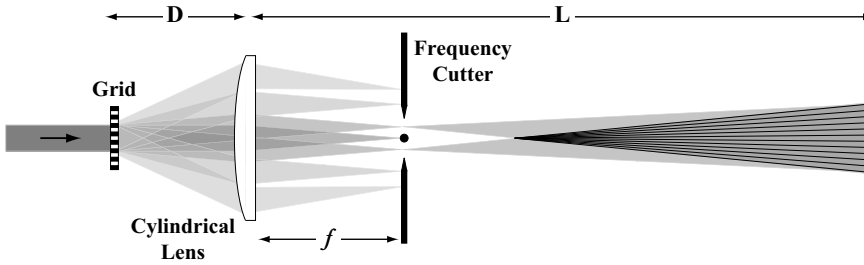
Figure 7.3: *A structured beam created by letting the 1st orders of diffraction interfere.*

7.1.3   Two-faceted Pyramid

The final approach, yet to be tested for SLIPI, is based on the idea presented by Lei and Zumbusch who used a four-faceted symmetric pyramid to create a structured illumination [91]. The concept is illustrated in Fig. 7.4 for a two-faceted glass component. In principle, the optical element works as a wave-front divider that, via refraction, splits the incident beam in two. As for fringe projection, the two coherent beams interfere and give rise to a sinusoidal intensity modulation with a periodicity of $T_f = \lambda/2\sin\theta$. In contrast to grid- and fringe projection, the optical component involved in the creation of the sinus pattern neither absorbs nor reflects the incident light, thus improving the damage threshold significantly. The resulting structured

illumination is, however, only created within a restricted area that, in turn, is given by the open angle γ. The sample must be placed within this so-called *interference zone*. For most spray applications, this requirement cannot be met due to potential wetting of the optical component.
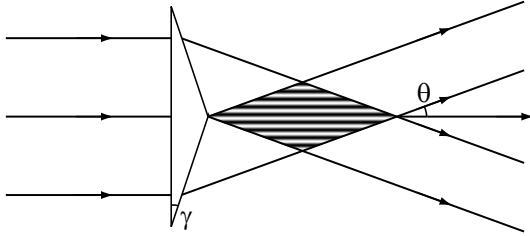

Figure 7.4: *The principle of the two-faceted pyramid approach. The component divides a plane wave in two due to refraction and the resulting beams create the sinus pattern via interference. Adopted from [91].*

Figure 7.5 illustrates how to solve this issue. By means of a telescope, the interference zone can be moved farther away from the optics. This arrangement furthermore allows the crossing angle to be adjusted by changing the distance between L_1 and L_2, which, in turn, allows the spatial frequency to be altered.

The increased damage threshold is the major advantage with the method. However, to obtain a "perfect" modulation depth that does not vary over the imaged area, the two interfering beams should, in principle, have identical intensity profiles. This is most straightforwardly achieved if the incident beam has a uniform intensity distribution. Since the creation of such a top-hat profile usually is associated with large energy losses[1], the final intensity might not differ significantly compared to fringe projection. It could be mentioned that one alternative solution to achieve a uniform intensity distribution with negligible losses is by means of arrays of micro-lenses [94–97]. Unfortunately this method cannot be readily implemented for structured illumination (when the modulation is created through interference) as these systems are not suited for coherent radiation.
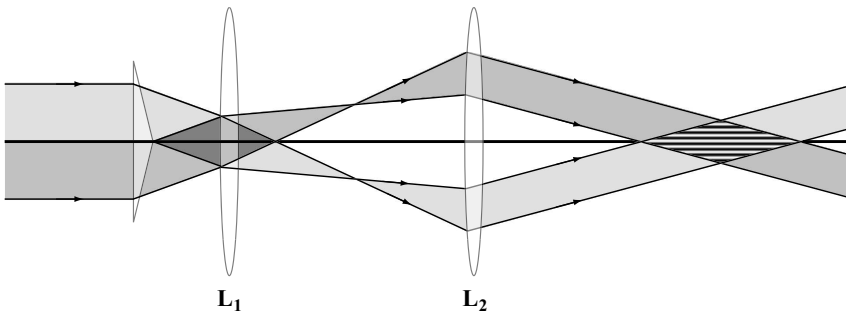

L_1 L_2

Figure 7.5: *Solution to move the interference zone away from the optics.*

---

[1]A top-hat beam profile is commonly achieved by selecting the central part of the laser beam followed by spatial filtering.

Additional Method for Intensity Modulation

In the literature, one additional experimental approach to create a spatially modulated laser sheet can be found. The method is based on scanning the sample vertically with a laser beam whilst simultaneously modulating the intensity *in time* [98].

7.2   Phase-shifting
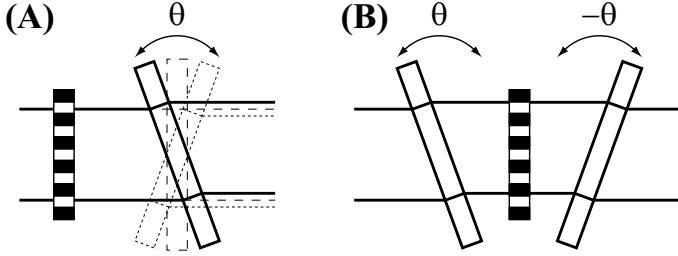
Figure 7.6: *Phase-shifting methods using glass platelets.*

For all the SLIPI measurements presented in this thesis, the required phase shift was performed by tilting a glass platelet. The method, which is illustrated in Fig. 7.6 (A), is experimentally simple and has both good precision and repeatability, yet it requires a calibration procedure. The calibration can be performed by placing a cuvette with a homogeneous scattering substance in the measurement region. The angle θ of the platelet is then varied and the phase ϕ measured for each θ. The acquired data is then fitted with a polynomial expression (3rd order is sufficient) from which the correct angles are extracted, as exemplified in Fig. 7.7.

Figure 7.7: *Calibration measurement. The spatial phase varies almost linearly with the inclination θ of the glass platelet. The value of ϕ at $\theta = 0$ is set as a reference.*

The precision depends on the step size of the rotational stage as well as on the required inclination, which, in turn, depends on the plate thickness. The negative

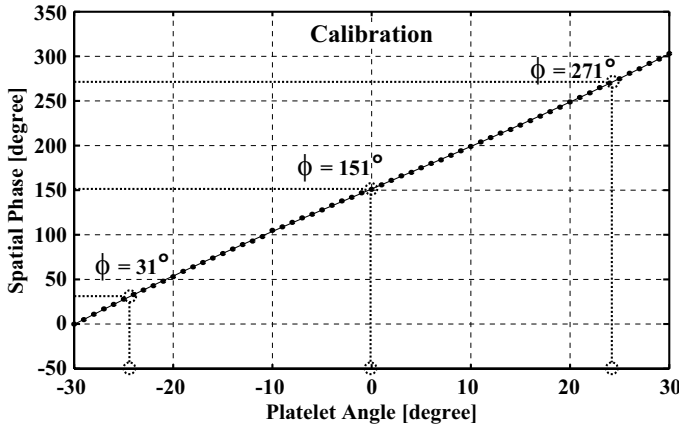aspect with the approach is that the entire beam profile is displaced in the process, thus also shifting any spatial variations in intensity. This may lead to residual lines in the reconstruction procedure that must be corrected for. Relying fully on post-processing routines to accurately suppress such structures is not advised. Instead, if the approach in Fig. 7.6 (A) is to be implemented, it is strongly recommended to uniformize the beam profile, by means of e.g. selecting the central part of the laser beam and to filter out eventual high spatial frequencies. If the available energy is too low, two options can be considered; (1) using an actuator to move the grating itself or (2) using the method presented in Fig. 7.6 (B). In the latter case, two oppositely inclined platelets are situated on either side of the grating. Neither of the two methods shift the beam profile, which, in effect, will reduce the appearance of residual lines.

7.2.1 Phase Determination

Determining the phase of the modulation can be done by studying the Fourier transform of the acquired image. This mathematical tool is very important for structured illumination. In short, the Fourier transform is an operation that decomposes its input - a 1D vector or an image - into its corresponding sine components. Thus, the Fourier transform of the illumination employed in SLIPI would ideally result in three non-zero points; the intensity dc offset called the 0th order and, on either side, the fundamental frequency ($\pm 1^{st}$ order)[2]. An example of the Fourier transform is given in Fig. 7.8, illustrating how a square wave is constructed from a certain composition of sine waves with different spatial frequencies and amplitudes. The Fourier transform presents this information by arranging each sine component along the x-axis with a y-value corresponding to its amplitude.
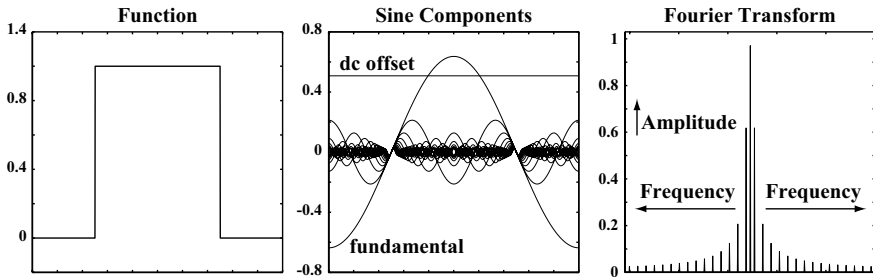
Figure 7.8: *The Fourier transform of a square wave.*

Information regarding the spatial phase of each sine component is also embedded in the resulting transform. Although not shown in Fig. 7.8, the Fourier transform produces a complex output (most often only the absolute value is presented as this contains most of the information concerning the geometrical structure of the input function). To accurately inverse transform the data back into the spatial domain the imaginary part is equally important. The phase of a certain spatial frequency ν can

---

[2]All but the 0th order appear twice in the Fourier transform. One explanation for this is that a sinus wave has no implicit direction and its frequency is equal when going from left to right or *vice versa*.

be determined by calculating

$$\phi = \tan^{-1}\left(\frac{\text{Im}(\nu)}{\text{Re}(\nu)}\right) \tag{7.5}$$

The theory of Fourier transformation has three important implementations for SLIPI; (1) for the alignment of the optical arrangement, (2) for the calibration of the tilting angle of the glass platelet and (3) for the data post-processing. Cases (1) and (3) will be discussed at a later stage.

Accurate calibration of the glass platelet requires detection of the fundamental ($\pm 1^{\text{st}}$) frequency. For the results presented in this thesis, the common procedure was to image a homogeneous scattering medium situated in the measurement region. The use of a homogeneous sample serves two purposes. Firstly, it does not fluctuate in time, which makes it easier to automate the procedure. Secondly, it narrows the distribution of low spatial frequencies, making the fundamental frequency more isolated.

Figure 7.9 illustrates the procedure to determine the spatial phase of a laser sheet with a superimposed sinusoidal intensity modulation. In the example the laser sheet traverses a homogeneous sample, Fig. 7.9 (A). For reasons of clarity, effects caused by laser extinction, signal attenuation and multiple scattering are omitted. The Fourier transform of (A) is provided in (B), where the fundamental frequency component is indicated[3]. To evaluate the phase of the modulation the position of the fundamental frequency must be determined, preferably automatically. This can be achieved by rejecting the low frequency part of the spectrum, thereby avoiding the prominent 0th order, Fig. 7.9 (C). In this selected region, the absolute value of the fundamental frequency dominates, making it straightforward to automatically determine its position. Figure 7.9 (D)-(F) shows the complex spectrum for three different spatial phases (centered around the fundamental component). The corresponding phases for all points in (D)-(F) are presented in (G)-(I) wherein the phase for the fundamental frequency is marked by a circle. These graphs illustrate the importance of knowing the exact location of the spatial frequency of interest, since the phases for the nearby components will give an incorrect value.

---

[3]Although the Fourier transform of (A) is two-dimensional, it contains no valuable information along the x-direction (in this specific case). Therefore, the Fourier transform of (A) can be represented in one dimension.
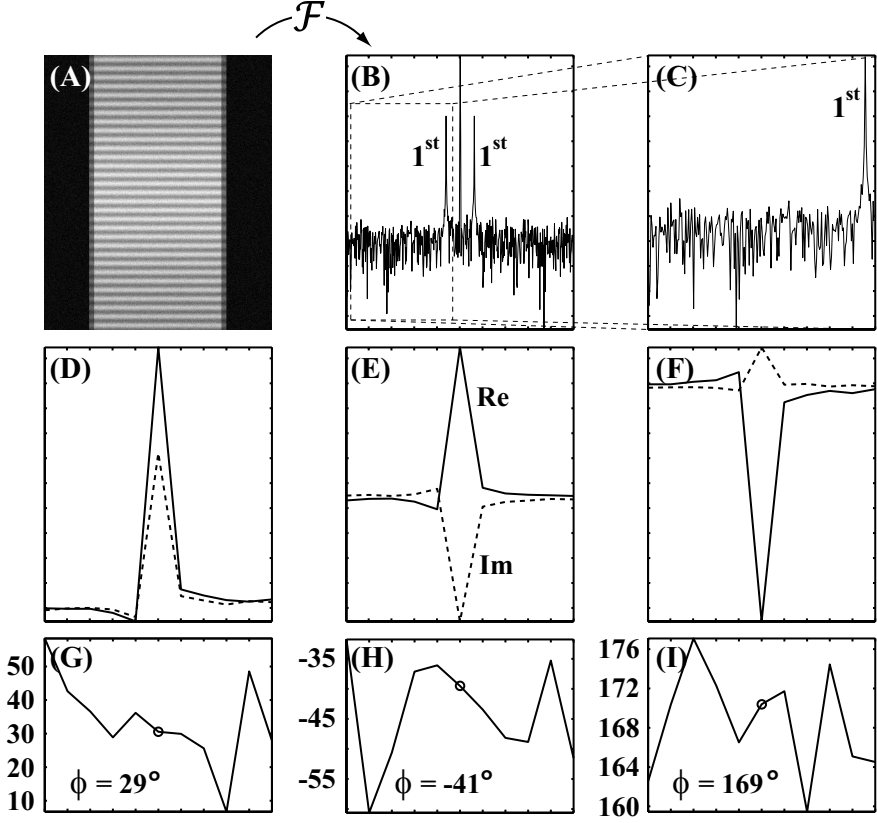
Figure 7.9: *Phase determination procedure. (A): Signal generated as a structured laser sheet propagates through a homogeneous sample. (B): The corresponding Fourier transform. (C): Automatically selected region. (D)-(F): Real and imaginary part of the spatial frequencies surrounding the fundamental frequency. (G)-(I): The phase evaluated for each point in (D)-(F). The circle marks the phase at the fundamental frequency.*

7.3 Alignment and Data Post-Processing Routines

7.3.1 Mask Orientation

In contrast to SIM, the modulated beam is optically compressed in one direction with SLIPI. The orientation of the optics involved is therefore an essential factor and to optimize the system the mask target (square grating, sinus target or wedged glass) and the cylindrical lenses involved must be mounted on components with which the inclination is adjustable. Figure 7.10 shows two examples of such mounts. Note that if fringe-projection is employed, tilting the grating affects the spatial frequencies at the frequency cutter device, that might need readjustment.

Figure 7.11 illustrates how the modulation depth is affected by an erroneous grid orientation. Since the SLIPI signal lies in the modulated component it is essential to maximize the modulation depth. It is therefore recommended to, if possible, continuously monitor the modulation strength during the alignment by e.g. extracting
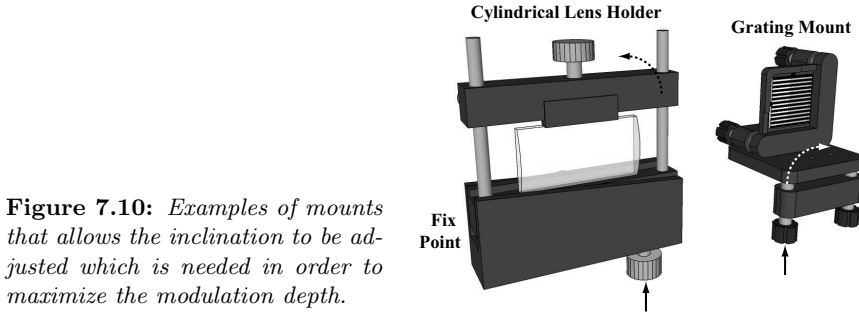
Figure 7.10: *Examples of mounts that allows the inclination to be adjusted which is needed in order to maximize the modulation depth.*

the Fourier transform. This approach also shows whether unwanted harmonics are present. Since these can render residual line structures in the final SLIPI image, such harmonics should be dealt with beforehand.
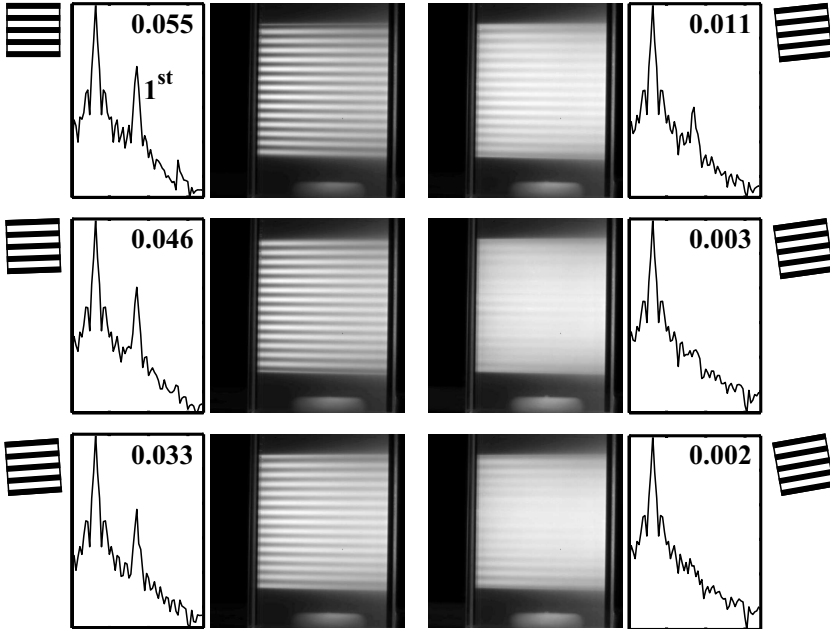
Figure 7.11: *Loss of modulation depth due to the orientation of the mask target. The drawing indicates the angle of the target. A part of the Fourier transform is given beside each image (logarithmic scale). The numbers indicate the ratio between the 1st and the 0th order.*

7.3.2   Residual Lines

Residual lines are undesired artefacts in the final SLIPI image and originate from the employed illumination scheme. Often they are caused by imprecise instrumental hardware, resulting in an incomplete demodulation of the structured illumination.

The instrumental factors mainly responsible for the creation of these stripe patterns are:

- Temporal fluctuations in the mean illumination intensity

- Spatial intensity variations in the laser sheet profile

- Inaccurate phase shifts

- Inadequate filtering of spatial frequencies (fringe projection)

In the literature, photo-bleaching is often referred to as a major contributer [99]. However, this is of no concern for spray studies.

Depending on the frequency contents of the residuals it is possible to make an assessment of the cause, as exemplified in Fig. 7.12. Figure 7.12 (A) illustrates an ideal measurement situation where there is no sign of any residual frequency components in the Fourier transform (logarithmic scale). In (B) the sample is illuminated with different intensities. This is simulated by setting the modulation depth different for each spatial phase, in this case $m_1 = 0.45$, $m_2 = 0.4$ and $m_3 = 0.35$. The corresponding Fourier transform of the resulting SLIPI signal indicates the presence of both the fundamental spatial frequency ν as well as overtones of ν. In (C), the illumination intensity is constant but the phase angle ϕ_3 is $2\pi/4$ instead of $2\pi/3$. This scenario gives rise to intensity fluctuations at 2ν and can thereby be differentiated from the previous case. However, when the two effects are combined, illustrated in (D), the frequency content is not readily distinguishable from (B).

These differences in frequency contents provide information regarding the origin of the artefacts. As a rule of thumbs: residuals appearing at ν are caused by variations in the mean intensity while imprecise phase shifts lead to fluctuations at 2ν. Note, however, that there are several other factors responsible for the appearance of residual stripes. A detailed analysis of image artefacts and means to suppress them can be found in [99].

7.3.3 Line Spacing

There are several approaches to diminish the appearance of fringe artefacts. Data post-processing routines can, to some extent, correct for variations in intensity and phase shifting errors, yet it is not advisable to fully rely on these. As pointed out by Cole *et al.*, one straightforward method to reduce the visual appearance of the residual lines is by choosing the fundamental spatial frequency ν so that its overtones are naturally attenuated by the OTF [81]. By setting $\nu > 0.5f_c$ all lingering harmonics fall outside of the cutoff frequency border, thus becoming "invisible". Unfortunately it is experimentally challenging to use such a narrow line separation and it is more preferable to use an illuminating spatial frequency of $\sim 0.2f_c$.

Figure 7.13 illustrates how the appearance of residual fringes can be reduced by increasing the fundamental line frequency. In the example a homogeneous sample was illuminated using fringe projection and the Fourier transforms of one of the subimages and the resulting SLIPI image are provided beside each figure (logarithmic scale). Two different gratings, having either 5 or 10 line pairs per mm, were illuminated. To purposely generate fringe artefacts two methods were used; either by, in addition
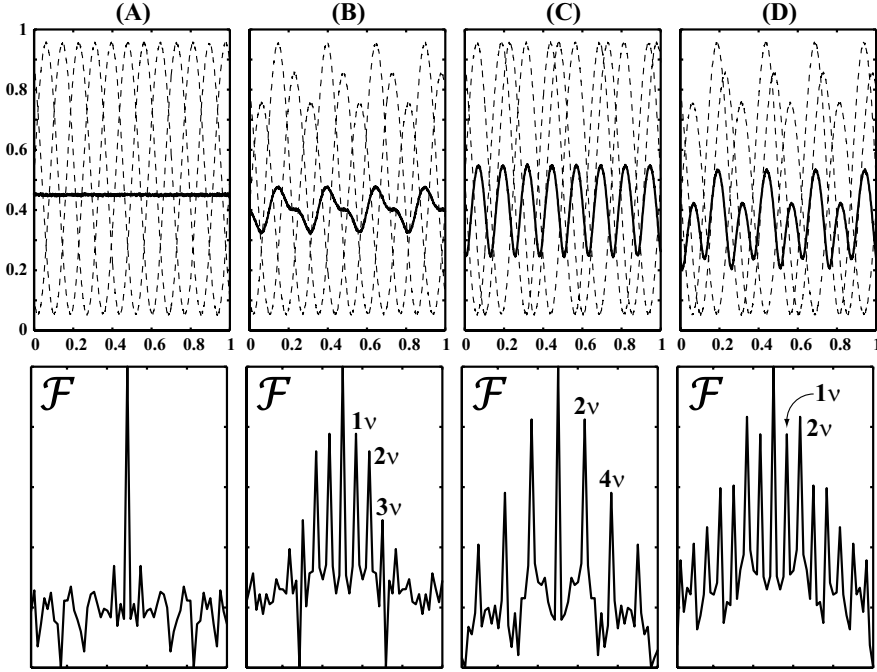
Figure 7.12: *Experimental factors causing residual fringe patterns. (**A**): Ideal situation, no artefacts visible. (**B**): Different mean intensities in the three images, leading to fluctuations at the fundamental frequency ν as well as at its harmonics. (**C**): Erroneous phase shifting, causing residuals to appear at even multiples of ν. (**D**): The two effects combined.*

to the $\pm 1^{\text{st}}$ orders, allowing the 0th order to pass the frequency cutter (A-D) or by letting higher harmonics pass (E-H).

With the first method, the presence of the 0th order reduces the crossing angle θ between the beams by a factor of two which, in turn, leads to an increased periodicity T_f (see Eq. 7.2). In addition, since three beams interfere the illumination will contain two sine components, where only the fundamental frequency is completely demodulated when applying Eq. 6.1. The second component will instead cause residuals with a spatial frequency of 3ν, which is why it is important to reject the non-diffracted light when using fringe projection. By increasing ν by a factor of two (going from A to C) it is noticeable how the OTF's natural attenuation of high frequency information leads to less (visually) apparent residuals.

Similar effects are noticed when instead letting higher orders pass the frequency cutter device. In E, where the grating with 5 lp/mm was used, harmonics of ν almost up to the seventh order are visible in the incident laser sheet. When extracting the SLIPI image, these overtones gives rise to stripe patterns, the strongest at 3ν[4]. By once again increasing ν by a factor of two (case G), the frequencies of the residual lines reside nearer the cutoff frequency and, consequently, become much less apparent. For instance, the residuals arising from the 3rd order in the incident laser sheet (Fig.

---

[4]These are created by the 2nd order. The residuals from the 3rd order appear at 6ν.
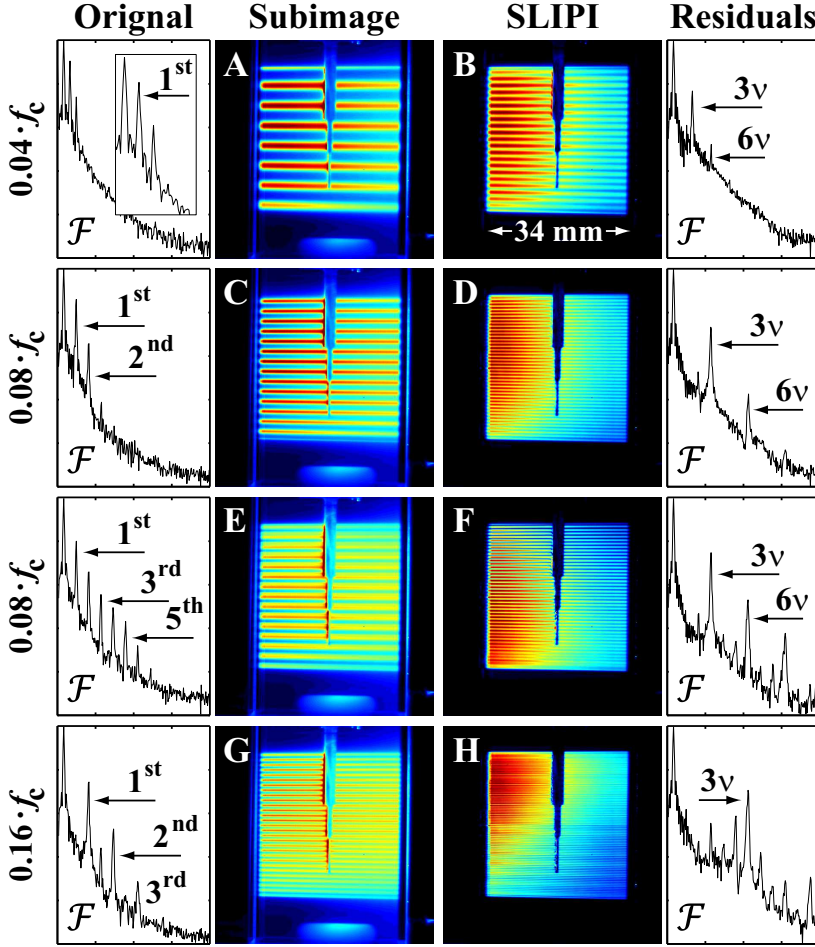
Figure 7.13: *Example showing how the natural attenuation of high spatial frequencies reduces the visual appearance of residual line structures. In A and E, a grating with 5 lp/mm was illuminated, while a grating with 10 lp/mm was used in C and G. The corresponding SLIPI images, together with their respective Fourier transforms are also provided. The spatial frequency of the fundamental component is also indicated for each case.*

7.13 G) are almost completely attenuated as they appear at around $0.96 f_c$ (6ν). The results presented in Fig. 7.13 illustrates the importance of removing any additional sine components in the laser sheet prior to implementing SLIPI.

7.3.4   Correction for Phase Shift Errors

As shown in Fig. 7.12, an error in the phase shifts of the incident intensity modulation leads to residual lines with a spatial frequency of 2ν. Cole *et al.* demonstrated a post-processing routine to compensate for this error [81]. In contrast to Eq. 5.4, where it is assumed that the grating is translated exactly $1/3$ of a period, the authors extracted the phase information from the three subimages and included this in the

calculation of the sectioned image according to[5]

$$I_S = \left| \frac{1}{2 \cdot \sin\left(\frac{\phi_1 - \phi_3}{2}\right)} \right| \cdot \left| (I_3 - I_1) + i \left[\frac{(I_1 - I_2)}{\tan(\frac{\phi_1 - \phi_2}{2})} - \frac{(I_2 - I_3)}{\tan(\frac{\phi_2 - \phi_3}{2})} \right] \right| \qquad (7.6)$$

The relative phase differences $(\phi_1 - \phi_2)$ and $(\phi_2 - \phi_3)$ are calculated from the subimages using the procedure illustrated in Fig. 7.9. A comparison between the implementation of Eq. 5.4 and Eq. 7.6 is presented in Fig. 7.14. In the example, a homogeneous sample is illuminated with a superimposed sinusoidal structure having a ν of either $0.08f_c$ (A) or $0.16f_c$ (B). The grid displacement is purposely erroneous which, as seen, renders residuals of 2ν when extracting the SLIPI image using Eq. 5.4 (C and D). Once again, choosing a higher fundamental spatial frequency is advantageous as the fringe artefacts appear nearer f_c and are thereby much less visible. By instead implementing Eq. 7.6 (case E and F), the 2ν residuals are almost completely diminished.
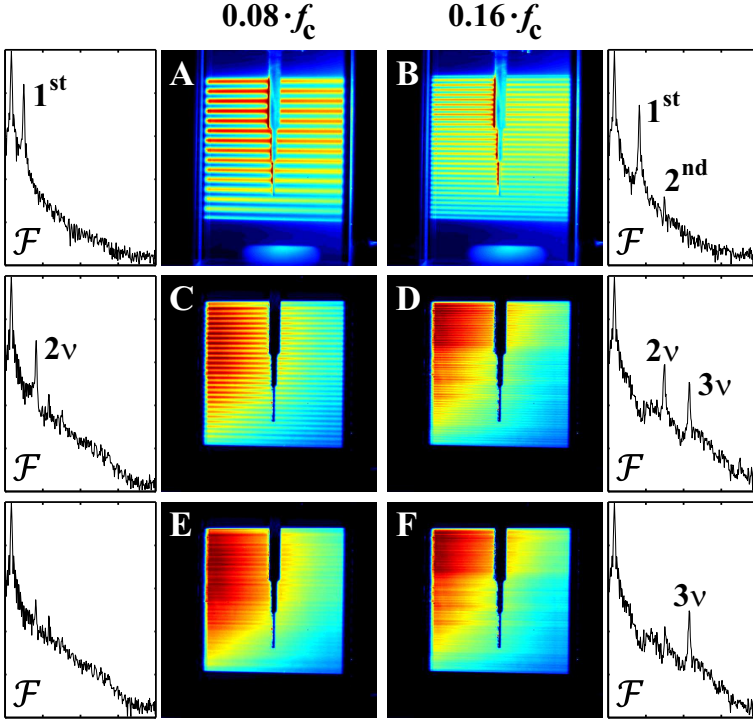
Figure 7.14: *Demonstration of the algorithm used to compensate for phase shift errors.* ***A - B:*** *Modulated images with a ν of either $0.08f_c$ or $0.16f_c$, respectively.* ***C - D:*** *SLIPI images calculated using Eq. 5.4. Notice the strong 2ν component in the Fourier transforms.* ***E - F:*** *Compensation for phase shift errors by means of Eq. 7.6.*

---

[5]The equation in the published manuscript contains a slight misprint, there should be a minus-sign between the two term within the square brackets as printed in Eq. 7.6.

Note, however, that the described methodology is only applicable when the fundamental frequencies are clearly distinguishable in the Fourier domain, as this is a prerequisite for accurate phase determination. Thus, in relatively dense situations, where the line structure can be blurred out very rapidly with distance, the relative phases might be poorly estimated. In these cases, the approach should therefore be used with care as it can have a negative effect on the final SLIPI images. In addition, in Fig. 7.14 D and F it can be noticed how the method is incapable of correcting for residuals residing at 3ν, which in this case arose from the weak, yet still detectable, 2ν sine component in the incident laser sheet.

7.3.5 Correction for Intensity Fluctuations

Regardless whether the wide-field or the laser sheet approach is implemented, the structured illumination technique assumes that the only difference between the three subimages lies in the spatial phase of the incident modulation. Experimentally, this is seldom the case. The light source may have both temporal instabilities and spatial intensity variations that makes it very challenging to meet this requirement. If not accounted for, these experimental factors will lead to unsatisfactory results. Post-processing routines are therefore more or less essential for the proper utilization of structured illumination.

The post-processing procedure used throughout the work presented in this theses is comprised of four steps:

1. Offset correction

2. Mean intensity correction

3. Field-dependent correction

4. Phase correction (when applicable)

The three first steps are illustrated in Fig. 7.15 (B)-(D). The desired aim is to accurately adjust the intensity curves so that the three modulated components alternate around a common offset. This is rarely the case before any correction procedure has been applied (case A), especially when utilizing pulsed laser sources.

Firstly, in (B), the background noise floor is evaluated in each image. This is achieved by calculating the mean intensity in a "zero area", i.e. a region within the recorded image where the signal is known to be zero[6] (see dashed area in Fig. 7.16 (B)). The obtained value is then subtracted from each image. Note that this is not the same as recording and subtracting a "background image" which is a common procedure when performing laser sheet imaging. Unless different cameras are used to record the three subimages (as in Paper II and IV), background image subtraction is conveniently not required for SLIPI.

---

[6]Strictly speaking, the "zero area" can be chosen where the *modulated* component is zero. However, in practice it is convenient to routinely block a small area, e.g. one of the image corners, and to use this as the zero area. This routine is sometimes a built-in feature in camera acquisition programs (e.g. Andor technologies calls it baseline clamp).
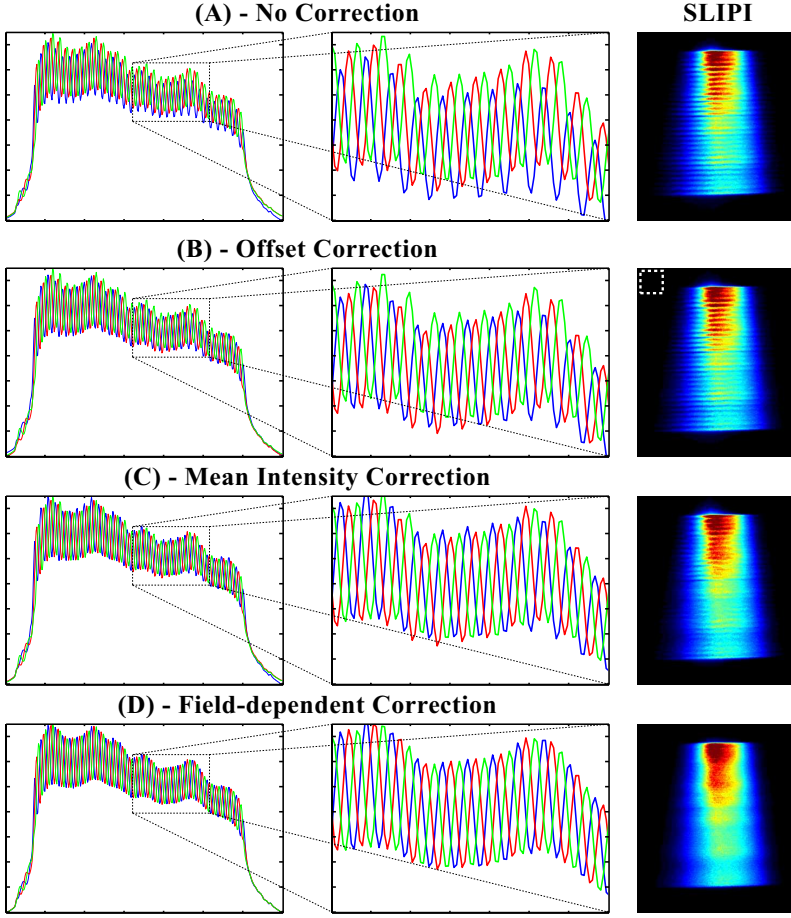
Figure 7.15: *Correction procedure to reduce residual lines. The graphs show a horizontal summation of the three subimages. (A): Raw data without any correction. (B): The average intensity in the dashed area is subtracted from each subimage. (C): Each image is multiplied with k_ϕ (Eq. 7.7), compensating for variations in laser power. (D): Compensation for low frequency variations.*

After offset-correcting the images a uniform correction constant, k_ϕ, is extracted for each image, in accordance with Eq. 7.7, and used as a normalization factor.

$$k_\phi = \frac{\bar{I}_\phi}{\frac{1}{N} \cdot \sum_{i=1}^{N} \bar{I}_i} \tag{7.7}$$

Here $\bar{I}$ denotes the overall average intensity in each subimage. This normalization procedure reduces the amount of residual lines, yet is usually not sufficient to fully remove them. This is mainly due to smooth intensity variations across the images. To compensate for these variations a more rigorous approach is needed which takes into account changes occurring on a pixel-to-pixel level. Figure 7.16 illustrates how to

gain access to this information and to obtain a field-dependent normalization map for all subimages. Each image is first low-pass filtered, where the cutoff frequency of the filter kernel is set just below the fundamental frequency of the incident modulation. From this set of filtered images an average filtered image $\bar{I}_{LP}$ is constructed. Deviations in intensity from $\bar{I}_{LP}$ is then extracted from each subimage on a pixel level, the result of which is shown in Fig. 7.16. Each subimage is then divided with its corresponding field-dependent intensity map, resulting in a SLIPI image mostly free from residual line structures (see Fig. 7.15 (D)). Depending on whether the spatial phases are correct or not, the result can be further improved by applying Eq. 7.6. If the subimages show variations in their high spatial frequency contents one alternative approach is to instead apply a dampening filter on the fundamental frequency component.
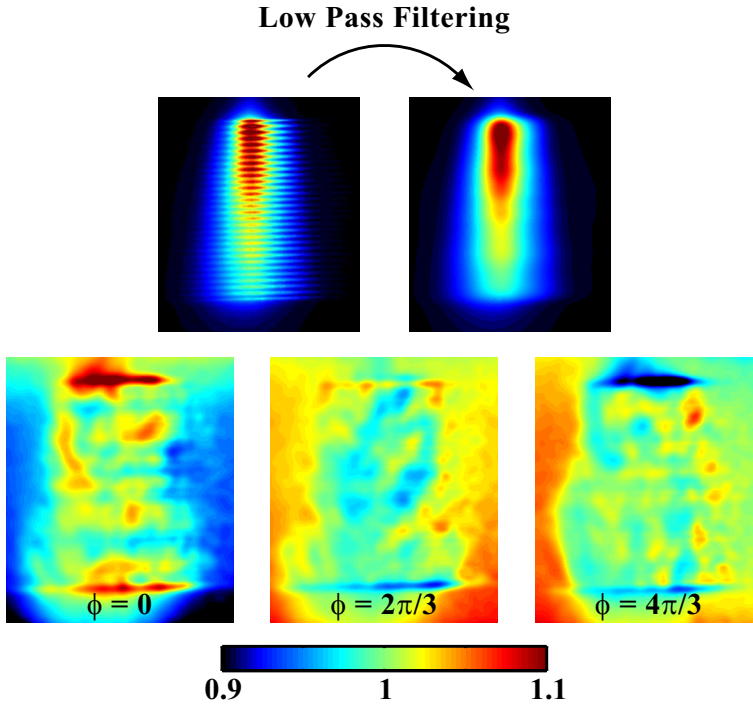

Figure 7.16: *Extraction of differences in low spatial frequencies. Each subimage is low-pass filtered and divided with $\bar{I}_{LP}$, the result of which is shown in the bottom row.*

Chapter 8

Additional Aspects and Applications

T HE primary focus of SLIPI has, so far, been for spray research, yet its filtering capabilities can be exploited in several other domains as well. This chapter describes some other areas of applications and shows some material yet to be published.

8.1 Saturated Laser Induced Fluorescence

A molecule which is pumped from the ground state to an excited state by means of laser absorption produces a fluorescence signal (upon relaxation) which is proportional to the upper level population density. However, depopulation of the excited state can also occur via non-radiative transitions, leading to an uncertainty in the interpretation of the fluorescence. In flame studies, deexcitation through collisions with other molecules - *collisional quenching* - is the dominating source of uncertainty, as it depends on both the local temperature and the chemical environment [100]. One approach to circumvent this issue is by means of saturated LIF.

To explain this concept, consider a simple two-level energy system. The rate equations for the level populations N_i are

$$\frac{dN_1}{dt} = -N_1 b_{12} + N_2 \left(b_{21} + Q_{21} + A_{21} \right) \tag{8.1}$$

$$\frac{dN_2}{dt} = N_1 b_{12} - N_2 \left(b_{21} + Q_{21} + A_{21} \right) \tag{8.2}$$

where b_{12} and b_{21} are the rate constants for absorption and stimulated emission, respectively, Q_{21} denotes the collisional deexcitation rate (collisional excitation is neglected) and A_{21} is the spontaneous emission rate constant [27]. Other non-radiative processes, such as predissociation and photoionization, are neglected here. The rate constants b_{12} and b_{21} are related to the Einstein coefficient for stimulated emission or absorption B through

$$b = \frac{B I_\nu}{c} \tag{8.3}$$

where I_ν incident intensity and c is the speed of light.

To find a simple expression for the upper electronic state population, some assumption must be made; (1) the excited state population N_2 is negligible prior to laser excitation, (2) that the total population N_1^0 remains constant and (3) steady state is achieved. Under these conditions, the upper population density can be expressed according to

$$N_2 = N_1^0 \frac{b_{12}}{b_{12} + b_{21}} \frac{1}{1 + \frac{A_{21} + Q_{21}}{b_{12} + b_{21}}} \tag{8.4}$$

Defining the saturation intensity as

$$I_\nu^S = \frac{(A_{21} + Q_{21})c}{B_{12} + B_{21}} \tag{8.5}$$

yields

$$N_2 = N_1^0 \frac{B_{12}}{B_{12} + B_{21}} \frac{1}{1 + I_\nu^S/I_\nu} \tag{8.6}$$

Thus, if $I_\nu \gg I_\nu^S$ the fluorescence signal becomes independent of both the laser irradiance and collisional quenching [27, 101].

Now, if the incident laser sheet has a sinusoidal intensity modulation, saturation leads to a measurable distortion. Figure 8.1 illustrates the concept for four values of I_ν^S. The left graphs illustrate the effect saturation has on a structured laser sheet ($I_\nu = 100$ mJ for all cases), whereas the right graphs show how saturation generates harmonics of the fundamental spatial frequency (as a function of I_ν). At low values of I_ν the fundamental frequency dominates the Fourier spectrum, i.e. the LIF signal responds linearly and there is no apparent distortion of the sinus-shaped laser sheet. However, as the incident irradiance increases (or, alternatively, I_ν^S decreases), the illuminated medium starts to respond non-linearly. The common approach is to observe the effect in the spatial domain but by implementing structured illumination, this non-linearity becomes visible also in the frequency domain. The value of I_ν^S can thus be determined by means of frequency analysis, e.g. by studying the ratio between the magnitude of the 1st and the 2nd orders as a function of I_ν.

An initial test was conducted to investigate whether the approach is applicable for the determination of I_ν^S. A laminar flow of NO was probed using a structured laser sheet ($\lambda = 226$ nm) and the generated signal was detected at 90 degrees using an intensified CCD camera. To reach intensities sufficient for saturation a lens with a short focal length was employed, see Fig. 8.2. The intensity was steadily increased and monitored using an oscilloscope with a boxcar integrator.

The results are presented in Fig. 8.3. The top row shows two measurements performed at either low or high incident irradiance, where the effect of the short focal length is visible as a sudden decrease in the LIF signal in the latter of the two images. The graph shows the corresponding Fourier transforms of a vertical cross section extracted at the point of focus. Due to the non-linear response of the LIF signal the 2nd order frequency is clearly visible when I_ν is increased beyond the limit of saturation. The three figures in the lower row show a 2D map of the magnitude of the 0th, 1st and 2nd orders at different x positions and incident intensities (rightmost point corresponding to the point of focus, as indicated with the drawing). As expected, the dc offset increases with increased irradiance and decreases as the NO flow becomes saturated. At low laser power the fundamental frequency is relatively weak, but its
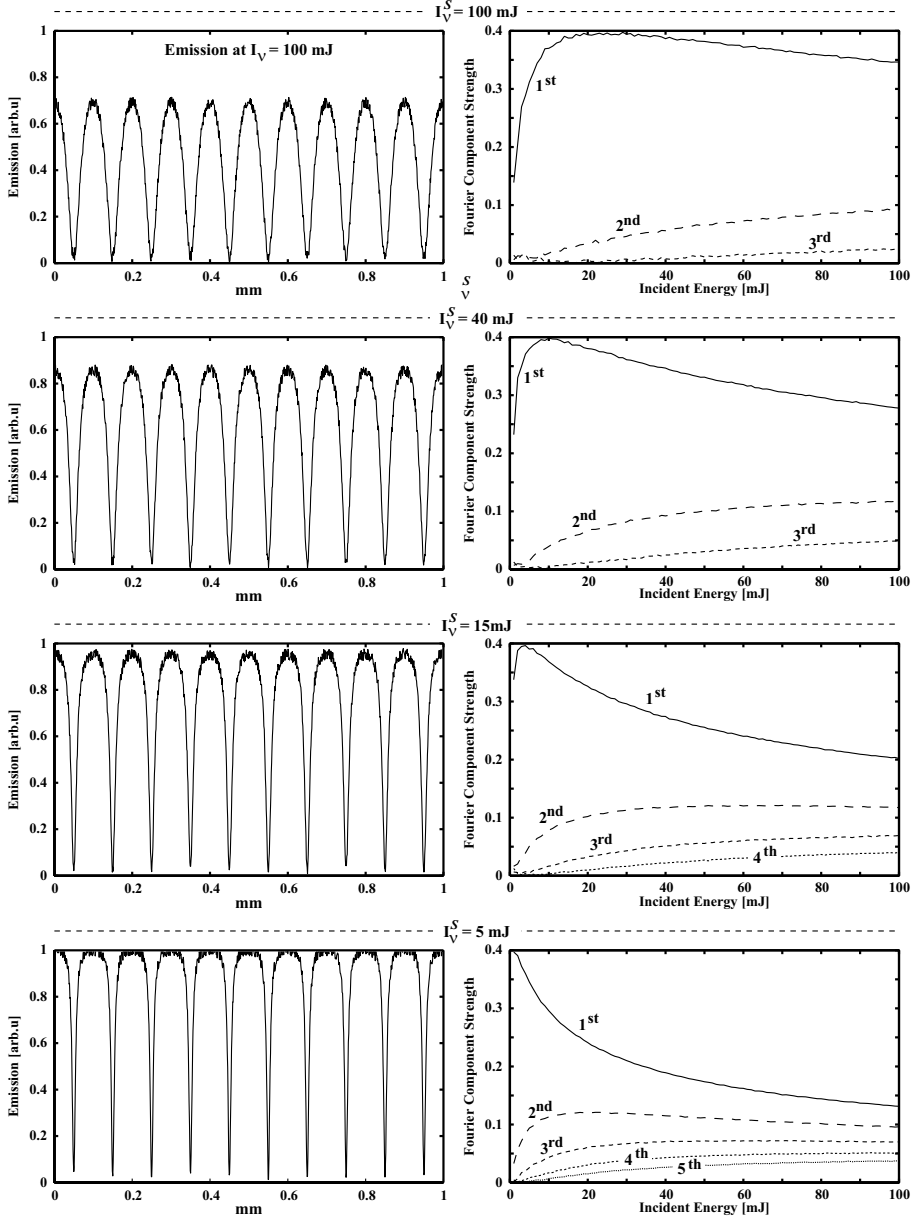
Figure 8.1: *Saturated LIF combined with structured illumination. The left graphs illustrate, for four different values of I_ν^S, how saturation leads to a distortion of the sinusoidal intensity modulation. The right graphs show how the magnitude of the different frequency components change as I_ν increases. By varying the incident irradiance the value of I_ν^S can be determined by analyzing the frequency composition. Noise is added to make the illustrations more realistic.*

Figure 8.2: *Laminar NO flow illuminated with a structured laser sheet at $\lambda = 226$ nm. To reach intensities beyond the limit of saturation the laser sheet is strongly focused.*

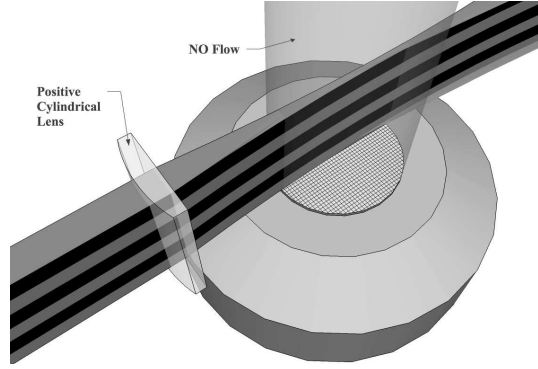magnitude grows with increasing irradiance. This behavior correlates well with that shown in the graphs in Fig. 8.1. The effect of saturation is clearly observable in the 2D map of the 2nd order, which rises above the noise floor at the point of focus as the laser power is increased.

From these results it would, in principle, be possible to determine I_ν^S by comparing the experimental results with the theoretical calculations in Fig. 8.1. The potential benefit with this approach is that the analysis does not rely on the absolute intensity of the fluorescence (although, accurate readings of the absolute values of I_ν are required). However, the method is at its first step of development and more work is needed before it can be accurately implemented.
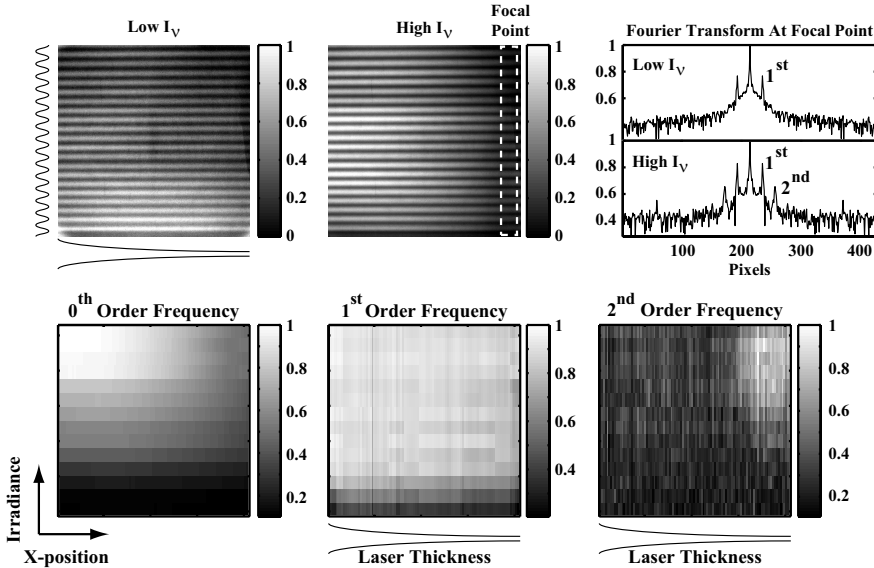
Figure 8.3: *Demonstration of how to measure saturation using structure illumination. The top row shows two recordings, acquired at either low or high laser power, together with the corresponding Fourier transform (for a vertical cross-section at the point of focus). The bottom row shows a 2D map of the 0th, 1st and 2nd orders. By comparing these results with those presented in Fig. 8.1 it is, in principle, possible to determine the value of I_ν^S.*

8.2 Blurring Caused by ICCD Cameras

Intensified CCD cameras are commonly employed for combustion research as these devices enable rapidly occurring events to be captured and disturbing background flame luminosities to be suppressed. However, the use of ICCDs can have an influence on the image contrast, especially when rapid gating is utilized.

The working principle of an ICCD is shown in Fig. 8.4. The incident light falls on a photocathode, causing the release of electrons. An electric field guides the emitted electrons into a so-called *multi-channel plate* (MCP), consisting of several narrow channels (Fig. 8.4 B). Inside these channels a secondary-emitting material gives rise to a multiplication, resulting in an avalanche of electrons (Fig. 8.4 C). The level of amplification is set by the applied voltage. After leaving the MCP the electrons impinge on a phosphor screen that converts them to photons, which are lead to the CCD chip (either by means of optical fibers or lenses) where the information is read out [102].

The purpose of the applied voltage between the photocathode and the MCP is twofold. Firstly the signal can be gated very rapidly (nanosecond scale) by switching the voltage on or off[1] and secondly, to guide the emitted electrons to the MCP channels. However, during the rise and fall time of the gate function (when the applied voltage is relatively low) the electric field is not always sufficiently strong to ensure the correct (straight) guidance of all electrons, as shown in Fig. 8.4 B. This leads to a blurriness that is similar to that caused by multiple light scattering and can therefore be removed by means of SLIPI.
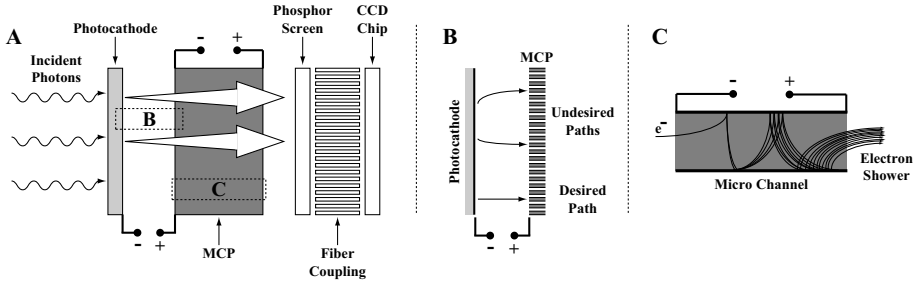

Figure 8.4: *Schematic diagram of the principle of an intensified CCD detector. Light which falls onto a photocathode is transformed into electrons. These are amplified in a multi-channel plate and then re-transformed into photons. Adopted from [102].*

The described effect is only of concern when measurements are performed using a very short gate, i.e. when a relatively large fraction of the signal is collected during the rise and fall time of the gate function. The work on fluorescence lifetime imaging, demonstrated by Ehn *et al.*, is such an application [103]. In short, this technique enables fluorescence lifetime measurements in 2D by recording the LIF signal using a short- and a long gate function. By knowing the exact shape of the gate functions it is possible to evaluate the fluorescence lifetimes on a pixel level by comparing the signal collected by the two cameras. If the two required measurements are performed simultaneously the technique allows instantaneous realizations.

---

[1]Certain types of cameras additionally switch the MCP voltage on or off.

8.3   Double "Single-Shot" SLIPI

Future developments and improvements in hardware will allow SLIPI to be implemented for 2D velocimetry measurements of high-pressure injection systems by combining the technique with e.g. PIV or PTV. The approach will, however, require three high power double-pulsed laser sources to enable the recording of two "single-shot" SLIPI images. Moreover, the time separations between consecutive pulses should be ∼10 μs (depending on the velocity of the spray). Unfortunately the laser system employed within the framework of this thesis did not meet these requirements.
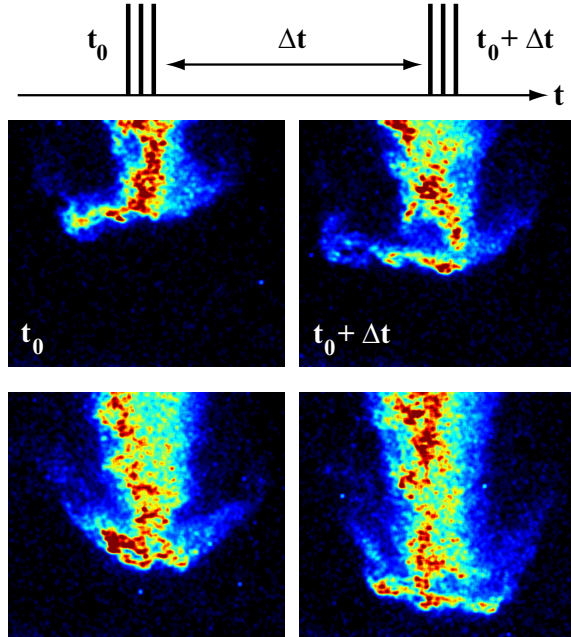

Figure 8.5: *Double "single-shot" SLIPI measurements of the leading edge of a transient spray generated by a GDI injector. The three pulses and their subsequent double-pulses (separated 50 μs in time) are illustrated at the top.*

Figure 8.5 shows two examples of double "single-shot" SLIPI measurements of a transient spray generated by a GDI injector. The images were acquired using the setup described in Chapter 6.3.2, where the second image triplet was obtained by double-pulsing the lasers (time delay $\Delta t = 50\mu s$). Although the signal levels are sufficient the time separation between the consecutive pulses must be reduced in order to accurately determine the velocity of the flow. With the employed laser system, a reduced time delay leads to insufficient signal levels.

8.4   Interfering Background Noise

Image noise in planar laser imaging is not always attributed to multiple light scattering. Other interfering sources of noise in spray or combustion related research are e.g. chemiluminescence, undesired reflections, stray light, elastically scattered light in LIF measurements (and *vice versa*). As long as the interfering signal is unaffected by the spatial phase shift of the superimposed intensity modulation SLIPI will enable the rejection of this undesired intensity contribution. Note, however, that

since the suppression process takes place *after* image acquisition, the desired signal that is generated by the laser sheet cannot be completely "drowned" in the interfering noise.
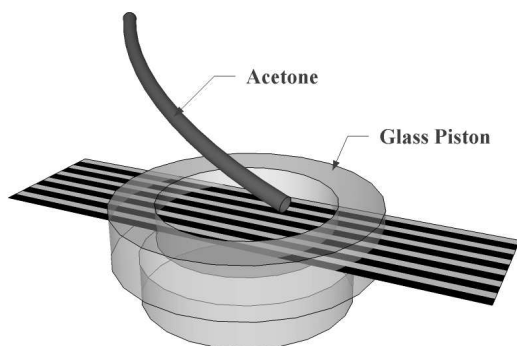

Figure 8.6: *A flow of acetone being guided into the bowl of a quartz piston. The sequential fluorescence signal is detected through the piston (i.e. from below).*

To demonstrate the applicability of SLIPI for the removal of interfering background noise a flow of acetone was guided into the bowl of a quartz piston, see Fig. 8.6. The spatially modulated laser sheet ($\lambda = 266$ nm) was arranged to intersect the flow and the generated fluorescence signal was detected through the piston from below. This commonly implemented optical arrangement can lead to undesired interfering signals as both the incident light and the signal may be reflected inside the confinement. This is illustrated in Fig. 8.7, showing measurements performed using both conventional laser sheet imaging and SLIPI.
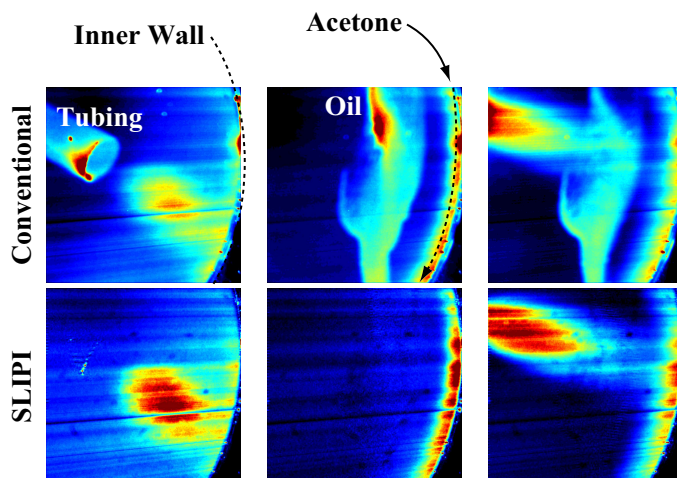
Figure 8.7: *Examples of interfering signals.* **Left**: *Acetone tube positioned within the cameras field-of-view, becoming visible as it reflects the acetone fluorescence.* **Middle - Right**: *Oil purposely smudged onto the piston.*

In the leftmost conventional image the acetone tube is clearly visible, as it reflects the fluorescence signal. As seen, the implementation of SLIPI filters out this undesired reflection. In the middle and rightmost cases, a thin layer of lubricant oil was intensionally applied on the piston. In these cases the oil is illuminated by the

incident light which is internally reflected on the walls. This, in turn, gives rise to a strong interfering fluorescence. SLIPI performs well in suppressing this overlying signal.

8.5 Rayleigh Thermometry

One commonly employed approach to achieve 2D temperature readings of flames in combustion research is by means of Rayleigh scattering. In short, the method is based on the ideal gas equation, stating that the number density of the Rayleigh scattering particles is inversely proportional to the local temperature. The scattered light intensity therefore scales with T^{-1}, thus providing the opportunity for thermometry. There are, however, considerations one must bear in mind. For instance, the scattered intensity also depends on variations in the so-called *effective Rayleigh cross-section*, which, in turn, depends on variations in the mole fraction (see [104] for more information on this topic).

Since the scattered light intensity scales as $1/T$ the signal level in high-temperature regions becomes very weak. This, in turn, makes the technique very sensitive to stray light detection which may arise from e.g. camera lenses and surfaces surrounding the flame [105]. With the filtering capabilities of SLIPI, this undesired intensity contribution could be diminished in the data post-processing.

One complication, which makes the implementation of SLIPI for Rayleigh thermometry experimentally challenging, concerns the need for high laser power to detect the relatively weak signal from the combustion zone. The high power needed to reach sufficient signal levels will doubtlessly damage the optical components required for both the fringe- and the grid projection arrangement. Whether the required level of irradiance is achievable using the two-faceted pyramid approach needs to be investigated.

8.6 CW-PLIF

The single species detection ability of PLIF has made the technique one of the most popular and frequently applied imaging techniques within combustion research. The technique employs temporal filtering to remove interfering signals, which arise primarily due to chemiluminescence. This approach involves the use of short laser pulses in combination with fast-gated intensified camera systems. However, since the chemiluminescence is completely unaffected by illumination, its intensity contribution could be removed by means of SLIPI. Neglecting issues related to laser power and tunability, which are essentially hardware limitations, the implementation of SLIPI could, in principle, enable PLIF measurements of flames using continuous light sources in combination with non-gated camera systems. This would significantly reduce the cost for a PLIF system, yet unfortunately, the approach is not applicable with the hardware commercially available today.

8.7 Optical Engine Measurements

The study of in-cylinder conditions of an IC engine during operation by means of optical diagnostics requires some modifications to the original design of the en-

gine. Optical access to the combustion chamber can made possible by replacing some metal parts with quartz windows. The required number of optical ports depends on the measurement technique one intends to utilize. For instance, line-of-sight chemiluminescence imaging requires "only" a quartz piston, whereas planar laser imaging typically require both a quartz piston as well as a transparent liner (to get optical access from the side).

SLIPI was applied on an optical engine to study wall-jet as well as jet-jet interactions of a non-reacting, evaporating spray. The main motivation for implementing SLIPI was to suppress interfering background signals created by e.g. reflections on the cylinder head and on the walls of the piston bowl, sources of error which ordinarily makes measurements close to a glass surface challenging. Figure 8.8 shows an example of an image acquired using SLIPI and conventional imaging during engine operation. The laser sheet was aligned to intersect the downstream (evaporated) spray region, yet still the upstream liquid spray plumes are clearly visible in the conventional image (where also the asymmetry of the injector can be seen). Near the surface of the wall of the piston bowl, two of the four plumes can be seen, where plume (1) is transported into the FOV by the swirling motion of the gas flow. As seen in the result, the implementation of SLIPI leads to significant improvements in image quality where all apparent background signals in the conventional case have been suppressed.
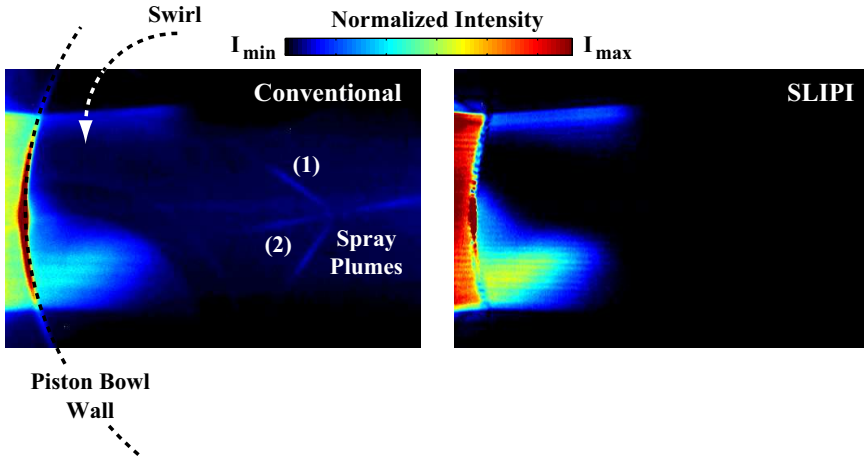
Figure 8.8: *A gas jet impinging on the piston bowl wall, imaged using either conventional PLI or SLIPI. The four spray plumes, which are not directly illuminated, as well as background signals, mainly from reflections in the walls and cylinder head, is noticeable in the former case.*

One experimental difficulty arising when utilizing SLIPI for engine studies that is worth mentioning concerns the need for absolute stability. Even the slightest vibration may cause movements in the incident line structure. This comes as no surprise since the spacing between the lines in a 5 lp/mm Ronchi grating is only 200 μm. Thus, vibrations in the laboratory leading to a lateral displacement of this component of merely 67 μm will result in a spatial phase shift of 1/3 of the sinusoidal line structure.

Chapter 9

Summary and Outlook

To conclude, a novel imaging technique named SLIPI has been developed. Unlike most other optical techniques, SLIPI enables the suppression of multiply scattered light, which has, until now, been a major limiting factor for both laser sheet- and transmission imaging when applied to optically dense media. The method combines laser sheet imaging and structured illumination to distinguish between the directly and multiply scattered light, where only the former of which provides an accurate and faithful description of the probed sample. The main results and achievements of this thesis are enumerated as follows:

- Structured illumination has been successfully implemented for single-ended, depth-resolved, backscattering imaging of a dilute flow of water droplets. The approach enabled the visualization of internal sample structures, which, due to the detection of out-of-focus light, were obscured when utilizing conventional backscattering imaging.

- A novel planar laser imaging technique (SLIPI) has been developed which improves and enhances visualization of optically dense light scattering media. The capabilities of the technique has been demonstrated, with convincing results, on several different turbid samples, including liquid atomizing sprays as well as homogeneous light scattering samples.

- Technical solutions to enable "single-shot" SLIPI imaging have also been demonstrated. A flow characterized by relatively slowly moving particles can be visualized using two pulsed laser sources (one running in double-pulsed mode), whereas rapidly moving samples require three individual lasers.

- The accuracy, precision and limitations of the SLIPI technique was investigated for both Mie scattering and LIF on different homogeneous scattering samples with different particle concentrations and diameters. The results conclusively show the advantages of SLIPI that presented superior repeatability, yet perhaps the most striking results in this campaign concerned the visualization of the intensity decay predicted by the Beer-Lambert law, demonstrated up to an OD of 6. To the best knowledge of the author, such results have not been demonstrated

for laser sheet imaging of optically dense scattering and fluorescing media in the past.

- A novel quantitative imaging technique, named dual-SLIPI, which allows the extinction coefficient to be visualized in 2D has also been developed within the framework of this thesis. Unlike previous methods to measure this optical property, the presented technique is based solely on side-scattering detection. Furthermore, the technique does not require a calibration procedure and it can be directly applied to the central region of an inhomogeneous scattering medium.

- A second quantitative imaging technique, referred to as SLIPI-scan, has also been developed. Unlike dual-SLIPI, this technique allows the extinction coefficient to be spatially resolved in 3D, which is of fundamental importance when attempting to characterize inhomogeneously dispersed, optically dense, light scattering media. To compensate for signal attenuation the sample is probed using a "bread slicing" manner. By measuring the path-integrated attenuation of light (by means of SLIPI), the effect of laser extinction can be quantified which, in turn, allows the local extinction coefficient to be extracted.

- An alternative method to visualize the extinction coefficient in 3D has been demonstrated. This approach is based on combining structured illumination with computed tomographic imaging. Since CT is based purely on transmission data, signal attenuation is of no concern here. However, to accurately measure the attenuation of light using visible light sources, multiple light scattering must be eliminated, hence the use of SI. The validity of the method was first tested on a homogeneous scattering medium and then demonstrated on three different atomizing spray systems.

- SLIPI requires three images to suppress the multiply scattered light, thus limiting its applicability. To partly overcome this limitation, a computer algorithm that extracts the local amplitude of the incident intensity modulation on a single subimage was developed. This bears information regarding the attenuation of light which, in turn, can be used to estimate the optical depth (by means of an exponential fitting routine). The method is, however, mostly suitable for homogeneous media.

- Finally, the SLIPI method was applied on a non-reacting diesel spray for both Mie scattering and fluorescence. Due to the high optical depth associated with the diesel spray, almost no directly scattered was observed in the central part of the spray at early times after start of injection. In an attempt overcome this severe attenuation of light, dual-SLIPI was (successfully) applied on the spray. However, when the contribution of directly scattered light fall below the unavoidable camera noise level, the information becomes noisy and unreliable. Droplet sizing by means of LIF/Mie SLIPI imaging was also demonstrated (qualitative data only).

Recommendations for future work:

- One of the main limitations of SLIPI concerns forward scattering. Light that is multiply scattered but in the exact forward direction prior to detection cannot be suppressed. This is advantageous for qualitative imaging but reduce the accuracy of any quantitative imaging technique which is based on SLIPI. Further work to address this issue is required, for instance by means of Monte-Carlo simulations. However, it should also be investigated whether this feature could be exploited for droplet sizing.

- When applied to optically dense media, the singly scattered light intensity contribution becomes relatively weak. A camera system with good dynamic range is therefore required. Although, the most appropriate approach is to suppress the multiply scattered light prior to detection, for instance by means of polarization filtering. This may allow even optically thicker samples to be probed.

- Bidirectional illumination should be tested, as this partly eliminates laser extinction. However, since the two SLIPI measurements cannot be performed simultaneously, this approach will double the acquisition time.

- The potential for droplet sizing by means of PDS and SLIPI should be investigated in more detail. Since droplet size and number density is linked through the extinction coefficient, both these quantities could, in principle, be extracted by combing a sizing technique with e.g. dual-SLIPI.

- Finally, to have an even greater impact in the spray community, future spray studies by means of SLIPI should be carried out in collaboration with spray modelers, to provide accurate and reliable input data for validation purposes.

Acknowledgements

Most of the work presented in this thesis was carried out at the division of combustion physic in Lund and I want to thank everyone working there for creating such a friendly and pleasant environment. In particular, I would like to express my appreciation to the following persons:

Marcus Aldén: You not only employed me (for which I am obviously very grateful) but you also believed in the work I was carrying out during these years and you spurred me to dig deeper. I wish I had your strategic mind and your way of seeing things in a larger context.

Mattias Richter: Your door was always open (with the keys in the keyhole) and you always set aside whatever you were doing to answer my questions and help me. You are a human encyclopedia when it comes to lasers and engines.

Collaborators: During these years I've had the opportunity of working together with researchers from outside Lund University and would especially want to thank Lucio Araneo, Stephan Wissel, Mark Linne and Peter Hottenbach. I learned a great deal by working with you.

Colleagues: In particular I would like to thank Nils-Erik Olofsson, Malin Jonsson, Billy Kaldvee, Andreas Lantz, Alexis Bohlin, Christoph Knappe, David Sedarsky, Johan Zetterberg, Johan Sjöholm, Sven-Inge Möller, Cecilia Bille, Eva Persson, Minna Ramkull, Joakim Bood and Per-Erik Bengtsson.

Rutger Lorensson: I want to thank you for helping me with all mechanical and technical issues in the lab. You always seem to find an elegant solution to every little problem.

Jonathan Johnsson: You have been a good office roommate. Your Matlab-skills have been invaluable, I do not think there was a single problem you did not manage to solve. As everyone knows at the office, your Google-search skills are also incredible, which has been a tremendous gain for me. And at times of stress you always knew what to do: *"Birds flying high, you know what I mean..."*.

The "support-sandwich"-guy: It is never boring when you are around and I always get inspired by you. You are a good friend and it's unfortunate that we never got the chance to do a project together.

Bibliography

[1]   Chigier, N. *An assessment of spray technology - editorial.* Atomization Sprays, **3**:365–371, 1993.

[2]   Jones, A. and Nolan, P.F. *Discussions on the use of fine water sprays or mists for fire suppression.* J. Loss Prev. Process Ind., **8**:17–22, 1995.

[3]   Dumouchel, C. *On the experimental investigation on primary atomization of liquid streams.* Exp. Fluids, **45**:371–422, 2008.

[4]   Smallwood, G.J. and Gülder, O.L. *Views on the structure of transient diesel sprays.* Atomization Spray, **10**:355–386, 2000.

[5]   Hiroyasu, H., Arai, M., and Shimizu, M. *Break-up length of a liquid jet and internal flow in a nozzle.* In *ICLASS-91, Gaithersburg, Maryland, July.* 1991.

[6]   Ohrn, T., Senser, D., and Lefebvre, A. *Geometrical effects on the spray angle for plain-orifice atomizers.* Atomization Spray, **1**:253–268, 1991.

[7]   Carvalho, I., Heitoyr, M., and Santos, D. *Liquid film disintegration regimes and proposed correlations.* Int. J. Multiph. Flow, **28**:773–789, 2002.

[8]   Siebers, D. *Liquid-phase fuel penetration in diesel sprays.* SAE Paper, **980809**, 1998.

[9]   Zhang, L., Tsurushima, T., Ueda, T., Ishii, Y., Itou, T., Minami, T., and Yokota, K. *Measurement of liquid phase penetration of evaporating spray in a DI Diesel engine.* SAE Paper, **971645**, 1997.

[10]   Johansson, B. *Förbränningsmotorer.* Department of Energy Sciences, 2006.

[11]   Hult, J. *Development of Time Resolved Laser Imaging Techniques for Studies of Turbulent Reacting Flows.* Ph.D. thesis, Lund Institute of Technology, 2002.

[12]   Dec, J.E. *A conceptual model of DI diesel combustion based on laser-sheet imaging.* SAE Paper, **970873**, 1997.

[13]   Husted, B.P. *Experimental measurements of water mist systems and implications for modelling in CFD.* Ph.D. thesis, Lund University, 2007.

[14] Hua, J., an B. Cheong Khoo, K.K., and Xue, H. *A numerical study of the interaction of water spray with a fire plume.* Fire Safety J., **37**:631–657, 2002.

[15] Husted, B.P., Petersson, P., Lund, I., and Holmstedt, G. *Comparison of PIV and PDA droplet velocity measurement techniques on two high-pressure water mist nozzles.* Fire Safety J., **44**:1030–1045, 2009.

[16] Rybicki, G. and Lightman, A. *Radiation Processes in Astrophysics.* John Wiley & Sons, 1979.

[17] Berrocal, E. *Multiple scattering of light in optical diagnostics of dense sprays and other complex turbid media.* Ph.D. thesis, Cranfield University, 2006.

[18] Gomi, H. and Hasegawa, K.I. *Measurements of the liquid phase mass in gas-liquid sprays by x-ray attenuation.* Int. J. Multiph. Flow, **10**:653–662, 1984.

[19] Bohren, C. and Huffman, D. *Absorption and Scattering of Light by Small Particles.* Wiley-VCH, 1983.

[20] Berrocal, E., Sedarsky, D.L., Paciaroni, M.E., Meglinski, I.V., and Linne, M.A. *Laser light scattering in turbid media Part I: Experimental and simulated results for the spatial intensity distributions.* Opt. Express, **15**:10649–10665, 2007.

[21] Melton, L.A. and Verdieck, J.F. *Vapor/liquid visualization in fuel sprays.* In *20th symposium (international) on combustion.* 1984.

[22] Abu-Gharbieh, R., Persson, J.L., Försth, M., Rosén, A., Karlström, A., and Gustavsson, T. *Compensation method for attenuated planar laser images of optically dense sprays.* Appl. Optics, **39**:1260–1267, 2000.

[23] Persson, L., Gao1, H., Sjöholm, M., and Svanberg, S. *Diode laser absorption spectroscopy for studies of gas exchange in fruits.* Opt. Laser Eng., **44**:687–698, 2006.

[24] Berrocal, E., Churmakov, D.Y., Romanov, V.P., Jermy, M.C., and Meglinski, I.V. *Crossed source-detector geometry for a novel spray diagnostic: Monte carlo simulation and analytical results.* Appl. Opt., **44**:2519–2529, 2005.

[25] Gal, P.L., Farrugia, N., and Greenhalg, D.A. *Laser sheet dropsizing of dense sprays.* Opt. Laser Technol., **31**:75–83, 1999.

[26] Driscoll, K.D., Sick, V., and Gray, C. *Simultaneous air/fuel-phase PIV measurements in a dense fuel spray.* Exp. Fluids, **35**:112–115, 2003.

[27] Eckbreth, A.C. *Laser Diagnostics for combustion temperature and species.* Abacus, 1988.

[28] Schultz, C. and Sick, V. *Tracer-LIF diagnostics: quantitative measurement of fuel concentration, temperature and fuel/air ratio in practical combustion systems.* Prog. Energ. Combust., **31**:75–121, 2005.

[29] Adrian, R.J. *Twenty years of particle image velocimetry.* Exp. Fluids, **39**:159–169, 2005.

[30] Kitzhofer, J., Nonn, T., and Brücker, C. *Generation and visualization of volumetric PIV data fields.* Exp. Fluids, **51**:1471–1492, 2011.

[31] Coghe, A. and Cossali, G. *Quantitative optical techniques for dense sprays investigation: A survey.* Opt. Laser Eng., **50**:46–56, 2012.

[32] Koochefahani, M.M. *Molecular tagging velocimetry (MTV): progress and applications.* AIAA Paper, **AIAA-99-3786**, 1999.

[33] Stier, B. and Koochefahani, M.M. *Molecular tagging velocimetry (MTV) measurements in gas phase flows.* Exp. Fluids, **26**:297–304, 1999.

[34] Lempert, W.R., Magee, K., Ronney, P., Gee, K.R., and Haugland, R.R. *Flow tagging velocimetry in incompressible flow using photo-activated nonintrusive tracking of molecular motion (PHANTOMM).* Exp. Fluids, **18**:249–257, 1996.

[35] Gendrich, C.P., Koochesfahani, M.M., and Nocera, D.G. *Molecular tagging velocimetry and other novel applications of a new phosphorescent supramolecule.* Exp. Fluids, **23**:361–372, 1997.

[36] Krüger, S. and Grünefeld, G. *Gas-phase velocity field measurements in dense sprays by laser-based flow tagging.* Appl. Phys. B, **70**:463–466, 2000.

[37] Krüger, S. and Grünefeld, G. *Droplet velocity and accereration measurements in dense sprays by laser flow tagging.* Appl. Phys. B, **71**:611–615, 2000.

[38] Jermy, M. and Greenhalgh, D. *Planar dropsizing by elastic and fluorescence scattering in sprays too dense for phase doppler measurement.* Appl. Phys. B, **71**:703–710, 2000.

[39] Domann, R. and Hardalupas, Y. *A study of parameters that influence the accuracy of the planar droplet sizing (PDS) technique.* Part. Part. Syst. Charact., **18**:3–11, 2001.

[40] Domann, R. and Hardalupas, Y. *Quantitative measurement of planar droplet sauter mean diameter in sprays using planar droplet sizing.* Part. Part. Syst. Charact., **20**:209–218, 2003.

[41] Charalampous, G. and Hardalupas, Y. *Numerical evaluation of droplet sizing based on the ratio of fluorescent and scattered light intensities (LIF/Mie technique).* Appl. Optics, **50**:1197–1209, 2011.

[42] Kawaguchi, T., Akasaka, Y., and Maeda, M. *Size measurements of droplets and bubbles by advanced interferometric laser imaging technique.* Meas. Sci. Technol., **13**:308–316, 2002.

[43] Maeda, M., Kawaguchi, T., and Hishida, K. *Novel interferometric measurement of size and velocity distributions of spherical particles in fluid flows.* Meas. Sci. Technol., **11**:L13–L18, 2000.

[44] van de Hulst, H.C. and Wang, R.T. *Glare points.* Appl. Opt., **30**:4755–4763, 1991.

[45] Damaschke, N., Nobach, H., Nonn, T.I., Semidetnov, N., and Tropea, C. *Multi-dimensional particle sizing techniques*. Exp. Fluids, **39**:336–350, 2005.

[46] Serpengüzel, A., Küçükşenel, S., and Chang, R.K. *Microdroplet identification and size measurement in sprays with lasing images*. Opt. Express, **10**:1118–1132, 2002.

[47] Glover, A.R., Skippon, S.M., and Boyle, R.D. *Interferometric laser imaging for droplet sizing: a method for droplet-size measurement in sparse spray systems*. Appl. Optics, **34**:8409–8421, 1995.

[48] Särner, G. *Laser-Induced Emission Techniques for Concentration and Temperature Probing in Combustion*. Ph.D. thesis, Lund University, 2008.

[49] Omrane, A., Särner, G., and Aldén, M. *2D-temperature imaging of single droplets and sprays using thermographic phosphors*. Appl. Phys. B, **79**:431–434, 2004.

[50] Brübach, J., Patt, A., and Dreizler, A. *Spray thermometry using thermographic phosphors*. Appl. Phys. B, **83**:499–502, 2006.

[51] Huisken, J., Swoger, J., Bene, F.D., Wittbrodt, J., and Stelzer, E.H.K. *Optical sectioning deep inside live embryos by selective plane illumination microscopy*. Science, **305**:1007–1009, 2004.

[52] Huisken, J. and Stainer, D.Y.R. *Even fluorescence excitation by multidirectional selective plane illumination microscopy (mSPIM)*. Opt. Lett., **32**:2608–2610, 2007.

[53] Hertz, H.M. and Aldén, M. *Calibration of imaging laser-induced fluorescence measurements in highly absorbing flames*. Appl. Phys. B, **42**:97–102, 1987.

[54] Versluis, M., Georgiev, N., Martinsson, L., Aldén, M., and Kröll, S. *2-D absolute OH concentration profiles in atmospheric flames using planar lif in a bi-directional laser beam configuration*. Appl. Phys. B, **65**:411–417, 1997.

[55] Sick, V. and Stojkovic, B. *Attenuation effects on imaging diagnostics of hollow-cone sprays*. Appl. Optics, **40**:2435–2442, 2001.

[56] Kalt, P.A.M., Birzer, C., and Nathan, G.J. *Corrections to facilitate planar imaging of particle concentration in particle-laden flows using mie scattering, part 1: Collimated laser sheets*. Appl. Optics, **46**(23):5823–5834, 2007. ISSN 0003-6935.

[57] Brown, C.T., McDonell, V.G., and Talley, D.G. *Accounting for laser extinction, signal attenuation, and secondary emission while performing optical patternation in a single plane*. In *Fifteenth annual conference on liquid atomization and spray systems*. 2002.

[58] Pastor, J.V., Payri, R., Araneo, L., and Manin, J. *Correction method for droplet sizing by laser-induced fluorescence in a controlled test situation*. Opt. Eng., **48**:1–11, 2009.

[59] Smallwood, G.J., Gülder, O.L., and Snelling, D.R. *The structure of the dense core region in transient diesel sprays.* In *Twenty-Fifth Symposium (International) on Combustion / The combustion institute*, pp. 371–379. 1994.

[60] Powell, C.F., Yue, Y., Poolab, R., and Wanga, J. *Time-resolved measurements of supersonic fuel sprays using synchrotron x-rays.* Journal of Synchrotron Radiation, **7**:356–360, 2000.

[61] Sedarsky, D. *Ballistic Imaging of Transient Phenomena in Turbid Media.* Ph.D. thesis, Lund University, 2009.

[62] Linne, M., Paciaroni, M., Berrocal, E., and Sedarsky, D. *Ballistic imaging of liquid breakup processes in dense sprays.* In *Proceeding of the 32nd International Symposium on Combustion.* 2009.

[63] Sedarsky, D.L., Paciaroni, M.E., Linne, M.A., Gord, J.R., and Meyer, T.R. *Velocity imaging for the liquid-gas interface in the near field of an atomizing spray: proof of concept.* Opt. Lett., **31**:906–908, 2006.

[64] Sedarsky, D., Gord, J., Cartner, C., Meyer, T., and Linne, M. *Fast-framing ballistic imaging of velocity in an aerated spray.* Opt. Lett., **34**:2748–2750, 2009.

[65] Wu, Q., Merchant, F.A., and Castleman, K.R. *Microscope Image Processing.* Academic Press, 2008.

[66] Pawley, J.B. *Handbook of Biological Confocal Microscopy.* Plenum Press, New York, 1995.

[67] Neil, M.A.A., Juškaitis, R., and Wilson, T. *Method of obtaining optical sectioning by using structured light in a conventional microscope.* Opt. Lett., **22**:1905–1907, 1997.

[68] Elson, D.S., Siegel, J., Webb, S.E.D., Lévêque-Fort, S., Parsons-Karavassilis, D., Cole, M.J., French, P.M.W., Davis, D.M., Lever, M.J., Juškaitis, R., Neil, M.A.A., Sucharov, L.O., and Wilson, T. *Wide-field fluorescence lifetime imaging with optical sectioning and spectral resolution applied to biological samples.* J. Mod. Optic., **49**:985–995, 2002.

[69] Krzewina, L. and Kim, M. *Single exposure optical sectioning by color structured illumination microscopy.* Opt. Lett., **31**:477–479, 2006.

[70] Wicker, K. and Heintzmann, R. *Single-shot optical sectioning using polarization-coded structured illumination.* J. Opt., **12**:9 pp, 2010.

[71] Gustafsson, M.G.L. *Nonlinear structured-illumination microscopy: wide-field fluorescence imaging with theoretically unlimited resolution.* Proc. Natl. Acad. Sci. U.S.A., **102**:13081–13086, 2006.

[72] Gustafsson, M. *Surpassing the lateral resolution limit by a factor of two using structured illumination microscopy.* J. Microsc., **198**:82–87, 2000.

[73] Gustafsson, M.G.L., Agard, D.A., and Sedat, J.W. *Doubling the lateral resolution of wide-field fluorescence microscopy using structured illumination.* In *Three-Dimensional and Multidimensional Microscopy: Image Acquisition Processing VII.* 2000.

[74] Kner, P., Chhun, B.B., Griffis, E.R., Winoto, L., and Gustafsson, M.G.L. *Super-resolution video microscopy of live cells by structured illumination.* Nat. Methods, **6**:339–342, 2009.

[75] Caulier, Y., Spinnler, K., Bourennane, S., and Wittenberg, T. *New structured illumination technique for the inspection of high-reflective surfaces: Application for the detection of structural defects without any calibration procedures.* EURASIP Journal on Image and Video Processing, **Article ID 237459**:14 pages, 2008.

[76] Cortizo, E., Yeras, A.M., Lepore, J., and Garavaglia, M. *Application of the structured illumination method to study the topography of the sole of the foot during a walk.* Opt. Laser Eng., **40**:117–132, 2003.

[77] Eckbreth, A.C. and Davis, J.W. *Spatial resolution enhancement in coaxial light scattering geometries.* Appl. Opt., **16**:804–806, 1977.

[78] Kaldvee, B., Ehn, A., Bood, J., and Aldén, M. *Development of a picosecond lidar system for large-scale combustion diagnostics.* Appl. Opt., **48**:65–72, 2008.

[79] Siegel, J., Elson, D.S., Webb, S.E.D., Parsons-Karavassilis, D., Lévêque-Fort, S., Cole, M.J., Lever, M.J., French, P.M.W., Neil, M.A.A., Juškaitis, R., and Wilson, T. *Whole-field five-dimensional fluorescence microscopy combining lifetime and spectral resolution with optical sectioning.* Opt. Lett., **26**:1338–1340, 2001.

[80] Breuninger, T., Greger, K., and Stelzer, E.H.K. *Lateral modulation boosts image quality in single plane illumination fluorescence microscopy.* Opt. Lett., **32**:1938–1940, 2007.

[81] Cole, M.J., Siegel, J., Webb, S.E.D., Jones, R., Dowling, K., Dayel, M.J., Parsons-Karavassilis, D., French, P.M.W., Lever, M.J., Sucharov, L.O.D., Neil, M.A.A., Juškaitis, R., and Wilson, T. *Time-domain whole-field fluorescence lifetime imaging with optical sectioning.* J. Microsc., **203**:246–257, 2000.

[82] Wang, L., Liang, X., Galland, P., Ho, P., and Alfano, R. *True scattering coefficients of turbid matter measured by early-time gating.* Opt. Lett., **20**:913–915, 1995.

[83] Ansmann, A., Riebesell, M., and Weitkamp, C. *Measurement of atmospheric extinction profiles with a raman lidar.* Opt. Lett., **15**:746–748, 1990.

[84] Lim, J., Sivathanu, Y., Narayanan, V., and Chang, S. *Optical petternation of a water spray using statistical extinction tomography.* Atomization Spray, **13**:27–43, 2003.

[85] Koh, H., Kim, D., Shin, S., and Yoon, Y. *Spray characterization in high pressure environment using optical line patternator.* Meas. Sci. Technol., **17**:2159–2167, 2006.

[86] Inagaki, K., Miura, S., Nakakita, K., and Watanabe, S. *Quantitative soot concentration measurement with the correction of attenuated signal intensity using laser-induced incandescence.* In *The fourth international symposium CO-MODIA.* 1998.

[87] Grangeat, P. *Tomography.* ISTE Ltd and John Wiley & Sons, 2009.

[88] Cai, W., Powell, C.F., Yue, Y., Narayanan, S., Wanga, J., Tate, M.W., Renzi, M.J., Ercan, A., Fontes, E., and Grunere, S.M. *Quantitative analysis of highly transient fuel sprays by time-resolved x-radiography.* Appl. Phys. Lett., **83**:1671–1673, 2003.

[89] Wang, J. *X-ray vision of fuel sprays.* Journal of Synchrotron Radiation, **12**:197–207, 2005.

[90] Wang, Y., Lui, X., Im, K.S., Lee, W.K., Wang, J., Fezzaa, K., Hung, D.L.S., and Winkelman, J.R. *Ultrafast X-ray study of dense-liquid-jet flow dynamics using structure-tracking velocimetry.* Nature Phys., **4**:305–309, 2008.

[91] Lei, M. and Zumbusch, A. *Structured light sheet fluorescence microscopy based on four beam interference.* Opt. Express, **18**:19232–19241, 2010.

[92] Choi, W., Fang-Yen, C., Badizadegan, K., Oh, S., Lue, N., Dasari, R.R., and Feld, M.S. *Tomographic phase microscopy.* Nat. Methods, **4**:717–719, 2007.

[93] Neil, M.A.A., Juškaitis, R., and Wilson, T. *Real time 3D fluorescence microscopy by two beam interference illumination.* Opt. Commun., **153**:1–4, 1998.

[94] Pfadler, S., Beyrau, F., Löffler, M., and Leipertz, A. *Application of a beam homogenizer to planar laser diagnostics.* Opt. Express, **14**:10171–10180, 2006.

[95] Nikolajeff, F., Hård, S., and Curtis, B. *Diffractive microlenses replicated in fused silica for excimer laser-beam homogenizing.* Appl. Opt., **36**:8481–8489, 1997.

[96] Pfadler, S., Löffler, M., Beyrau, F., and Leipertz, A. *Improvement of planar laser diagnostics by the application of a beam homogenizer.* In *Third International Conference on Optical and Laser Diagnostics.* 2007.

[97] Kana, E.T., Bollanti, S., Lazzaro, P.D., Murra, D., Bouba, O., and Onana, M.B. *Laser beam homogenization: Modeling and comparison with experimental results.* Opt. Commun., **264**:187–192, 2006.

[98] Keller, P.J., Schmidt, A.D., Santella, A., Khairy, K., Bao, Z., Wittbrodt, J., and Stelzer, E.H.K. *Fast, high-contrast imaging of animal development with scanned light sheet-based structured-illumination microscopy.* Nat. Methods, **7**:637–642, 2010.

[99] Schaefer, L.H., Schuster, D., and Schaffer, J. *Structured illumination microscopy: artefact analysis and reduction utilizing a parameter optimization approach.* J. Microsc., **216**:165–174, 2004.

[100] Schäfer, M., Ketterle, W., and Wolfrum, J. *Saturated 2D-LIF of OH and 2D determination of effective collisional lifetimes in atmospheric pressure flames.* Appl. Phys. B, **52**:341–346, 1991.

[101] Daily, J.W. *Saturation of fluorescence in flames with a gaussian laser beam.* Appl. Opt., **17**:225–229, 1978.

[102] Seyfried, H. *Laser Spectroscopic techniques for combustion diagnostics directed towards industrial applications.* Ph.D. thesis, Lund University, 2007.

[103] Ehn, A., Johansson, O., Bood, J., Arvidsson, A., Li, B., and Aldén, M. *Fluorescence lifetime imaging in a flame.* In *Proceedings of the Combustion Institute.* 2011.

[104] Dibble, R.W. and Hollenbach, R.E. *Laser rayleigh thermometry in turbulent flames.* In *The Eighteenth Symposium (International) on Combustion.* 1981.

[105] Bergmann, V., Meier, W., Wolff, D., and Stricker, W. *Application of spontaneous Raman and Rayleigh scattering and 2D LIF for the characterization of a turbulent $CH_4/H_2/N_2$ jet diffusion flame.* Appl. Phys. B, **66**:489–502, 1998.

Summary of Papers

Paper I: The structured illumination technique was applied on an optically dilute two-phase flow (generated by a nebulizer) with the aim of investigating whether the method could be implemented for single-ended imaging.

I planned and conducted the experimental work. I also performed the data post-processing, produced the illustrations and was responsible for the preparation of the manuscript.

Paper II: An experimental approach for "single-shot" SLIPI measurements is described in this paper. A flow of water droplets (generated by a nebulizer) was probed and the improvements in image contrast, when applying SLIPI, was quantified. These were the first successful SLIPI measurements.

I performed the measurements together with Edouard Berrocal. I performed the data post-processing, produced the illustrations and was responsible for the preparation of the manuscript.

Paper III: SLIPI was applied for average imaging of a hollow-cone water spray. These were the first SLIPI measurements of a high-pressure liquid spray system. The sample was chosen because of its (supposedly) hollow internal structure, where the aim was to demonstrate the multiple light scattering filtering capabilities of SLIPI.

Edouard Berrocal planned the measurements, which were conducted by him and myself. I was responsible for the data post-processing of the SLIPI images and produced most of the illustrations. I also participated in the preparation of the manuscript.

Paper IV: This paper describes a "single-shot" SLIPI system which is capable of temporally freezing droplet motions up to approximately 600 m/s. To reduce the acquisition time (compared to Paper II) three individual laser systems were employed, one for each spatial phase of the modulation.

I planned and conducted the experimental work. I also carried out the required data post-processing, produced the illustrations and was responsible for the preparation of the manuscript.

Paper V: The measurements presented in this paper can be considered a pre-study to both Paper VIII and IX. Two measurements were performed, both conducted on an air-assisted solid cone water spray. First the possibility of performing 3D imaging using SLIPI was investigated by means of a "bread-slicing" approach. The results showed clear differences between SLIPI and conventional imaging, where the effect of signal attenuation and laser extinction was hardly noticeable using the latter technique, despite the relatively high optical depth. In the second test, quantitative imaging of the OD based on structured illumination was performed and the results compared with conventional wide-field-, laser sheet- and point transillumination. It was found that the values of OD obtained using structured illumination was comparable with those obtained using point transillumination.

The experimental work was carried out by myself, Edouard Berrocal and Rikard Wellander. I did the image post-processing, produced the illustrations and was responsible for the preparation of the manuscript.

Paper VI: This paper describes the dual-SLIPI approach, which allows the extinction coefficient to be visualized spatially resolved in 2D solely by means of side-scattering detection. The capabilities of the technique was first investigated on a homogeneous scattering sample and then demonstrated on two different spray systems.

I developed the dual-SLIPI technique, conducted the experiments and did the data post-processing. I also produced the illustrations and was responsible for the preparation of the manuscript.

Paper VII: Here the accuracy, precision and limitations of SLIPI was investigated for both Mie scattering and fluorescence. Monodisperse and homogeneous scattering and fluorescing samples with different particle concentrations and diameters were probed. 72 different measurement cases were investigated and the results conclusively illustrate the benefits with SLIPI, which showed a remarkable repeatability. However, the results also show how the accuracy of SLIPI is negatively affected by the particle diameter, where the measurements performed on larger particles led to less accurate results.

Edouard Berrocal and Lucio Araneo planned the measurements and were responsible for the preparation of the samples. I was responsible for the optical setup and I conducted most of the measurements. I carried out the post-processing, most of the data analysis and produced the illustrations. I was also responsible for the preparation of the manuscript.

Paper VIII: This paper describes an experimental approach to measure the extinction coefficient of a turbid sample spatially resolved in 3D. The technique is based on measuring both the path-integrated attenuation of light and the scattered light, both using SLIPI. By probing the sample in a "bread-slicing" manner the exponential reduction of the signal intensity can be compensated for. The method was successfully tested on both a homogeneous sample and an air-assisted solid cone water spray.

Rikard Wellander and Edouard Berrocal developed the technique. I participated in the experimental part and was responsible for the post-processing of the SLIPI

images (except for the calculations of μ_e). I made small contributions to the text.

Paper IX: Much like the previous paper, this work aimed at performing 3D imaging of the extinction coefficient. The approach used here was based on combining structure illumination and computed tomographic imaging. The linearity of the response of the system as a function of OD was first investigated on a homogeneous sample with convincing results. Thereafter the technique was implemented on two different types of spray systems.

I planned and conducted the measurements. I also wrote the reconstruction algorithm, produced the illustrations and was responsible for the preparation of the manuscript.

Paper X: This work investigates the possibility of performing multiple scattering rejection based on a single intensity modulated laser sheet measurement, an approach referred to as "single phase SI". A computer program was developed with the purpose of extracting the local amplitude of the incident modulation.

Edouard Berrocal was responsible for the experiments and the Monte-Carlo simulations, whereas Jonathan Johnsson wrote the computer program. I made small contributions to the text.

Paper XI: This paper presents SLIPI measurements performed on a diesel spray for both Mie scattering and fluorescence detection. The evolution of the spray was investigated qualitatively. In addition, the dual-SLIPI technique was employed at late times after SOI to demonstrate the possibility of overcoming issues related to laser extinction and signal attenuation. Also presented in this paper are images of the ratio between fluorescence and Mie scattering acquired using SLIPI.

I was responsible for the optical arrangement and the data post-processing. Peter Hottenbach was responsible for the diesel spray operation and Edouard Berrocal was responsible for analyzing the results as well as for the preparation of the manuscript.